

LINKING CLIMATE HISTORY AND ICE CRYSTALLINE FABRIC EVOLUTION IN
POLAR ICE SHEETS

By

Joseph Huston Kennedy

RECOMMENDED:


Dr. Curt Szuberla


Dr. David Newman


Dr. Ed Bueler


Dr. Martin Truffer


Dr. Erin Pettit
Advisory Committee Chair


Dr. Renate Wackerbauer
Chair, Department of Physics

APPROVED:


Dr. Paul Layer
Dean, College of Natural Science and Mathematics


Dr. John Eichelberger
Dean of the Graduate School


Date

LINKING CLIMATE HISTORY AND ICE CRYSTALLINE FABRIC EVOLUTION IN
POLAR ICE SHEETS

A
DISSERTATION

Presented to the Faculty
of the University of Alaska Fairbanks
in Partial Fulfillment of the Requirements
for the Degree of
DOCTOR OF PHILOSOPHY

By

Joseph Huston Kennedy, B.S.

Fairbanks, Alaska

August 2015

Abstract

An ice sheet consists of an unfathomable number of ice crystallites (grains) that typically have a preferred orientation of the crystalline lattices, termed fabric. At the surface of ice sheets, the microstructural processes that control the grain structure and fabric evolution are influenced by climate variables. Layers of firn, in different climate regimes, may have an observable variation in fabric which can persist deep into the ice sheet; fabric may have ‘memory’ of these past climate regimes.

To model the evolution of a subtle variation in fabric below the firn-ice transition, we have developed and released an open-source Fabric Evolution with Recrystallization (FEVOR) model. FEVOR is an anisotropic stress model that distributes stresses through explicit nearest-neighbor interaction. The model includes parameterizations of grain growth, rotation recrystallization and migration recrystallization which account for the major recrystallization processes that affect the macroscopic grain structure and fabric evolution. Using this model, we explore the evolution of a subtle variation in near-surface fabric using both constant applied stress and a stress-temperature history based on data from Taylor Dome, East Antarctica.

Our results show that a subtle fabric variation will be preserved for ≈ 200 ka in compressive stress regimes with temperatures typical of polar ice-sheets. The addition of shear to compressive stress regimes preserves fabric variations longer than in compression-only regimes because shear drives a positive feedback between crystal rotation and deformation. We find that temperature affects how long the fabric variation is preserved, but does not affect the strain-integrated fabric evolution profile except when crossing the thermal-activation-energy threshold ($\approx -10^\circ\text{C}$). Even at high temperatures, migration recrystallization does not rid the fabric of its memory under most conditions. High levels of nearest-neighbor interactions between grains will rid the fabric of its memory more quickly than low levels of nearest-neighbor interactions.

Because FEVOR does not compute flow, an integrated fabric-flow model is needed to investigate the flow-fabric feedbacks that arise in ice sheets. Using the open-source Parallel Ice Sheet Model (PISM) and FEVOR, we develop a combined flow-fabric model (PISM-FEVOR). We provide the first integrated flow-fabric model that explicitly computes the fabric evolution and includes all three major recrystallization processes. We show that PISM-FEVOR is able to capture the flow enhancement due to fabric by modeling a slab-on-slope glacier, initialized with a variety of fabric profiles. We also show that the entire integrated fabric-flow history affects the final simulated flow. This provides a further, independent validation of using an integrated fabric-flow model over a constant enhancement factor in ice-sheet models.

Table of contents

	Page
Signature page	i
Title page	iii
Abstract	v
Table of contents	vii
List of figures	xi
List of tables	xiii
Acknowledgements	xv
Chapter 1 Introduction	1
1.1 Background	1
1.2 Objectives	4
1.3 References	7
Chapter 2 The evolution of ice crystal fabric in ice sheets and its link to climate history	11
2.1 Abstract	11
2.2 Introduction	11
2.3 Background	14
2.4 The model	17
2.4.1 Crystal physics	20
2.4.2 Rotating crystals	21
2.4.3 Bulk properties	22
2.4.4 Crystal processes	23
2.5 Generating initial crystal distributions	24
2.5.1 Orientation tensor	27
2.6 Constant stress experiments	28
2.6.1 Results	31
2.7 Taylor dome experiments	33
2.7.1 Experimental setup	35
2.7.2 Results	38
2.8 Discussion	41
2.9 Conclusions	45
2.10 Acknowledgements	47
2.11 References	47

Chapter 3 The response of fabric variations to simple shear and migration recrystalliza-

tion	55
3.1 Abstract	55
3.2 Introduction	55
3.3 Fabric	58
3.4 The model	59
3.4.1 Model physics	61
3.4.2 Recrystallization processes	65
3.5 Experimental setup	69
3.6 Results and discussion	72
3.6.1 Simple shear	74
3.6.2 Nearest neighbor interaction	78
3.6.3 Temperature	78
3.6.4 Further discussion	80
3.7 Conclusions	83
3.8 Acknowledgements	84
3.9 References	84

Chapter 4 PISM-FEvoR: a multi-scale ice flow model incorporating fabric evolution

with recrystallization	89
4.1 Abstract	89
4.2 Introduction	89
4.3 FEvoR	93
4.4 PISM	96
4.5 The integrated PISM-FEvoR model	97
4.6 Slab-on-slope example	101
4.6.1 Evolution	103
4.7 Slab-on-slope experiments	103
4.7.1 Evolution	104
4.8 Further discussion	104
4.8.1 Further development	106
4.9 Conclusions	107
4.10 Acknowledgements	107

4.11	References	107
Chapter 5	Conclusions	115
5.1	Looking forward	116
5.2	Final words	117
5.3	References	118

List of figures

	Page
1.1 The crystalline structure of ice.	2
1.2 Measuring ice crystalline fabrics.	3
1.3 Comparison of $\delta^{18}\text{O}$ and fabric in the GISP2 ice core.	4
2.1 The polycrystal structure.	18
2.2 Flow chart of the model.	19
2.3 Contoured Schmidt plot of the initial fabrics for both the constant stress and Taylor Dome experiments.	30
2.4 The uniaxial-compression runs, 1-6 (Table 2.2).	31
2.5 Separation of the largest eigenvalue, e_1 , between the top layer and middle layer for the uniaxial-compression runs, 1–6.	33
2.6 The pure-shear runs, 7-12 (Table 2.2).	35
2.7 Separation of the largest eigenvalue, e_1 , between the top layer and middle layer for the pure-shear runs, 7-12.	37
2.8 Depth–age profile for Taylor Dome, East Antarctica.	38
2.9 Fabric profile with depth for Taylor Dome.	39
2.10 Depth–stress profile for Taylor Dome.	40
2.11 Evolution of fabric within an ice sheet based on Taylor Dome for the dome-like Taylor Runs, 13-15 (Table 2.3).	40
2.12 Same as Figure 2.11, but within a glacier based on Taylor Dome for the ridge-like Taylor runs, 16-18 (Table 2.3).	41
2.13 Contoured Schmidt plots of the evolved middle layer fabric after 210 000 years for dome-like (top row) and ridge-like (bottom row) symmetry.	42
2.14 Cumulative strain in the Taylor Dome runs.	43
2.15 Largest eigenvalue separation for Taylor Dome.	44
3.1 The polycrystal structure.	60
3.2 Flow chart of the model.	61
3.3 Contoured Schmidt plots of the magnitude of the resolved shear stress, \mathcal{T}	62
3.4 Contoured Schmidt plot of the initial fabrics for both the constant-stress and Taylor Dome experiments.	69

	Page
3.5 Contoured ternary plot of the eigenvalues of the fabrics for every time-step of all 288 model runs.	73
3.6 The effects of simple shear on the evolution of the layered fabric (Figure 3.4).	74
3.7 The effects of simple shear on the evolution of the layered fabric (Figure 3.4) eigenvalue separation between the top/bottom and middle fabric layer.	76
3.8 The effects of nearest-neighbor interaction (NNI) on the evolution of the layered fabric (Figure 3.4).	77
3.9 The effects of temperature on the evolution of the layered fabric (Figure 3.4).	79
3.10 The total simulation time to evolve the fabric to 0.35 bulk strain for our different model runs.	80
3.11 Sensitivity to the model parameters (Table 3.1).	81
4.1 Contoured Schmidt plots of the magnitude of the Resolved Shear Stress \mathcal{T} from Eqn (4.9) for grains in the stress states of: uniaxial compression, pure shear, and simple shear.	96
4.2 Flow chart of the combined PISM-FEVR model.	98
4.3 Geometric visualization of bilinear interpolation from a regular grid (black) to a particle (pink).	99
4.4 A cross-section of the computational domain of PISM-FEVR.	99
4.5 Visualization of natural neighbor interpolation of a grid point (black) from a scattered collection of particles (pink).	100
4.6 Initial PISM-FEVR setup for the 2D slab-on-slope experiments with slope θ and periodic boundary conditions in x	102
4.7 Initial eigenvalues and calculated enhancement factors for a slab-on-slope with a linearly increasing fabric profile.	111
4.8 The evolution of FEVR particles for a slab with a linearly increasing initial fabric.	112
4.9 Simulation times for the slab-on-slope experiment with differing number of FEVR distribution grains.	112
4.10 The evolution of FEVR particles in a slab with a variety of initial fabric profiles.	113
5.1 Comparison of $\delta^{18}\text{O}$ and fabric in the GISP2 ice core (reprint of Figure 1.3).	118

List of tables

	Page
2.1 Values of the parameters used in the model.	23
2.2 Summary of the run setup of our constant-stress experiments.	29
2.3 Summary of the run setup of our Taylor Dome experiments.	41
3.1 Values of the parameters used in the model.	64
3.2 Stress regimes, stress magnitude, nearest-neighbor interaction parameters, and temperature values used in the constant-stress experiments.	72
4.1 Notation.	91
4.2 Results summary for the different initial fabric profiles.	105

Acknowledgements

I regarded coming to Alaska for graduate school as a grand adventure of exploration and discovery in both the tangible and intellectual world. When I climbed into my '95 Ford Exploder [sic] with my brother Jon, to embark on our journey to Alaska, I had no idea just how much of an adventure I was getting myself into. Nor how the amazing people here, and this place itself would profoundly affect me down to my very soul.

I must first thank my advisor, Erin Pettit, for truly fulfilling that promise of adventure. She sent me on many scientific adventures around the world and I was able to see Austria, France, Greenland, and Antarctica (though that last one very nearly killed me). She encouraged me to become a NSF GK-12 fellow, where I got to spend a year playing science with sixty first-graders – a truly wonderful experience. During the course of our research together, she gave me the freedom to explore my own ideas and develop into the researcher I wanted to become. As quite the adventurer herself, she never even batted an eye when I wanted to take a summer off to paddle 1400 miles of the Yukon River. I am very thankful for all her encouragement, support, and putting up with me for these short seven years.

My committee members were all equally supportive and encouraging throughout this dissertation. Martin Truffer taught me much of what I know about glaciology through his course work and the many discussions he was always happy to have. Ed Bueler was always enthusiastic and willing to help clarify my sometimes poor understanding of computation and mathematics. Curt Szuberla and David Newman both provided a great outside perspective; they reminded me to see the broader context of my work and the importance of telling a good story.

I don't believe there is a better place to study glaciology than the glaciers group in the Geophysical Institute (GI). The faculty have done an exemplary job of creating an open and encouraging environment where everyone from undergraduates to emeritus faculty are seen as equal colleagues. The lunchtime discussions, coffee-machine banter, and cake-filled gatherings all made for a rather enjoyable work environment. So thank you all very much, and especially Anthony Ardent for providing an amazing espresso machine and Regine Hock for providing all the cake.

I owe much of my success, education, and well being to the many graduate students, staff, and postdocs I have had the pleasure of working with, getting to know, and call friends. I could write a novel describing the good times and adventures I've had with Bob McNabb, Peter Peterson, Ronni Grapenthin, Christina Carr, Laura Oxtoby, Andy Aschwanden, David and Agitha Podraski, Carl Anderson, Daisy Huang, Jamie Martin, Florian Ziemann, Vanessa Stevens, Dani DellaGiustina, Scott Otterbacher, Philip and Alyssa Loring, Marijke Habermann, Kelly McFarlin, Joanna Young,

Anna and Brian Perttu, Annie Worden, Aurora Roth, Barbara Trussel, Jason Amundson, Sam Herreid, Constantine Khroulev, Tim and Sophie Bartholomaeus, Alessio Gusmeroli, Ryan Kovatch, Chris Bruton, Natalie Hinkel, Allie Rutledge, Christian Kienholz, and many others. A giant thank you to all of you, I would not have been able to do it without you. Bob, Peter, Ronni and Laura, a special thanks to you; at least one of you has been on every adventure I've taken in Alaska. You've truly made this a magical place. Bob, thanks for telling me "No!" when my ideas have been just a little too crazy; I may not have lived through this otherwise! Christina, thank you especially for always being willing to help with anything – I most definitely couldn't have done this without you.

I'd also like to thank James Stewart, Kristen Larsen, and Brad Johnson, without whom I would have never gotten myself into this wonderful mess called graduate school. James challenged me in his introductory physics classes at Western Washington University and sparked my passion for physics and teaching. Kristen was a champion of an undergraduate advisor and was always willing to go the extra mile for any of her students. Brad introduced me to computational physics, which I immediately knew I wanted to do for the rest of my life. All three of them provided the encouragement, advice, and support that carried me through my undergraduate program and into my graduate program.

My family has always been the foundation to my success in anything. To my parents, Steve and Leslie Kennedy: if I'm ever able to be even half as good of a parent as you have been, I will have done well with my life. Love and thanks to my brother who brought me to Alaska and started me off on this adventure; a drive we'll need to do again. I must also thank my aunts and uncles Dan, Ray and Darlene, and Gay and Darla. They have always been constant sources of encouragement, support, and in Gay's case, bad habits. I owe much of my love of music, theater, nature and the world to them. Thank you all very much.

And finally, Holly Dean. Holly has proved to be the single greatest source of encouragement, support, and understanding in my short time up here. She has always borne the brunt of my frustration, shared in my excitement, and dealt with the long hours I always seem to find myself working with grace. I'm so glad I met her here, and that we've had so many fun adventures together – we attempted to paddle 1400 miles of the Yukon River (and made it 700 miles even though it was a flood year!), hunted caribou on the north slope, accidentally ran rapids, and had many bears encounters (she really does attract them). I'm so thankful that she has agreed to be my life long adventure partner; I'm looking forward to many more Jolly Adventures to come.

Chapter 1

Introduction

1.1 Background

Ice sheets are generally defined as a contiguous mass of ice that covers a continental sized area ($> 50000 \text{ km}^2$; Cogley and others, 2011). Currently, the Greenland Ice Sheet in the north polar region, and the Antarctic Ice sheet in the south polar region, are the only two ice sheets on Earth. The latter, while contiguous, is often subdivided along the Transantarctic Mountains into the East Antarctic Ice Sheet and the West Antarctic Ice Sheet. The West Antarctic Ice Sheet is the last remaining marine ice sheet where the majority of its bedrock is below sea level (Fretwell and others, 2013). This cause it to behave differently than its eastern counterpart, which is best highlighted by its possible instability (Mercer, 1978).

Ice sheets are often described as “time machines” because they act as storehouses for paleoclimate information (e.g., Jouzel and Masson-Delmotte, 2010; Alley, 2014). This information, usually obtained from thousands-of-meters long ice cores, can be used for paleoclimate reconstruction (Alley, 2010), where a “memory” of past climate is extracted from the ice. The oxygen isotope ratio, $\delta^{18}\text{O}$ measured in ice cores has been one of the most successful climate proxies used to reconstruct past climate since the pioneering work of Paterson and Clarke (1978). Paterson was able to reconstruct a mean annual air temperature history to 11000 BP from the $\delta^{18}\text{O}$ record contained in ice cores from the Devon Island Ice Cap. He used the air temperature history to predict the ice temperature distribution within the ice cap and was able to successfully predict the small differences in temperature observed in upper parts of two boreholes situated 300 m apart. However, due to the complex nature of the water cycle, and its effect on $\delta^{18}\text{O}$, it is important to corroborate $\delta^{18}\text{O}$ paleoclimate reconstructions against other known climate proxies (Alley and Cuffey, 2001).

In order to use proxy measurements from an ice-core for paleoclimate reconstruction, the age of the ice at the particular depth of the proxy measurement must be determined. Because an ice-sheet is flowing, and flow disturbances can reorder the annual layers of ice, an understanding of the flow history is required to determine the age of the ice. To accurately model ice flow, processes spanning many scales must be accounted for (Faria and others, 2009). The crystalline structure of ice (atomic scale) is hexagonally symmetric (Figure 1.1) and the individual response of a crystallite (cm scale) to stress is highly anisotropic. In polycrystalline ice (natural ice; m scale), the spatial distribution of these crystallite or grains is what determines the polycrystalline ice’s bulk material properties and overall response to stress. Only when the crystallite or grain orientations are uniformly distributed in space can the anisotropic behavior of each individual grain be ignored

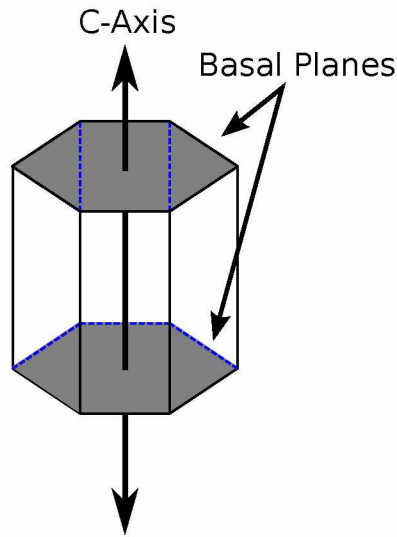
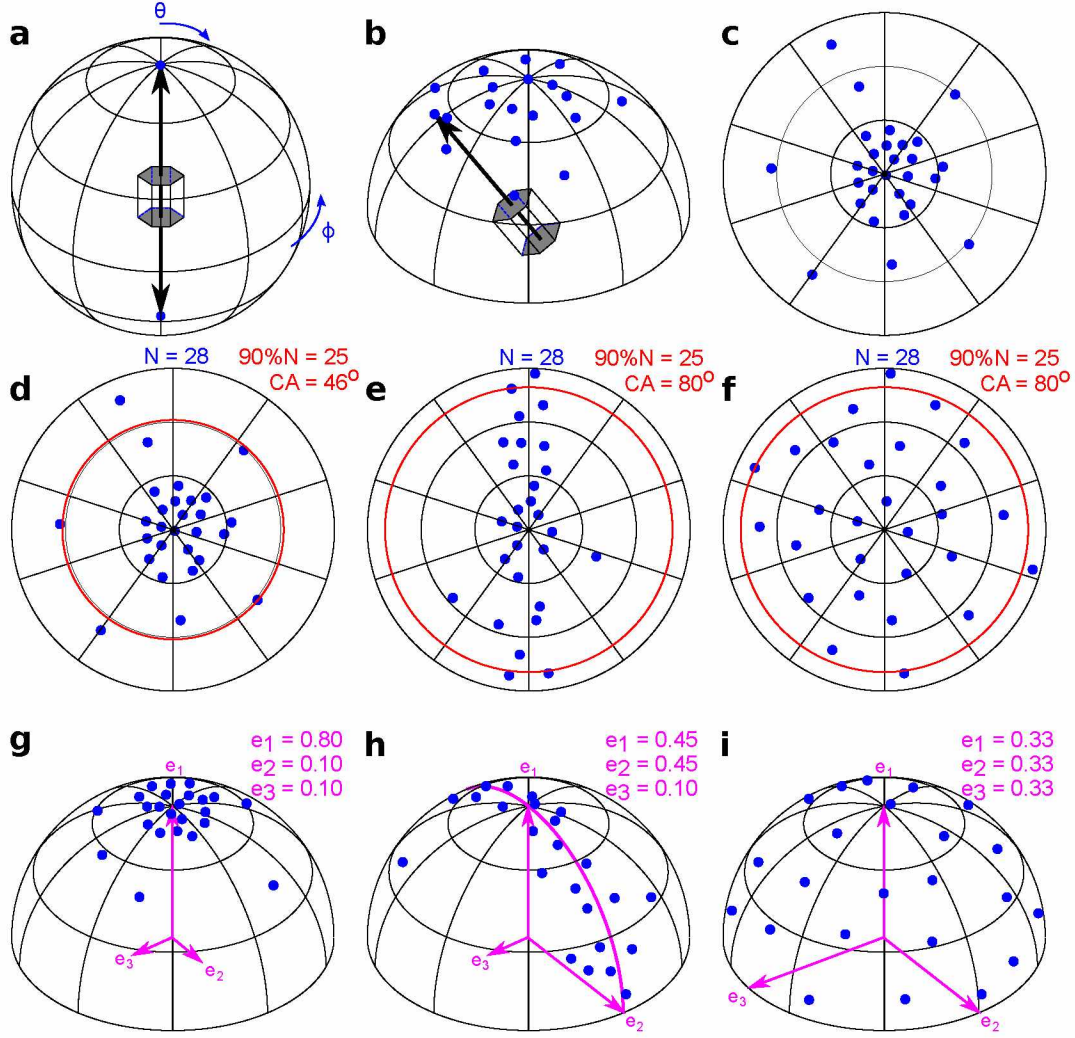


Figure 1.1: The crystalline structure of ice. The hexagonal planes are termed the basal planes, and the optical axis or c-axis is perpendicular to the basal planes.

– giving rise to isotropic behavior in response to stress. Ice with a grain preferred orientation (fabric) will behave anisotropically in response to stress (Figure 1.2 illustrates how fabric is measured). The emergent flow of an ice sheet (continental scale) is then the integrated polycrystalline response to stresses that arise from the overall ice sheet geometry.

Glen (1955) assumed isotropic behavior in his flow law that has gained wide acceptance in glaciology, as it successfully explained early field observations. Modern field measurements have shown some discrepancies with flow predicted by Glen’s flow law, many of which can be attributed to the fabric in the ice sheet (e.g., Thorsteinsson and others, 1999), or impurities (e.g., Faria and others, 2009). Detailed microstructural observations, such as ice-core line-scanners (Svensson and others, 2005; Faria and others, 2010), optical and electron microscopy, and x-ray diffraction and tomography (Faria and others, 2010), provide insights into the integrity of ice-core stratigraphy.

From the detailed microstructure studies that have been carried out in ice cores for both Antarctic and Greenlandic ice, it has been observed that aspects of climate history are recorded in the microstructure of ice itself (e.g., Gow and others, 1997; Paterson, 1991; Durand and others, 2007; Pettit and others, 2011). Paterson (1991) showed that ice-age ice typically consists of smaller grains and stronger fabric (statistically preferred orientation of the ice crystal lattice) than Holocene ice, providing the first hint of a direct connection between paleoclimate and microstructure in an ice sheet. More recently, both thin-section data and sonic-velocity data from Dome C, East Antarctica



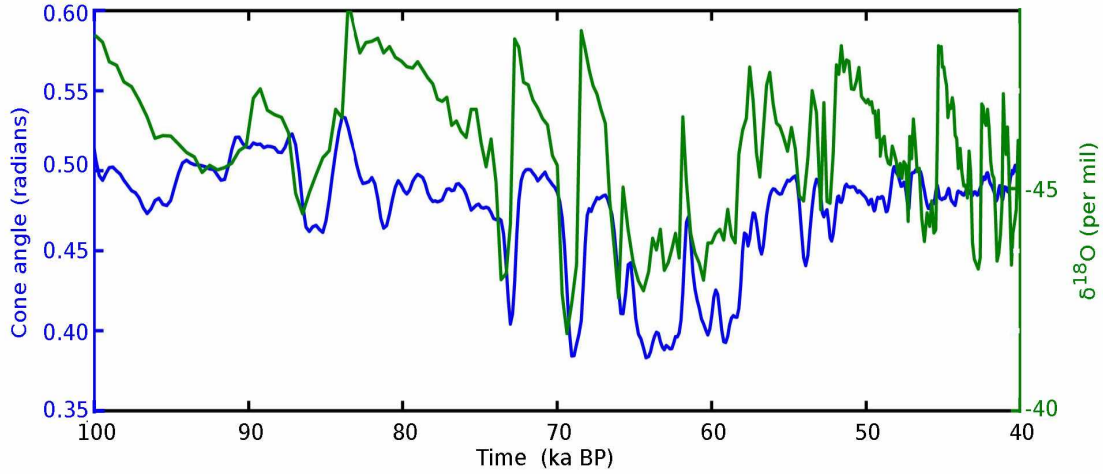


Figure 1.3: Comparison of $\delta^{18}\text{O}$ and fabric in the GISP2 ice core. Changes in the fabric (blue curve; Gow and others, 1997) appear to correlate with the known climate proxy $\delta^{18}\text{O}$ (green curve; Grootes and others, 1993).

show an abrupt transition in the ice rheology at 1750m depth which corresponds to a transition between the warm MIS-5 (marine isotope stage 5) and the cool MIS-6 about 150ka ago (Durand and others, 2007; Gusmeroli and others, 2012). Observations show that many microstructural features (impurities, grain size, fabric) generally correlate with climate history (e.g., Durand and others, 2006). In Figure 1.3, there is an apparent, albeit qualitative, correlation between $\delta^{18}\text{O}$ and the fabric measured in the Greenland Ice Sheet Project Two (GISP2) ice core (Grootes and others, 1993; Gow and others, 1997). Fabric itself however, has not yet been used as a climate proxy.

1.2 Objectives

The ultimate goal of this research is to develop ice crystalline fabric as a climate proxy. We hypothesize that because the microstructural processes active in the firn are sensitive to climatic variables (Alley and others, 1990), layers of firn experiencing different climate regimes may have observable variations in the fabric which can be preserved. For example, vapor deposition is the primary method of grain growth in the upper firn and it is anisotropic: deposition will favor either the basal or prism faces of the ice-crystalline lattice, depending on the temperature (Nelson and Knight, 1998). Grains with their preferred face parallel to the vapor pressure gradient will grow more than grains in a less favorable orientation. Because these grains grow at the expense of other grains (Colbeck, 1983), the well-oriented grains are more likely to remain (Carns and others, 2010, are developing a model to explore this process). Therefore, variations in texture and fabric in the

firm may reflect variations in temperature and vapor-pressure gradients (hypothesized by Adams and Miller, 2003). Consequently, fabric variations may preserve memory of past climate for as long as they are observable. This is analogous to the climate proxy $\delta^{18}\text{O}$; it is the variation in $\delta^{18}\text{O}$, not the particular amount of the oxygen isotope present, that allows us to extract a temperature history.

There are a number of large benefits to developing fabric as a climate proxy. First, a fabric proxy would provide another independent proxy to validation of current climate proxies, increasing the robustness of current paleoclimate reconstructions. Second, it may provide a way to increase the spatial resolution of climate reconstructions from the ice sheets. Due in large part to the unique challenges of working in such remote and extreme environments, drilling an ice core is often a near decade-long process (Alley, 2010). As such, there have only been a few dozen ice cores drilled in the polar ice sheets to date, resulting in a rather sparse spatial coverage over the ice sheets. Because fabric measurements can be taken from the bore hole using a sonic logger (Gusmeroli and others, 2012), a fast-access mechanical drill, which doesn't provide an intact core, can be used without losing the ability to reconstruct paleoclimate (Clow and Koci, 2002). Instead of a decade long project, a reconstruction could be created within a single year (albeit at a lower temporal resolution due to sonic loggers averaging data over multiple annual layers). Finally, ice cores have typically been taken at location that have minimal ice dynamics in order to provide the least error-prone depth-age analysis needed for paleoclimate reconstruction. Unfortunately, these locations do not correspond to the most interesting locations for ice microstructure and dynamics studies, leading to a call in the community for a physically-motivated ice-coring project (Faria and others, 2009); which has yet to come to fruition. The ability to provide paleoclimate reconstructions at high spatial scale would allow a physically-motivated coring project (which is likely to take a decade) to happen without losing the ability to generate new paleoclimate reconstructions throughout Antarctica and Greenland.

In order for climate history to be inverted from fabric data, a forward model of the ice fabric evolution is needed. The forward model must include the climate-dependent firm processes, and the subsequent metamorphism of the firm as it turns to ice, as well as the further evolution of ice within the ice sheet. Because this is a many-scale problem, encompassing processes from the mesoscopic to the macroscopic and beyond, a complete forward model will necessarily entail a number of interacting models. These models will need to compute: the climate, the firm microstructure evolution, the firm densification, the ice microstructure evolution, and the ice flow. These models can be split into two regimes, the firm regime and the ice regime.

In this study, we lay the foundation for crystalline fabric as a climate proxy in the ice regime by:

1. showing that a variation in fabric just below the firn ice transition may be preserved;
2. determining how long, and under what conditions, the variation is preserved in ice-sheet like conditions;
3. developing a flow-fabric integrated model which can be used to investigate in situ fabric evolution and cover the ice regime part of the complete forward model.

We develop a fabric-evolution model based largely on the work by Thorsteinsson (2001, 2002) and include phenomenological descriptions of the dominant recrystallization processes active within an ice sheet. Because ice cores are typically drilled at ice divides, and most of our in situ microstructural knowledge is derived from these cores, we apply this model to a fabric variation experiencing the ice-sheet divide-like conditions. We find that a variation can be preserved in an ice divide for ≈ 200 ka and throughout the depth of an ice-sheet using a simple model of Taylor Dome, East Antarctica, where migration recrystallization is not active. We present these results in Chapter 2, which has been published in the Journal of Glaciology as Kennedy and others (2013). As lead author, I developed the computational model, designed and conducted the experiments, and drafted the manuscript. Carlos L. Di Prinzio performed the fabric analysis for Taylor Dome, East Antarctica, and provided a description of the analysis technique. Erin C. Pettit provided guidance and edited the manuscript.

In Chapter 3, we extend our model to the wide variety of stress and temperature conditions found throughout the polar ice-sheets, including conditions that result in highly active migration recrystallization of the ice grains. We find that a fabric variation can be preserved even in the presence of migration recrystallization, and in the variety of conditions tested. We present these results in Chapter 3, which has been published in the Journal of Glaciology as Kennedy and Pettit (2015). As lead author, I developed the computational model, designed and conducted the experiments, and drafted the manuscript. Erin C. Pettit provided guidance and edited the manuscript.

Since our model developed in Chapter 2 and Chapter 3 is a fabric-evolution model, it does not compute the ice flow or a stress balance within an ice sheet; these must be prescribed externally. The new model in Chapter 4, dubbed the Fabric Evolution with Recrystallization (FEvOR) model, has been licensed and released as an open-source model (FEvOR, <https://github.com/FEvOR>) and has been integrated into the open-source Parallel Ice Sheet Model (PISM, <http://www.pism->

docs.org/). This is the first attempt in the glaciological community to fully integrate a fabric-evolution model into an ice flow model. In Chapter 4, we describe the PISM-FEVOR integrated model and present the results of a 2-dimensional slab-on-slope glacier model. A version of Chapter 4 is being prepared for submission to the Journal of Glaciology. As lead author, I developed FEVOR, guided the development of PISM-FEVOR, designed and conducted the experiments, and drafted the manuscript. Constantine Khroulev provided the majority of the PISM structure needed to integrate FEVOR and conduct the experiments, and reviewed the PISM-FEVOR code base. Erin C. Pettit provided guidance and edited the manuscript. Ed Bueler provided additional guidance and helpful discussions.

Finally, Chapter 5 describes the key findings presented here and discusses the path forward for developing ice crystalline fabric as a climate proxy.

1.3 References

- Adams, E.E. and D.A. Miller, 2003. Ice crystals grown from vapor onto an orientated substrate: application to snow depth-hoar development and gas inclusions in lake ice, *J. Glaciol.*, **49**(164), 8–12.
- Alley, R.B., 2010. Reliability of ice-core science: Historical insights, *J. Glaciol.*, **56**(200), 1095–1103.
- Alley, R.B., 2014. The Two-Mile Time Machine: Ice Cores, Abrupt Climate Change, and Our Future: Ice Cores, Abrupt Climate Change, and Our Future, Princeton Science Library, Princeton University Press.
- Alley, R.B. and K.M. Cuffey, 2001. Oxygen-and hydrogen-isotopic ratios of water in precipitation: Beyond paleothermometry, *Reviews in Mineralogy and Geochemistry*, **43**(1), 527–553.
- Alley, R.B., E.S. Saltzman, K.M. Cuffey and J.J. Fitzpatrick, 1990. Summertime formation of depth hoar in central Greenland, *Geophysical research letters*, **17**(13), 2393–2396.
- Carns, R., E.D. Waddington, E.C. Pettit and S.G. Warren, 2010. A model of grain growth and crystal fabric in polar snow and firn, *AGU Fall Meeting Abstracts*, D572.
- Clow, G.D. and B. Koci, 2002. A fast mechanical-access drill for polar glaciology, paleoclimatology, geology, tectonics, and biology, *Mem. Natl. Inst. Polar Res*, 1–30.

- Cogley, J.G., R. Hock, L.A. Rasmussen, A.A. Ardent, A. Bauder, R.J. Braithwaite, P. Jansson, G. Kaser, m. Moller, L. Nicholson and M. Zemp, 2011. Glossary of glacier mass balance and related terms, IHP-VII Technical Documents in Hydrology, UNESCO-IHP, Paris, 86 ed.
- Colbeck, S.C., 1983. Theory of metamorphism of dry snow, *J. Geophys. Res.*, **88**(C9), 5475–5482.
- Durand, G., F. Gillet-Chaulet, A. Svensson, O. Gagliardini, S. Kipfstuhl, J. Meyssonier, F. Parrenin, P. Duval and D. Dahl-Jensen, 2007. Change in ice rheology during climate variations – implications for ice flow modelling and dating of the EPICA Dome C core, *Climate of the Past*, **3**(1), 155–167.
- Durand, G., J. Weiss, V. Lipenkov, J.M. Barnola, G. Krinner, F. Parrenin, B. Delmonte, C. Ritz, P. Duval, R. Röthlisberger and M. Bigler, 2006. Effect of impurities on grain growth in cold ice sheets, *J. Geophys. Res.*, **111**(F01015).
- Faria, S.H., J. Freitag and S. Kipfstuhl, 2010. Polar ice structure and the integrity of ice-core paleoclimate records, *Quaternary Science Reviews*, **29**(1-2), 338–351.
- Faria, S.H., S. Kipfstuhl, N. Azuma, J. Freitag, I. Weikusat, M.M. Murshed and W.F. Kuhs, 2009. The multiscale structure of antarctica part I: Inland ice, *Low Temperature Science*, **68**(Sup.), 39–59.
- FEvoR, <https://github.com/FEvoR>. Fabric Evolution with Recrystallization, master branch.
- Fretwell, P., H.D. Pritchard, D.G. Vaughan, J.L. Bamber, N.E. Barrand, R. Bell, C. Bianchi, R.G. Bingham, D.D. Blankenship, G. Casassa, G. Catania, D. Callens, H. Conway, A.J. Cook, H.F.J. Corr, D. Damaske, V. Damm, F. Ferraccioli, R. Forsberg, S. Fujita, Y. Gim, P. Gogineni, J.A. Griggs, R.C.A. Hindmarsh, P. Holmlund, J.W. Holt, R.W. Jacobel, A. Jenkins, W. Jokat, T. Jordan, E.C. King, J. Kohler, W. Krabill, M. Riger-Kusk, K.A. Langley, G. Leitchenkov, C. Leuschen, B.P. Luyendyk, K. Matsuoka, J. Mouginot, F.O. Nitsche, Y. Nogi, O.A. Nost, S.V. Popov, E. Rignot, D.M. Rippin, A. Rivera, J. Roberts, N. Ross, M.J. Siegert, A.M. Smith, D. Steinhage, M. Studinger, B. Sun, B.K. Tinto, B.C. Welch, D. Wilson, D.A. Young, C. Xiangbin and A. Zirizzotti, 2013. Bedmap2: Improved ice bed, surface and thickness datasets for Antarctica, *Cryosphere*, **7**(1), 375–393.
- Glen, J.W., 1955. The creep of polycrystalline ice, *Proceedings of the Royal Society of London. Series A, Mathematical and Physical Sciences*, **228**(1175), 519–538.

- Gow, A.J., D.A. Meese, R.B. Alley, J.J. Fitzpatrick, S. Anandakrishnan, G.A. Woods and B.C. Elder, 1997. Physical and structural properties of the Greenland Ice Sheet Project 2 ice core : A review, *J. Geophys. Res.*, **102**(C12), 26,559–26,575.
- Grootes, P.M., M. Stuiver, J.W.C. White, S. Johnsen and J. Jouzel, 1993. Comparison of oxygen isotope records from the GISP2 and GRIP Greenland ice cores, *Nature*, **366**(6455), 552–554.
- Gusmeroli, A., E.C. Pettit, J.H. Kennedy and C. Ritz, 2012. The crystalline fabric of glacial ice from full-waveform borehole sonic logging, *J. Geophys. Res.*, **117**(F03021), 1–13.
- Jouzel, J. and V. Masson-Delmotte, 2010. Deep ice cores: the need for going back in time, *Quaternary Science Reviews*, **29**(27-28), 3683–3689.
- Kennedy, J.H. and E.C. Pettit, 2015. The response of fabric variations to simple shear and migration recrystallization, *J. Glaciol.*, **61**(227), 537–550.
- Kennedy, J.H., E.C. Pettit and C.L. Di Prinzio, 2013. The evolution of crystal fabric in ice sheets and its link to climate history, *J. Glaciol.*, **59**(214), 357–373.
- Mercer, J.H., 1978. West Antarctic ice sheet and CO₂ greenhouse effect: a threat of disaster, *Nature*, **271**(26), 321–325.
- Nelson, J. and C. Knight, 1998. Snow crystal habit changes explained by layer nucleation, *J. Atmos. Sci.*, **55**(8), 1452–1465.
- Paterson, W.S.B., 1991. Why ice-age ice is sometimes “soft”, *Cold Regions Science and Technology*, **20**, 75–98.
- Paterson, W.S.B. and G.K.C. Clarke, 1978. Comparison of theoretical and observed temperature profiles in Devon Island ice cap, Canada, *Geophysical Journal International*, **55**(3), 615–632.
- Pettit, E.C., T. Thorsteinsson, E.D. Waddington, W.D. Harrison, J.L. Morack, D.H. Elsberg and M.A. Zumberge, 2011. The crossover stress, anisotropy and the flow law at Siple Dome, West Antarctica, *J. Glaciol.*, **57**(201), 39–52.
- PISM, <http://www.pism-docs.org/>. Parallel Ice Sheet Model, fevor branch.
- Svensson, A., S.W. Neilsen, S. Kipfstuhl, S.J. Johnsen, J.P. Steffensen, M. Bigler, U. Ruth and R. Röthlisberger, 2005. Visual stratigraphy of the North Greenland Ice Core Project (NorthGRIP) ice core during the last glacial period, *J. Geophys. Res.*, **110**(D2), D02108.

- Thorsteinsson, T., 2001. An analytical approach to deformation of anisotropic ice-crystal aggregates, *J. Glaciol.*, **47**(158), 507–516.
- Thorsteinsson, T., 2002. Fabric development with nearest-neighbor interaction and dynamic recrystallization, *J. Geophys. Res.*, **107**(B1,2014), 1–13.
- Thorsteinsson, T., E.D. Waddington, K.C. Taylor, R.B. Alley and D.D. Blankenship, 1999. Strain rate enhancement at Dye 3, Greenland, *J. Glaciol.*, **45**(150), 338–345.

Chapter 2

The evolution of ice crystal fabric in ice sheets and its link to climate history ¹

2.1 Abstract

The evolution of preferred crystal-orientation fabrics is strongly sensitive to the initial fabric and texture. A perturbation in climate can induce variations in fabric and texture in the firm. Feedbacks between fabric evolution and ice deformation can enhance these variations through time and depth in an ice sheet. We model the evolution of fabric under vertical uniaxial-compression and pure-shear regimes typical of ice divides. Using an analytic anisotropic flow law applied to an aggregate of distinct ice crystals, the model evolves the fabric and includes parameterizations of crystal growth, polygonization and migration recrystallization. Stress and temperature history drive the fabric evolution. Using this model, we explore the evolution of a subtle variation in near-surface fabric using both constant applied stress and a stress–temperature history based on data from Taylor Dome, East Antarctica. Our model suggests that a subtle variation in fabric caused by climate perturbations will be preserved through time and depth in an ice sheet. The stress history and the polygonization rate primarily control the magnitude of the preserved climate signal. These results offer the possibility of extracting information about past climate directly from ice fabrics.

2.2 Introduction

An ice crystal is highly anisotropic in its response to stress. An ice sheet is made up of an unfathomably large number of ice crystals oriented in a variety of directions (fabric) and of a variety of shapes and sizes (texture). Only when crystal orientations are uniformly distributed in space can the anisotropic behavior of each individual crystal be ignored – giving rise to isotropic behavior in response to stress. However, ice with a preferred orientation of ice crystals (fabric) will behave anisotropically in response to stress. Glen (1955) assumed isotropic behavior in his flow law that has gained wide acceptance in glaciology, as it successfully explained early field observations. Modern field measurements have shown some discrepancies with flow predicted by Glen’s flow law, many of which can be attributed to the fabric in the ice sheet (e.g. Thorsteinsson and others, 1999).

Paleoclimate reconstruction requires an understanding of flow history in order to relate the depth of the ice (containing the climate proxy) to its age. Changes in flow due to microstructure,

¹Published as Kennedy, J. H., Pettit, E. C., and Di Prinzio, C. L. (2013). The evolution of crystal fabric in ice sheets and its link to climate history. *Journal of Glaciology*, **59**(214), 357-373. doi:10.3189/2013JoG12J159

such as enhanced strain from fabric or impurity-enhanced ice flow (Paterson, 1991; Faria and others, 2009), need to be accounted for in the ice-flow models used in paleoclimate reconstruction. Flow disturbances can also reorder the layers of ice, altering the depth–age relation. This reordering can happen at any scale, and microstructural observations provide insights into the integrity of ice-core stratigraphy such as ice-core line-scanners (Svensson and others, 2005; Faria and others, 2010), optical and electron microscopy and X-ray diffraction and tomography (Faria and others, 2010). Further, microstructural changes often coincide with changes in ice chemistry. Ice with high numbers of grain boundaries, triple junctions and micro-inclusions may smear the signal for entrapped gases and dissolved ions (Faria and others, 2010). Detailed microstructural studies are needed for paleoclimate reconstruction to ensure the integrity of the depth–age relation, ice-core strata and the climate proxies. Microstructure itself, however, has not yet been able to reconstruct a record of past climate changes (it is not a climate proxy).

From the detailed microstructure studies that have been carried out in ice cores for both Antarctic and Greenlandic ice, it is well accepted that ice often develops a preferred crystal orientation (e.g. Paterson, 1991; Arnaud and others, 2000; Di Prinzio and others, 2005; Durand and others, 2007; Gow and Meese, 2007). Near ice divides, the pattern of crystal orientations, or fabric, is commonly a vertically oriented single-maximum or vertical-girdle fabric. The strength of the fabric typically increases through the depth of an ice sheet. The profile of fabric with depth at a particular site, however, depends on temperature and strain history. Paterson (1991) showed that Ice Age ice typically has a smaller crystal size and stronger fabric than Holocene ice, providing the first hint of a connection between paleoclimate and microstructure. A recent sonic velocity profile of Dome C, East Antarctica, has shown transitions in the fabric that correlate to glacial–interglacial transitions through the depth of the ice sheet (Gusmeroli and others, 2012). Furthermore, Pettit and others (2011) showed a strong correlation between $\delta^{18}\text{O}$, a known climate proxy, and fabric data, implying fabric records climate information. Therefore, fabric may become a climate proxy in the future.

The variable growth of snow crystals in the atmosphere is unlikely to be preserved in the snowpack, even though snow-crystal growth is highly dependent on the climate in which it is growing (Kobayashi, 1967). Once deposited, the crystals break to a small average size ($< 1\text{mm}^2$; Benson, 1962) with nearly random orientations, such that their size and orientation do not directly record atmospheric temperature (Hooke, 2005). After landing, snow crystals begin to grow and change shape immediately, due to temperature and vapor pressure gradients in the firn (Colbeck,

1983), and it is here that we expect the climate signal to be imprinted into the ice (Carns and others, 2010).

In polar regions, vapor deposition is the primary method of crystal growth in the upper firn. The deposition of vapor on a crystal face is anisotropic: deposition will favor either the basal or prism faces of the snow crystal, depending upon the temperature (Nelson and Knight, 1998). This process causes crystals with the preferred face parallel to the vapor-pressure gradient to grow more than crystals in a less favorable orientation. These crystals grow at the expense of other crystals; as average size of crystals increases, the number of crystals decreases (Colbeck, 1983). This causes the well-oriented crystals to be more likely to remain, while poorly oriented crystals disappear. Therefore, variations in texture and fabric are primarily due to variations in temperature and vapor-pressure gradient (Carns and others, 2010). Because temperature and vapor-pressure gradients are a function of accumulation rate, air temperature and wind strength, this firn crystal evolution process records the climate signal within the firn column. Observations from firn cores have shown a preferred orientation of crystals in the firn layer (Di Prinzio and others, 2005; Fujita and others, 2009, 2012).

Climate variables, including temperature, solar radiation, winds and accumulation rate, are not the only factors that control variations of texture and fabric in the firn. The mechanics of densification may cause crystals to break apart, and rotate as they are compressed. Because the underlying physics in this region is poorly understood and much beyond the scope of this paper, we assume here that these climate variables affect the initial orientation and size of the ice crystals due to changes in the firn air temperature, vapor-pressure gradient and accumulation rate. The magnitude and rate of change of these variables during a climate transition will determine how pronounced the initial fabric variation is.

The aim of this paper is to determine how well climate information, as recorded in the initial fabric, may be preserved throughout the depth of an ice sheet. We model the evolution of a climate-induced fabric variation below the firn-ice transition. The fabric is evolved in response to a stress-time profile in which the stress is either constant or varies in a similar way to a real ice divide. Specifically, our model follows a small block of ice as it travels along a particle path. The block of ice is made up of three layers of 8000 crystals or grains (each grain is considered to be a single crystal, and the terms could be used interchangeably throughout this paper; we will use the term crystal because it is the term most often associated with fabric). The model does not include the larger-scale feedbacks among ice with different rheological properties that may alter the stress

history along a particle path. Our goal here is to isolate the effects of crystal-scale processes on the evolution of fabric under uniaxial compression and pure shear.

In the following sections, we show which stress–temperature conditions can lead to a preservation of the fabric variation through tens of thousands of years and deep in the ice sheet divide. First, we provide a brief background on fabric evolution and the relevant crystal processes. We then describe our model in detail and introduce a new orientation distribution function (ODF) to describe the orientations of crystals. In the remaining sections, we describe and discuss the results of our experiments with both constant applied stresses and stress–time profiles from an ice divide.

2.3 Background

The deformation of a single ice crystal in response to stress is strongly anisotropic. Crystals shear easily along the slip systems in their basal planes, much like a deck of cards, while shear on other slip systems is nearly two orders of magnitude harder (Duval and others, 1983). This leads to crystals responding to applied stress by elongating in the direction of the tensile stress and rotating until its basal planes are perpendicular to the compressive stress (Azuma and Higashi, 1985; Alley, 1992; Van der Veen and Whillans, 1994). In polycrystalline ice (hereafter referred to as ice), the orientation of a crystal is defined by the crystallographic axis (c-axis) that is perpendicular to the basal plane. Ice with a random orientation of c-axes (uniform over the surface of the sphere) is considered isotropic, while ice with a preferred orientation of c-axes is anisotropic. Strongly anisotropic ice in simple shear can deform up to an order of magnitude faster than isotropic ice (Azuma, 1994; Castelnau and others, 1996; Thorsteinsson, 2001). Ice at depth in an ice sheet tends to have crystals with c-axes aligned vertically (e.g. Alley, 1992), so its flow is significantly affected by crystal fabric.

The state of stress in the central regions of an ice sheet is dominated by vertical compression combined with horizontal shear that increases in magnitude with depth and distance from the divide. Under this stress state, the crystals tend to align with basal planes oriented horizontally and their c-axes oriented vertically as they move deeper in the ice sheet through time; strengthening the fabric with depth. The rate at which crystals rotate (how quickly fabric evolves) depends primarily on strain rate, which is a function of temperature, impurity content, crystal orientation (Weerman, 1973; Budd and Jacka, 1989; Paterson, 1991), and neighboring crystal interactions (Thorsteinsson, 2002).

The evolution of fabric is significantly affected by three additional processes: normal crystal (grain) growth, polygonization and migration recrystallization (Alley, 1992). In solid ice, normal

crystal (grain) growth occurs through migration of crystal boundaries driven by energy differences across the boundary defined by boundary curvature, intrinsic properties (e.g. temperature, thickness, diffusivity of water molecules), and extrinsic material (e.g. impurities, bubbles). Almost every experimental and theoretical treatment of the intrinsic growth rate of an ice crystal describes growth rate by a parabolic growth law (Alley and others, 1986). The crystal diameter, D , increases with time as

$$D^2 = K(t - t_0) + D_0^2, \quad (2.1)$$

where K is the crystal-growth factor, t is time, t_0 is the time of the last recrystallization and D_0 is the crystal diameter at time t_0 . The crystal-growth factor, K , is

$$K = K_0 \exp\left(-\frac{Q}{\mathcal{R}T}\right), \quad (2.2)$$

where K_0 is a constant that depends on the intrinsic properties of the crystal boundaries, Q is the thermal activation energy, \mathcal{R} is the gas constant and T is the temperature. However, extrinsic materials reduce the rate of boundary migration and can be described by a drag force on the boundary (Alley and others, 1986). This drag effectively reduces the crystal-growth factor K .

Normal crystal growth is active throughout the depth of an ice sheet. Once the ice starts deforming, crystal-boundary migration is a function of strain energy and grain-boundary energy. In the special case of the crystals on either side of the boundary having the same strain energy, Eqn (2.1) will describe the crystal growth in deforming ice. Even though the crystals continue growing at depth, a stable crystal size is typically reached (below a certain depth) because polygonization counteracts crystal growth. Polygonization creates new crystal boundaries within large ice crystals, effectively dividing the crystal in two. Large crystals can become highly strained and experience differential stress, which is relieved by the organization of dislocations into a sub-crystal boundary (Alley, 1992). De La Chapelle and others (1998) determined that the minimum dislocation density needed to form a sub-crystal boundary is, $\rho_p = 5.4 \times 10^{10} \text{ m}^{-2}$.

Because polygonization depends upon a minimum dislocation density being reached, the rate of polygonization can be indirectly described through the rate of change of the dislocation density. Dislocation density changes due to two dominate processes: it increases due to work hardening and decreases due to the absorption of dislocations at the crystal boundary (Miguel and others, 2001). Therefore, the change in the dislocation density can be described as

$$\frac{\partial \rho}{\partial t} = \frac{||\dot{\mathbf{e}}||}{bD} - \alpha \rho \frac{K}{D^2} , \quad (2.3)$$

where the first term on the right-hand side describes work hardening: $||\dot{\mathbf{e}}||$ is second invariant of the strain rate tensor, b is the length of the Burgers vectors and D is the crystal diameter (Montagnat and Duval, 2000). The second term describes the absorption of dislocations at the crystal boundaries: α is a constant and K is the crystal-growth factor.

Through most of the depth of an ice sheet, the rate of fabric evolution is a balance between crystal growth, polygonization and crystal rotation. However, migration recrystallization dominates fabric evolution at high temperatures (typically above approximately -10°C ; Duval and Castelnau, 1995). Migration recrystallization occurs when the stored strain energy (due to dislocations) in a crystal is greater than the crystal-boundary energy of a new strain-free crystal. The new strain-free crystal is nucleated and rapidly grows at the expense of the old crystal (Duval and Castelnau, 1995). The stored energy due to a dislocation density, E_d , can be estimated as

$$E_d \simeq \mu \rho G b^2 \ln \left(\frac{R_e}{b} \right) , \quad (2.4)$$

where G is the shear modulus, μ is a constant and R_e is the mean average of the dislocation strain field range (Thorsteinsson, 2002). The energy associated with crystal boundaries, E_c , is

$$E_c = \frac{3\gamma_g}{D} , \quad (2.5)$$

where γ_g is the energy per area on the boundary (for high-angle boundaries). When $E_d > E_c$ it is energetically favorable to nucleate a new crystal, which quickly grows to a diameter that scales with the effective stress (e.g., Shimizu, 1998). The crystal that grows rapidly will form in the most energetically favorable position: about halfway between the compressional and tensional axes, which maximizes the resolved shear stress on the basal planes causing them to deform easily (Alley, 1992). For uniaxial compression or pure shear, for example, this is 45° from the axis of compression. The grains are initially strain-free, and will have a much lower strain energy than the surrounding grains, allowing them to grow. As the new crystals grow preferentially at orientations favorable for the bulk deformation, the fabric can change significantly; in uniaxial compression, a strong vertical fabric will become a weaker small-circle girdle fabric (Budd and Jacka, 1989).

2.4 The model

Many models have been proposed to incorporate the effect of fabric into ice-sheet models. Gagliardini and others (2009) classify the variety of anisotropic polar ice models into four categories: phenomenological, full-field, homogenization and topological models.

Phenomenological models are large-scale ice-flow models that use a macroscopic formulation of the anisotropy of ice (e.g., Morland, 2002; Gillet-Chaulet and others, 2005; Placidi and others, 2009). The primary question these models answer is how the anisotropy of ice affects the flow of a glacier or ice sheet. These models are designed for flow studies; computational efficiency is paramount and the anisotropy of ice is parameterized and limited to a few special cases. These models typically represent large areas (m^2 to km^2) for each representative sample of ice and fabrics are not passed along flowlines. This entire class of model is unsuitable for our application because we are interested in the evolution of small-scale (cm^2 to m^2) subtle variations in fabrics as they move along their flowlines.

At the other end of the scale lie the full-field models. These models solve the Stokes equations by decomposing each crystal into many elements, allowing the stress and strain-rate heterogeneity to be inferred at the microscopic scale (e.g., Meyssonier and Philip, 2000; Lebensohn and others, 2004). These models are concerned with the microscopic processes within the ice crystal and at the boundaries of the ice crystal. They are generally two-dimensional models and become increasingly computationally difficult as the number of crystals is increased, limiting their application to a small number of crystals. These models are unsuitable for our application because the limited number of crystals does not allow for a statistically significant description of fabric on the scale of an ice sheet.

Homogenization models (also called micro-macro models) are used to derive the polycrystalline behavior of the ice from the behavior of single crystals (e.g., Lliboutry, 1993; Castelnau and Duval, 1994; Van der Veen and Whillans, 1994; Gördert, 2003; Gillet-Chaulet and others, 2006). These models compute the macroscopic (bulk) behavior by averaging over the microscopic (crystal) behavior. Generally these models are primarily focused on the evolution of fabric and describe the fabric as either a discrete or continuous orientation distribution. The topological models (e.g., Azuma, 1994; Thorsteinsson, 2002) are a sub-class of the homogenization models that include topological information by taking into account neighbor influences; a crystal surrounded by 'hard' crystals will be less likely to deform regardless of its orientation. Sarma and Dawson (1996) showed that nearest-neighbor interactions are essential to determining the single-crystal strain given a bulk equivalent strain. Thorsteinsson's (2002) model is the only topological model to in-

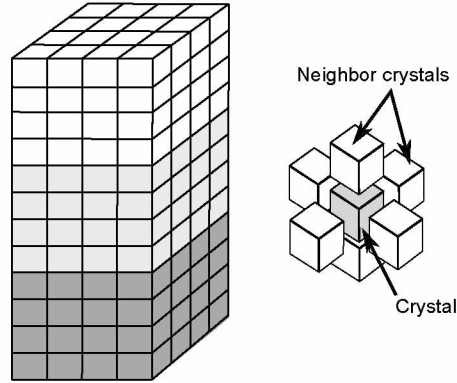


Figure 2.1: The polycrystal structure. Left: an example of a polycrystalline cuboid with three distinct fabric layers; the top layer is white, the middle layer light gray and the bottom layer dark gray. Each small cube indicates one crystal and each layer has $4 \times 4 \times 4 = 64$ crystals. The three-layered cuboid in our model has $20 \times 20 \times 20 = 8000$ crystals in each layer. Right: an illustration of the crystal packing where each crystal (gray) has six neighboring crystals (white).

corporate crystal growth, rotation and dynamic recrystallization into the fabric evolution. Since the recrystallization processes significantly affects the evolution of crystal fabric (Alley, 1992), we use the model developed by Thorsteinsson (2001, 2002) to study the fabric evolution throughout the depth of an ice sheet near a divide. It is important to note that this model is a polycrystal model that solves for fabric evolution and behavior, not a flow model. This model alone will not capture the deformation–fabric feedbacks due to the redistribution of stress (as a result of spatial variations in rheology) within the ice sheet. However, the model could be integrated into an ice-sheet flow model in order to capture this feedback.

The model uses a representative distribution of N individual ice crystals to calculate the bulk response of the ice to stress by averaging over the crystals. The crystals are arranged on a regular cuboidal grid (Figure 2.1), where each crystal has six nearest neighbors. The crystals, however, are considered to evolve independently of each other and are embedded in an ice matrix consisting of small crystals, which accommodate the crystal-boundary migration and act as seeds for migration recrystallization (Thorsteinsson, 2002). Because these crystals are small, they do not contribute significantly to the bulk deformation of the ice. In the case of nearest-neighbor interactions, the crystals are only able to feel that there is a hard or soft crystal nearby and the interaction only affects the crystals' resolved shear stress (Eqn (2.10), below). Each layer in the cuboid can be given a sub-distribution of crystals with its own fabric, and the response of each layer to an applied stress can be calculated through time.

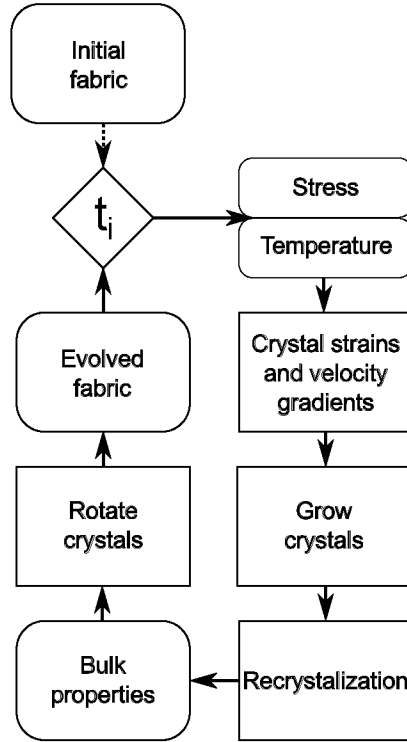


Figure 2.2: Flow chart of the model. The model is initialized with fabric data, deviatoric stress and temperature. For each time-step, strain rates and velocity gradients are calculated, dynamic recrystallization processes are applied to the fabric and then the crystals are rotated to calculate new fabric data. The new fabric data as well as new stresses and temperatures are fed back into the model to start the next time-step.

Each crystal in the distribution has an associated orientation given by the co-latitude, θ , and azimuth, ϕ , as well as an associated spherical size of diameter D and dislocation density ρ . The model takes in an initial crystal distribution, stress and temperature and evolves the crystals through uniform steps in time or strain; Figure 2.2 outlines the model process. First, the model creates an initial crystal distribution by the method described in the next subsection. The model then applies a stress to the crystal distribution and calculates the individual crystal strain rates and velocity gradients using the analytic flow law developed by Thorsteinsson (2001, 2002). Next, it checks the recrystallization conditions (outlined below) and then rotates the crystals. After each time- or strain-step, the model outputs the new distribution of crystals, the bulk strain and the number and type of recrystallization events. This new distribution of crystals is then fed back into the model for the next time-step along with the new stress and temperature.

In this model, stress is an input; the stress, therefore, must be determined outside the model.

2.4.1 Crystal physics

Ice crystals rotate as a result of the velocity gradient experienced. The velocity gradient is a result of the internal stresses experienced by the ice sheet, and these stresses lie somewhere between two end members: uniform stress and uniform strain rates. Due to the strong crystal anisotropy, the uniform-stress assumption has been shown to be well adapted to describing polycrystalline ice (Castelnau and others, 1996). Therefore, we apply a uniform stress to each crystal in the distribution. We restrict the deformation of the crystal to the basal plane; therefore, the crystal only responds to the components of stress that are in the basal plane (termed the resolved shear stress; RSS). The Schmidt tensor, \mathbf{S} , describes the orientation of the crystal, \vec{c} , relative to the slip directions and has the form

$$\mathbf{S}^{(s)} = \vec{b}^{(s)} \otimes \vec{c} . \quad (2.6)$$

where (s) refers to the slip system, $\vec{b}^{(s)}$ is the direction (Burgers vector) of the slip system and \otimes is the vector direct (dyadic) product. Then the RSS, $\tau^{(s)}$, on a slip system is

$$\tau^{(s)} = \mathbf{S}^{(s)} : \boldsymbol{\sigma} , \quad (2.7)$$

where $\boldsymbol{\sigma}$ is the deviatoric stress tensor for the stress applied to the fabric and $\mathbf{S}^{(s)} : \boldsymbol{\sigma} = S_{kl}^{(s)} \sigma_{kl}$ summing over repeated indexes. The magnitude of the RSS, \mathcal{T} , can then be calculated as

$$\mathcal{T} = \left| \sum_{(s)} \tau^{(s)} \vec{b}^{(s)} \right| . \quad (2.8)$$

Using the analytic flow law (Thorsteinsson, 2001, 2002) the velocity gradient of a crystal, \mathbf{L}^c , in response to a stress is

$$\mathbf{L}^c = \beta \mathcal{A} \sum_s \mathbf{S}^{(s)} |\mathcal{E}^c \tau^{(s)}|^{n-1} (\mathcal{E}^c \tau^{(s)}) , \quad (2.9)$$

where β is a constant, \mathcal{A} is the flow parameter from Glen's flow law (Paterson, 1994, p. 97), \mathcal{E}^c is the local softness parameter due to explicit nearest-neighbor interactions (NNI) of the ice crystals and n is the exponent in Glen's flow law (Glen, 1955). The local softness parameter averages the magnitude of the RSS on a crystal's six nearest neighbors relative to the magnitude of the RSS it is experiencing, \mathcal{T}^0 :

$$\mathcal{E}^c = \frac{1}{\zeta + 6\xi} \left(\zeta + \xi \sum_{i=1}^6 \frac{\mathcal{T}^i}{\mathcal{T}^0} \right), \quad (2.10)$$

where ζ is the relative contribution of the center crystal, ξ is the relative contribution of each neighbor and $i = 0$ refers to the center crystal and $i = 1, \dots, 6$ refers to each of the six nearest neighbors (Figure 2.1). Because the RSS can be zero, there is a specified roof for the maximum value of \mathcal{E}^c . Setting $[\zeta, \xi]$ to $[1, 0]$ in Eqn (2.10) is equivalent to the homogeneous stress assumption where, there is no NNI. Changing the values of $[\zeta, \xi]$ modifies the homogeneous-stress (toward the homogeneous-strain) assumption by redistributing the stress through explicit NNI. Using the values $[6, 1]$ means the center crystal contributes as much as all the neighbors together, and $[1, 1]$ means the center crystal and all the neighbors contribute equally.

Finally, the strain rate of a single crystal, $\dot{\mathbf{e}}^c$, is

$$\dot{\mathbf{e}}^c = \frac{1}{2} \left[\mathbf{L}^c + (\mathbf{L}^c)^T \right], \quad (2.11)$$

where $()^T$ indicates the matrix transpose.

2.4.2 Rotating crystals

In each time-step, the crystals are rotated from an orientation, \vec{c} , to a new orientation, \vec{c}' . If the surrounding ice is fixed, each crystal rotates as it deforms according to the standard continuum mechanics rotation rate tensor:

$$\dot{\mathbf{\Omega}}^p = \frac{1}{2} \left[\mathbf{L}^c - (\mathbf{L}^c)^T \right], \quad (2.12)$$

where $\dot{\mathbf{\Omega}}^p$ is the rotation rate of a single crystal and \mathbf{L}^c is the velocity gradient of a crystal in response to stress from Eqn (2.9). If the surrounding ice is rotating within the frame of reference, however, the model calculates a relative crystal rotation rate:

$$\dot{\mathbf{\Omega}}^* = \dot{\mathbf{\Omega}}^b - \dot{\mathbf{\Omega}}^p, \quad (2.13)$$

where $\dot{\mathbf{\Omega}}^b$ is the bulk rotation rate of the modeled ice in response to stress. The bulk rotation rate is

$$\dot{\mathbf{\Omega}}^b = \frac{1}{2} \left[\mathbf{L}^m - (\mathbf{L}^m)^T \right] + \dot{\mathbf{\Omega}}^d, \quad (2.14)$$

where \mathbf{L}^m is the bulk velocity gradient of the modeled ice (calculating bulk properties is discussed in the next subsection), and $\dot{\mathbf{\Omega}}^d$ is the rotation rate necessary to add to the modeled bulk rotation rate in order to satisfy the boundary conditions. For example, irrotational deformations (e.g. uniaxial compression, pure shear) should have no bulk rotation of the ice ($\dot{\mathbf{\Omega}}^b = 0$), making

$$\dot{\mathbf{\Omega}}^d = -\frac{1}{2} \left[\mathbf{L}^m - (\mathbf{L}^m)^T \right] . \quad (2.15)$$

Therefore, the new orientation of the crystal is

$$\vec{c}' = (\mathbf{I} + t\dot{\mathbf{\Omega}}^*)\vec{c} \quad (2.16)$$

where t is the time-step.

2.4.3 Bulk properties

The bulk properties are calculated by averaging the single-crystal properties and will be influenced more by the larger crystals than the smaller crystals. We calculate the volume of a crystal from its diameter, D , and use its volume fraction, f , as a statistical weight for the calculation of the bulk properties (Gagliardini and others, 2004). Any bulk property, \mathbf{Y} , of a single-crystal property, \mathbf{Y}^c , is then

$$\mathbf{Y} = \sum_{n=1}^N f_n \mathbf{Y}_n^c , \quad (2.17)$$

where

$$f_n = \frac{D_n^3}{\sum_{m=1}^N D_m^3} . \quad (2.18)$$

Therefore, the modeled bulk velocity gradient is

$$\mathbf{L}^m = \sum_{n=1}^N f_n \mathbf{L}_n^c , \quad (2.19)$$

where N is the number of crystals in the fabric. Likewise, the bulk strain rate is

$$\dot{\mathbf{\epsilon}} = \sum_{n=1}^N f_n \dot{\mathbf{\epsilon}}_n^c . \quad (2.20)$$

Table 2.1: Values of the parameters used in the model.

Parameter	Value	Equation	Source
Initial crystal diameter, D_0	1.5 mm	Eqn (2.1)	Benson (1962)
Crystal-growth constant, K_0	$8.2 \times 10^{-9} \text{ m}^2 \text{ s}^{-1}$	Eqn (2.2)	Alley and others (1986); Thorsteinsson (2002)
Thermal activation energy, Q	40 kJ mol^{-1}	Eqn (2.2)	Alley and others (1986); Thorsteinsson (2002)
Dislocation absorption constant, α	1	Eqn (2.3)	De La Chapelle and others (1998); Montagnat and Duval (2000)
Dislocation energy constant, μ	0.035	Eqn (2.4)	Mohamed and Bacroix (2000); Thorsteinsson (2002)
Dislocation strain field range, R_e	$\frac{1}{\sqrt{\rho}}$	Eqn (2.4)	Mohamed and Bacroix (2000)
Crystal boundary energy, γ_g	0.065 J m^{-2}	Eqn (2.5)	Ketcham and Hobbs (1969)
Flow law constant, β	630	Eqn (2.9)	Thorsteinsson (2001)
Polygonization ratio, δ	0.065		Thorsteinsson (2002)
Polygonization orientation change, $\Delta\theta$	5°		Thorsteinsson (2002)
Initial dislocation density, ρ_0	10^{10} m^{-2}		De La Chapelle and others (1998)

2.4.4 Crystal processes

The crystals are additionally affected by normal crystal growth and the recrystallization processes of polygonization and migration recrystallization. Normal crystal growth is implemented by growing the diameter of the crystal, D , according to Eqn (2.1). Though the ice is deforming, we assume that the small crystals that surround the modeled ice crystal have an average strain energy comparable with the modeled crystal, such that the strain energy does not add to the grain-boundary migration rate. The dislocation density of the crystal also grows, according to Eqn (2.3). The recrystallization processes are outlined below. Once a crystal has undergone a recrystallization event, it will start to evolve again according to Eqn (2.1) and (2.3).

Polygonization

We model polygonization using a proxy for differential stress on a crystal (Thorsteinsson, 2002). Crystals that have a small component of shear stress resolved on to the basal plane (RSS) will likely be experiencing a differential stress from their neighboring crystals which are deforming. If the

ratio of the magnitude of the RSS, \mathcal{T} , to the second invariant of the applied stress, $\|\boldsymbol{\sigma}\|$ is less than a given value ($\mathcal{T}/\|\boldsymbol{\sigma}\| < \delta$) and the dislocation density, ρ , in the crystal sufficient to form a sub-crystal wall ($\rho > \rho_p$), then the crystal can polygonize. When a crystal polygonizes, the orientation is changed by an angle, $\Delta\theta$, in a direction that increases the RSS, the crystal size is halved and the dislocation density is reduced by ρ_p . Polygonization tends to slow the development of fabric, because crystals that are oriented very close to the preferred orientation (small RSS) of the fabric will polygonize preferentially by the selection criteria (weakening the fabric).

Migration recrystallization

We model migration recrystallization by immediately nucleating a new crystal once the dislocation energy, E_d , is greater than the boundary energy, E_c (Eqn (2.4) and (2.5)). The old crystal is replaced with the new ‘strain-free’ crystal, with dislocation density ρ_0 and a diameter that scales with the effective stress, $D \sim (\sigma_{kl}\sigma_{kl}/2)^{-2/3}$. The rapid crystal-boundary migration is assumed to be fast enough to grow to a diameter D within a single time step. The ‘strain-free’ crystal is given the ‘softest’ orientation, or orientation with the highest RSS, of a random set of orientations in the applied stress state (Thorsteinsson, 2002). In uniaxial compression, this is close to the small circle 45° off the compression axis.

Model parameters

Table 2.1 lists each parameter used, which section and equation it can be found in, and the relevant reference(s).

2.5 Generating initial crystal distributions

To generate our initial fabrics, we use a finite number of crystals randomly selected from an orientation distribution function (ODF) to represent the ice we are modeling. Each layer of our cuboid (as shown in Figure 2.1) can be given a unique ODF and thereby a unique fabric. The layers are then put together to form our initial crystal distribution.

Orientation distribution functions provide a continuous description of the volume fraction of ice crystals in a certain orientation. This reduces to the relative number of ice crystals in an orientation if every crystal has the same volume. Because thin-section measurements from ice cores provide only a limited snapshot of the ODF *in situ*, a general ODF is needed to describe the variety of fabrics observed in ice sheets.

It is important to remember that ice crystals are axially symmetric; they have no inherent ‘up’ or ‘down’ direction. Therefore, the orientation of a single ice crystal can equally be described by two unit vectors pointing in opposite directions, \vec{c} and $-\vec{c}$, corresponding to the two points on opposite sides of the unit sphere where the axis passes through. Because of this symmetry, the space of all possible orientations can be reduced to the upper hemisphere of the unit circle. Every axis will have one end pass through a point on the upper hemisphere, while the other end will pass through a corresponding point (reflected through the origin) on the lower hemisphere. Thus an ODF that preserves this axial symmetry can be defined on the upper hemisphere alone (the unit vector space is *restricted* to the upper hemisphere). Defined as such, the ODF, p , must be normalized such that the total volume fraction is equal to 1, or

$$1 = \frac{1}{2\pi} \oint_{S/2} p(\vec{c}) d\vec{c} , \quad (2.21)$$

where $S/2$ is the surface of the upper hemisphere of the unit sphere, S . Alternately, an ODF, P , could be defined over the whole unit sphere (the unit vector space is *unrestricted*) such that both ends of the axis carry half the probability of finding a crystal in that orientation ($P(\vec{c}) = P(-\vec{c})$). Again P must be normalized, such that the total volume fraction is equal to 1, or

$$1 = \frac{1}{4\pi} \oint_S P(\vec{c}) d\vec{c} . \quad (2.22)$$

It is mathematically equivalent to use either a restricted or unrestricted distribution and, thus far, every ODF proposed in the glaciology literature has been a restricted distribution (Gagliardini and others, 2009).

We use an unrestricted distribution called the Watson distribution, the simplest well-known axial distribution in directional statistics (Fisher and others, 1987; Mardia and Jupp, 2000). The Watson distribution (Watson, 1965) is defined over the *whole* unit sphere as

$$w(\vec{c}) = a_k^{-1} \exp[-k(\vec{\eta}^T \vec{c})^2] , \quad (2.23)$$

where $k \in [-\infty, \infty]$ is the concentration parameter, $\vec{\eta}$ is the principal axis of the distribution and a_k is the normalizing constant. If we set $u = \vec{\eta}^T \vec{c}$, the normalizing constant is

$$a_k = 2 \int_0^1 \exp(-ku^2) du . \quad (2.24)$$

The Watson Distribution preserves axial symmetry, $w(\vec{c}) = w(-\vec{c})$ and is rotational symmetric around its principal axis, $\vec{\eta}$. If the principal axis is pointing vertically, $\vec{\eta} = [0, 0, 1]$, the Watson distribution can be written as

$$w(\theta, \phi) = a_k^{-1} \exp[-k \cos^2(\theta)] , \quad (2.25)$$

where θ and ϕ are the co-latitude and azimuth angles.

The Watson distribution describes single-maximum fabrics when $k < 0$, equatorial-girdle fabrics when $k > 0$, and reduces to the uniform (isotropic) distribution when $k = 0$. Fortunately, these are the most common types of fabrics observed in ice cores (Paterson, 1994). Additionally, if there is a sample of N observations of axis positions, the Watson distribution's concentration parameter and principal axis can be determined from the eigenvalues and vectors of $\sum_{n=1}^N f_n \vec{c}_n \otimes \vec{c}_n$, the familiar orientation tensor used to analyze ice-core thin sections (Woodcock, 1977; Gagliardini and others, 2004). Therefore, we can connect the concentration parameter and the principal axis of the Watson distribution to an observed fabric (described in the next subsection).

Although unrestricted distributions have not been used previously in the glaciology literature, the Watson distribution is closely related to the Fisher distribution, the best known vectorial (not axial) distribution in the field of directional statistics (Fisher and others, 1987; Mardia and Jupp, 2000). Lliboutry (1993) proposed a restricted form of the Fisher distribution to use as an ODF in glaciology, but abandoned it due to the computational difficulties. Later, Gagliardini and others (2009) showed that for Dome C, the restricted Fisher distribution best fit the observed distribution of crystals, as compared to the other ODFs used in the glaciology literature, even though it has never been applied in glaciology. The Fisher distribution, \mathcal{F} , is defined as

$$\mathcal{F}(\vec{c}) = f_\kappa^{-1} \exp[\kappa \vec{\eta}^T \vec{c}] \quad (2.26)$$

where f_κ^{-1} is a normalizing constant, $\kappa \in [0, \infty]$ is the concentration parameter, $\vec{\eta}$ is the principal axis of the distribution and \vec{c} is a crystal orientation (unit) vector (Fisher, 1953). When the principal axis, $\vec{\eta}$, is vertical, the density of the distribution reduces to $\exp(\kappa \cos(\theta))$, where θ is the co-latitude angle. The Fisher distribution describes single-maximum fabrics when $\kappa > 0$, and reduces to the uniform (isotropic) distribution when $\kappa = 0$. Unfortunately, the Fisher distribution cannot describe girdle fabrics and it is not axially symmetric ($\mathcal{F}(\vec{c}) \neq \mathcal{F}(-\vec{c})$) so must be used in the restricted unit vector space for ice crystals. Watson (1982) showed that an axial form of the (unrestricted) Fisher distribution can be created by replacing θ with 2θ , thereby creating a bipolar distribution.

By noticing that $\exp[\cos(2\theta)] \propto \exp[\cos^2(\theta)]$ we arrive back at the Watson distribution, which, by choosing an appropriate k , can be used in place of Lliboutry's restricted Fisher distribution, with the added benefit of being able to describe girdle fabrics.

2.5.1 Orientation tensor

The orientation tensor, built from the orientation of each crystal in a polycrystal, is used to determine the strength of the fabric in the ice (Woodcock, 1977; Gagliardini and others, 2004). The orientation tensor is calculated from a polycrystal of N crystals as

$$\mathbf{A} = \sum_{n=1}^N f_n \vec{c}_n \otimes \vec{c}_n, \quad (2.27)$$

where f_n is the crystal's volume fraction (Eqn (2.17)). The eigenvalues (e_i for $i = 1, 2, 3$) and eigenvectors (\vec{v}_i) are then calculated from \mathbf{A} . The eigenvalues are said to describe the spatial strength of the fabric and the eigenvectors form the *best* material symmetry basis. Alternately, the eigenvalue, e_i , can be considered the fractional variance of the distribution along the eigenvector, \vec{v}_i . The eigenvalues are arbitrarily sorted, such that $e_1 > e_2 > e_3$, and \vec{v}_1 gives the direction of the 'strongest' fabric. An axially symmetric single-maximum distribution will have eigenvalues such that $e_1 > e_2 = e_3$ and the principal axis will be \vec{v}_1 ; the points will all be clustered around \vec{v}_1 (most of the variance is along \vec{v}_1). While an axially symmetric equatorial-girdle distribution will have eigenvalues such that $e_1 = e_2 > e_3$, the points will be clustered around the equator of a sphere with a pole axis \vec{v}_3 (most of the variance is along both \vec{v}_1 and \vec{v}_2).

If our crystals are considered a random sample of a Watson distribution, then the eigenvalues and eigenvectors of the orientation tensor allow us to estimate the concentration parameter, k , of the Watson distribution (Watson, 1965). Fisher and others (1987, p. 176), and Mardia and Jupp (2000, p. 202) show that the maximum-likelihood estimate (MLE) of the concentration parameter, k , is the solution of

$$\mathcal{D}(z) = \frac{\int_0^1 u^2 \exp(-zu^2) du}{\int_0^1 \exp(-zu^2) du}, \quad (2.28)$$

where u is the same as in Eqn (2.24); $\mathcal{D}(z) = e_1$ and $z = k$ for a bipolar distribution and $\mathcal{D}(z) = e_3$ and $z = -k$ for a equatorial girdle distribution. Both Fisher and others (1987) and Mardia and Jupp (2000) give methods to reasonably approximate the solution to Eqn (2.28). Further, we know the principal axis of the distributions will be

$$\begin{cases} \vec{\eta} = \vec{v}_1 & \text{for a bipolar distribution} \\ \vec{\eta} = \vec{v}_3 & \text{for an equatorial-girdle distribution,} \end{cases}$$

from the eigenvectors of the orientation tensor. The Watson distribution can thus be calculated to have a fabric that is analogous to a thin section's fabric.

Taking the Watson distribution to be our general ODF has a few distinct advantages over other proposed ODFs. The Watson distribution is inherently axial, like our ice crystals, and it can be generated directly from the observed properties of a thin section. It describes single-maximum, equatorial-girdle and isotropic fabrics, the most common observed in ice cores. Further, it is a well-known distribution in directional statistics (Fisher and others, 1987; Mardia and Jupp, 2000). This allows use to use the statistical tools, such as MLE, developed in a variety of disciplines, from nuclear magnetic resonance imaging (Cook and others, 2004) to the movement of robots (Palmer and Fagg, 2009) and many others. (See Fisher and others (1987) and Mardia and Jupp (2000) for more information about the statistical tools that have been developed for this and other spherical distributions.)

We generate our initial fabrics for our model through random sampling of the Watson distribution (Ulrich, 1984; Li and Wong, 1993; Wood, 1994). Each crystal is assumed to have the same crystal size, and therefore the Watson distribution describes the relative fraction of crystals in a particular orientation. We model the distributions on the fabrics observed at Taylor Dome, Antarctica (as described below).

2.6 Constant stress experiments

In order to determine whether a subtle variation in fabric could be preserved over time, we model the application of constant stress on a cuboid that has three 8000-crystal layers, where the middle layer is initialized with a different fabric than the top and bottom layers. The initial fabric for the top and bottom layers is generated with a concentration parameter for the Watson distribution of $k = -2.0$ ($e_1 = 0.538$) while the middle layer has a concentration parameter of $k = -2.4$ ($e_1 = 0.567$). These concentration parameters are chosen to correspond with fabrics at 100m depth in Taylor Dome (described below). A contoured Schmidt plot of the fabrics is shown in Figure 2.3. At each time-step, a constant temperature, T , and stress, σ , is applied to the fabric. We chose our temperature to be $T = -30^\circ\text{C}$: the approximate average temperature of the Antarctic ice sheet. This temperature is well below our cut-off temperature for migration recrystallization, which is there-

Table 2.2: Summary of the run setup of our constant-stress experiments.

Run	σ	NNI $[\zeta, \xi]$	σ bar
1	Uniaxial compression	None $[1, 0]$	-0.1
2			-0.4
3		Mild $[6, 1]$	-0.1
4			-0.4
5		Full $[1, 1]$	-0.1
6			-0.4
7	Pure shear	None $[1, 0]$	-0.1
8			-0.4
9		Mild $[6, 1]$	-0.1
10			-0.4
11		Full $[1, 1]$	-0.1
12			-0.4

fore not active in the results presented here. We apply the stress states of uniaxial compression and pure shear to our fabric. The deviatoric stress tensor for uniaxial compression has the form

$$\sigma = \begin{pmatrix} \frac{1}{2}\sigma & 0 & 0 \\ 0 & \frac{1}{2}\sigma & 0 \\ 0 & 0 & -\sigma \end{pmatrix}, \quad (2.29)$$

and the deviatoric stress tensor for pure shear has the form

$$\sigma = \begin{pmatrix} \sigma & 0 & 0 \\ 0 & 0 & 0 \\ 0 & 0 & -\sigma \end{pmatrix}. \quad (2.30)$$

We use σ values 0.1 and 0.4bar to provide a lower and upper bound on the characteristic deviatoric stresses typically seen in ice sheets (Pettit and Waddington, 2003). The model calculates a strain rate at a time-step, and then the fabric is evolved for the amount of time required to achieve a strain-step of 0.001, until a total strain of 0.35 is reached. After 0.35 strain, the time-step necessary for a 0.001 strain-step has increased by over two orders of magnitude, due to stress hardening, and preliminary model runs suggest that the separation in eigenvalues between the layers will drop below 0.01 for most of our experiments. The nearest-neighbor interaction parameters (Eqn (2.10)) were varied for different model runs. Table 2.2 shows the model set-up for each run.

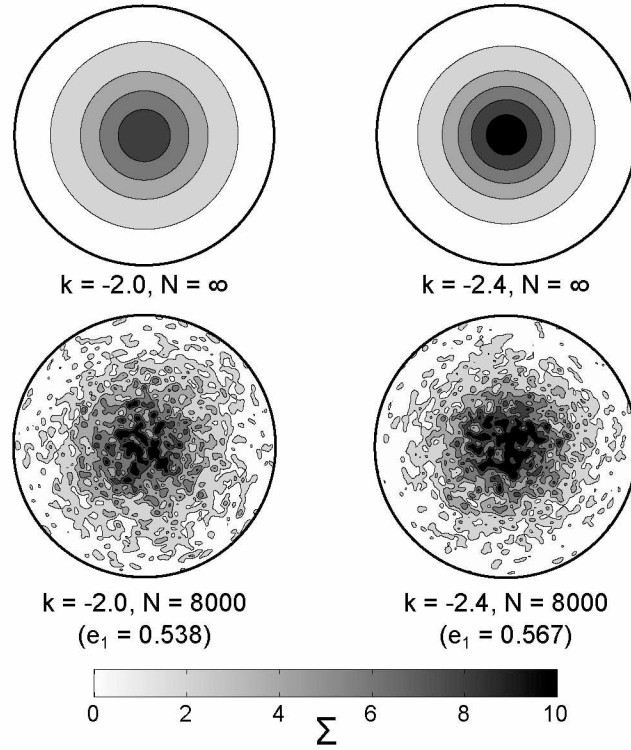


Figure 2.3: Contoured Schmidt plot of the initial fabrics for both the constant stress and Taylor Dome experiments. The fabrics are contoured at levels of $0, 2\Sigma, \dots, 10\Sigma$ where Σ is the standard deviation of the density of crystals from the expected density for isotropic ice (Kamb, 1959). The top two plots are contour plots of the continuous Watson distribution (an infinite number of crystals) with concentration parameters $k = -2.0$ (left) and $k = -2.4$ (right). Two random 8000 crystal fabrics were generated from these Watson distributions, as shown in bottom two plots. The fabric generated from the $k = -2.0$ and $k = -2.4$ distributions have eigenvalues of $e_1 = 0.538$ and $e_1 = 0.567$, respectively. The concentration parameter of $k = -2.4$ is consistent with a fabric at 100m depth in Taylor Dome, and the concentration parameter of $k = -2.0$ was picked to make a fabric that is slightly more isotropic.

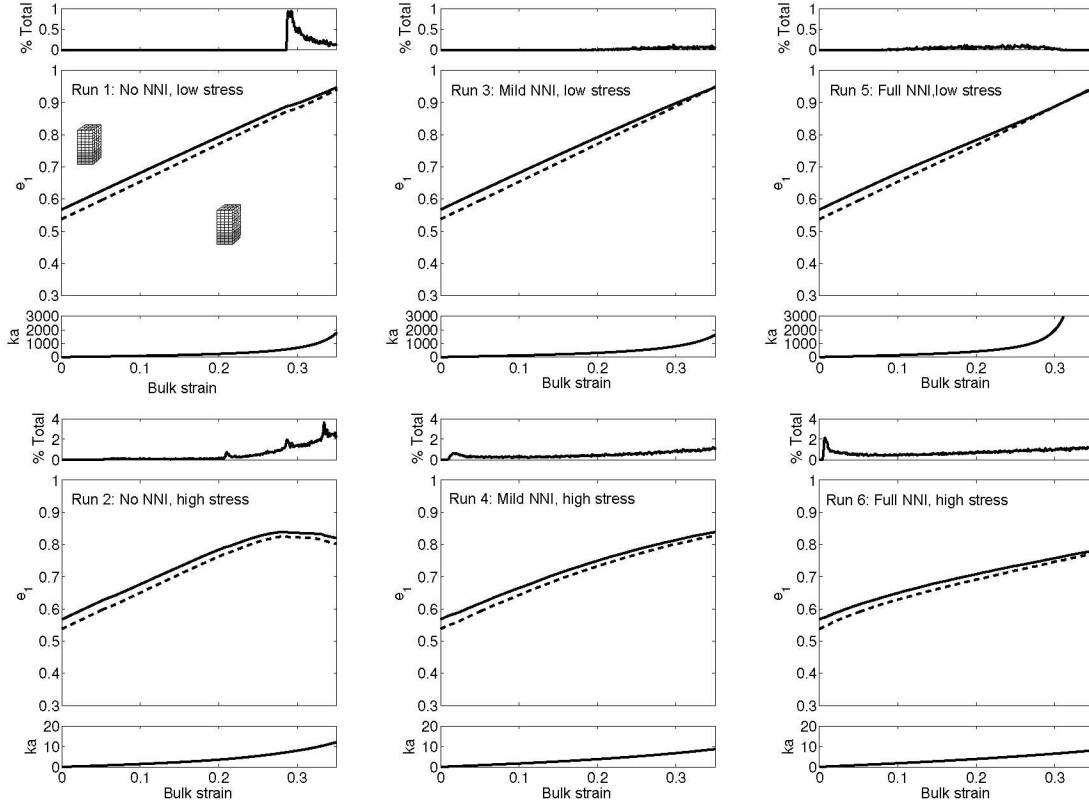


Figure 2.4: The uniaxial-compression runs, 1-6 (Table 2.2). The top row shows the low-stress runs and the bottom row the high-stress runs. The left column shows no nearest-neighbor interaction ($[\zeta, \xi] = [1, 0]$; Eqn (2.10)), the middle column shows mild nearest-neighbor interaction ($[\zeta, \xi] = [6, 1]$) and the right column shows full nearest-neighbor interaction ($[\zeta, \xi] = [1, 1]$). For each run, the top plot shows the number of crystals that recrystallize within each strain-step, as a percentage of the total number of crystals. The middle plot shows the evolution of the largest eigenvalue, e_1 , for the middle layer (solid curve) and the top and bottom layer (dashed curve). The bottom plot shows the total model time at each strain-step.

2.6.1 Results

Figure 2.4 shows the evolution of the e_1 eigenvalues, the number of polygonization events and the model time for each strain step in the uniaxial-compression tests (runs 1-6 in Table 2.2). A uniaxial-compression stress environment causes an increase in the fabric strength. For the low-stress runs (1,3 and 5) polygonization is not active initially because the strain rate is too low to generate dislocations faster than they are being destroyed by recovery processes, unlike the high-stress runs (2,4 and 6). As the crystals grow, however, the absorption of dislocations at crystal boundaries decreases, triggering polygonization events even as the strain rates decrease due to

work hardening. The effect of NNI in these experiments is to change the timing and rate of polygonization. Nearest-neighbor interactions distribute stress among crystals, such that they are no longer all experiencing the same effective stress. This modification of the stress distribution tends to cause polygonization events to be evenly distributed in time, rather than tightly clustered at a threshold strain. In each run, when polygonization becomes active, there is a corresponding reduction in the rate of evolution (slope of the middle graph).

Figure 2.5 shows the separation between the eigenvalues, e_1 , of the middle and top/bottom layers for runs 1-6. In all cases, we see the separation of the eigenvalues reduced over time because, when all other effects are equal, the rotation rate decreases as the fabric strengthens. However, the separation of eigenvalues reduces slowly enough that the fabric variation is measurable for up to at least 0.30 bulk strain. This reduction in the eigenvalue separation happens because each layer's fabric nears its stress-equilibrium state. All three layers will ultimately approach the same equilibrium fabric because they are under the same stress and temperature, and have the same material properties (e.g. impurity content). Polygonization events tend to slow down fabric evolution, which can result in an increase of the separation if the polygonization events dominate the fabric evolution, as seen in the no NNI runs (1 and 2) at high bulk strains. Likewise, in the high stress NNI runs (2,4 and 6), polygonization is very active early in the evolution, due to the high strain rates. In these runs, polygonization and strain-induced rotation are close to being balanced, causing the separation to be maintained to higher bulk strains. The weaker fabric will have a higher strain rate, causing it to be slowed down more by the increased number of polygonization events. However, in the low-stress runs with mild and full NNI (3 and 5), the separation at any given bulk strain will be less than in runs without NNI, because the strain-induced rotation dominates the polygonization. The weaker fabric will be able to evolve faster than the stronger fabric, since it is not being slowed by many polygonization events.

Figure 2.6 shows the evolution of the e_1 eigenvalues, polygonization events and total strain for the pure-shear tests (runs 7-12 in Table 2.2). Similar to uniaxial compression, a pure shear environment causes a strengthening of the fabric. In the low stress runs (7, 9 and 11), polygonization events happen at a lower bulk strain, due to larger horizontal strain rates than in the uniaxial-compression runs. Similarly, polygonization is much more active for the high-stress-pure shear runs (8, 10 and 12) than for uniaxial-compression runs, resulting in the weakest fabrics after 0.35 strain among any of our experiments.

Figure 2.7 shows the separation between the eigenvalues, e_1 , of the middle and top/bottom layers for the pure-shear runs (7-12). As in the uniaxial-compression runs, we see the separation

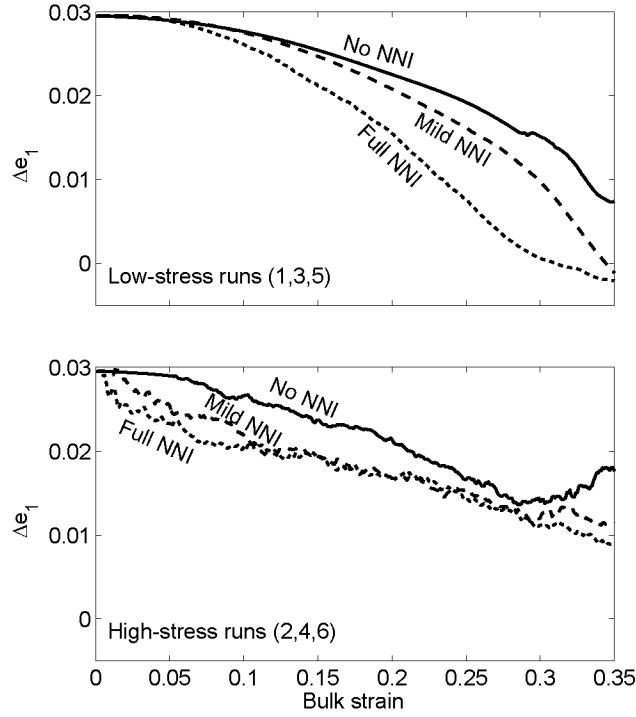


Figure 2.5: Separation of the largest eigenvalue, e_1 , between the top layer and middle layer for the uniaxial-compression runs, 1–6. The top plot shows the low-stress runs 1,3 and 5. The bottom plot shows the high-stress runs 2,4 and 6. The solid curves indicate runs 7 and 8 with no nearest-neighbor interaction ($[\zeta, \xi] = [1, 0]$; Eqn (2.10)), the dashed curves indicate runs 9 and 10 with mild nearest-neighbor interaction ($[\zeta, \xi] = [6, 1]$) and the dotted curves indicate runs 11 and 12 with full nearest-neighbor interaction ($[\zeta, \xi] = [1, 1]$).

of the eigenvalues decrease over time in all cases, yet remain measurable to at least 0.30 bulk strain. In the low-stress runs with NNI (9 and 11), polygonization starts at lower bulk strains, causing the separation to decrease more quickly than for the no NNI run (7). Polygonization is very active in the high-stress runs (8, 10 and 12), causing the separation to be maintained to a higher bulk strain than in any other test. Polygonization dominates the fabric evolution in the no NNI run (8), causing a large increase in the separation of the eigenvalues, that is more pronounced than in the uniaxial-compression runs.

2.7 Taylor dome experiments

Taylor Dome is a small peripheral dome (20 km \times 80 km) of the East Antarctic ice sheet, just inland of the Transantarctic Mountains, and provides ice to outlet glaciers entering Taylor Valley and McMurdo Sound. An ice core was drilled to bedrock on the summit of Taylor Dome ($77^\circ 47' 47'' S$, $158^\circ 43' 26'' E$) to a depth of 554m in 1994. Near the bed the ice is > 230 ka old; the depth-age

profile shown in Figure 2.8 (Steig and others, 1998, 2000). The ‘kink’ in the depth–age profile is synchronous with the last glacial–interglacial transition. The Taylor Dome ice core provides a stratigraphically undisturbed record through the entire last glacial cycle (Grootes and others, 1994).

Ice samples were cut from the ice core for thin-section microstructure analysis. Each thin section’s fabric was determined using an automatic ice fabric analyzer (Wilen, 2000; Hansen and Wilen, 2002; Wilen and others, 2003). The instrument consists of an optical bench that has two rotating stages containing polarized lenses. A thin section is mounted in a sample holder on the sample stage, between the crossed polarizers. A diffused light source illuminates the sample through one of the polarizers.

The ice fabric analyzer has a digital camera which measures the extinction angle of each pixel from the sample as it is rotated. The sample is rotated nine times in nine different positions. The extinction angle determines the plane containing the c -axis (up to 90°), and the plane intersections from the nine different positions determine the unique c -axis direction. Refraction corrections (analogous to Kamb corrections for manual technique) are included. A NI LabviewTM routine automatically calculates the angle between the c -axis and the z -axis (θ) and the angle between the projection of c -axis on the x - y plane and the x -axis (ϕ), for each grain. The error is $< 0.5^\circ$ for both θ and ϕ . This corresponds to an measurement error of less than ± 0.001 in the eigenvalues of the thin sections. The fabric profile with depth is shown in Figure 2.9. The eigenvalues vary by ± 0.1 in the top 200 m of Taylor dome; these variations are two orders of magnitude greater than the measurement error. Because of the low density of thin sections, it is not possible to distinguish whether these variations are due to climate, statistical fluctuations due to the number of measured crystals, or other microstructural processes. However, these variations are on the order of what we expect from climate variations and, when combined with a higher density measurement technique (e.g. sonic logging), these are the type of variations that may be preserving a climate signal. Further, the difference in the eigenvalues e_2 and e_3 suggest a lack of rotational symmetry; this implies Taylor Dome is not a perfect dome and a combined stress state is required to model it accurately.

Additionally, Taylor Dome has a very low accumulation rate and therefore little advection, leading to a nearly linear temperature profile (Waddington and Morse, 1994). We use a linear temperature profile where the temperature, T , at the surface is the mean annual surface air temperature, -43°C , and increases to -26°C at the bedrock (Grootes and others, 1994; Morse, 1997). As the temperature never gets above -26°C , migration recrystallization activity is likely negli-

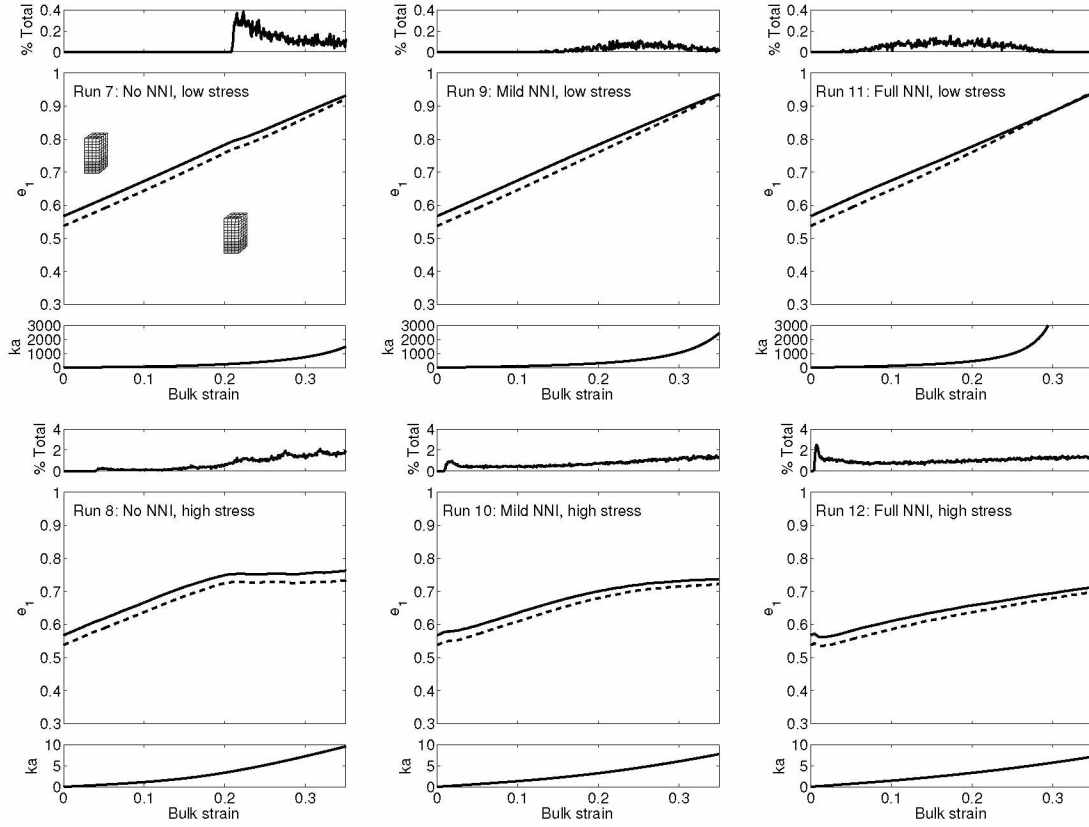


Figure 2.6: The pure-shear runs, 7-12 (Table 2.2). See Figure 2.4 caption for details.

ble here; it is well below the theoretical temperature for activation (above approximately -10°C ; Duval and Castelnau, 1995).

2.7.1 Experimental setup

We use the depth–age (Figure 2.8) and depth–temperature profiles to model an idealized ice-sheet divide with the characteristics of Taylor Dome. We calculate a depth–stress profile based on an idealized, symmetric ice divide (as described by Raymond, 1983), defined by the ice thickness and the vertical velocity of ice at the surface. We assume that these profiles are constant throughout time, so that we can use the model time to interpret a depth from the depth–age profile and then a stress and temperature from their respective profiles. From these profiles we define a stress–time profile that drives the fabric evolution.

The deviatoric stress components, σ_{ij} , of a dome-type (circularly symmetric) ice divide are

$$\boldsymbol{\sigma} = \begin{pmatrix} \frac{1}{2}\sigma & 0 & 0 \\ 0 & \frac{1}{2}\sigma & 0 \\ 0 & 0 & -\sigma \end{pmatrix}, \quad (2.31)$$

$$\sigma = 2\mathcal{A}^{-1/n} \left(2 \frac{|v_s|}{h} \right)^{1/n} \left(1 - \frac{d}{h} \right)^{1/n} \frac{v_s}{|v_s|}, \quad (2.32)$$

where \mathcal{A} is the flow parameter from Glen's flow Law (Glen, 1955), n is the exponent in Glen's flow Law, v_s is the vertical component of the ice velocity at the surface, h is the ice thickness and d is the depth. We interpret \mathcal{A} from the values given in (Paterson, 1994, p. 97) based on the ice temperature, and v_s from the top of the depth-age profile (the average accumulation rate over the century preceding 1994). Likewise, deviatoric stress components, σ_{ij} , of a ridge type ice divide are

$$\boldsymbol{\sigma} = \begin{pmatrix} \sigma & 0 & 0 \\ 0 & 0 & 0 \\ 0 & 0 & -\sigma \end{pmatrix}, \quad (2.33)$$

where σ is the same as in Eqn (2.32).

In reality, Taylor Dome is likely experiencing a higher stress than our idealized model because it assumes a flat bed. It also does not have constant depth-age, depth-temperature and depth-stress profiles. Because our model does not solve for ice flow, the assumptions in our idealized model do not account for possible strain enhancements, such as impurity-enhanced ice flow (Paterson, 1991; Faria and others, 2009), or the feedback between layers with different rheological properties, such as the feedback that can lead to concentrated shearing on layers with crystals oriented to be soft in shear (Budd and Jacka, 1989; Durand and others, 2007; Pettit and others, 2007). In general, layers that are rheologically harder in the direction of the dominant stress component will deform more slowly and the fabric will evolve more slowly if surrounded by softer layers; in our model, each layer evolves independently. Therefore, we expect our modeled fabric evolution to be slower and more uniformly distributed between layers than within Taylor Dome.

We calculated a depth-stress profile for both dome-like and ridge-like symmetry, as shown in Figure 2.10. Taylor Dome falls somewhere between these two end members, but, based on geometry, it is closer to a dome-like symmetry.

Similar to our constant-stress experiments, we modeled the evolution of a cuboid with three fabric layers of 8000 crystals. We start the model at a depth just below the pore close-off depth at 100m, and run the model to a depth 547.2m through both the ridge-like and dome-like stress

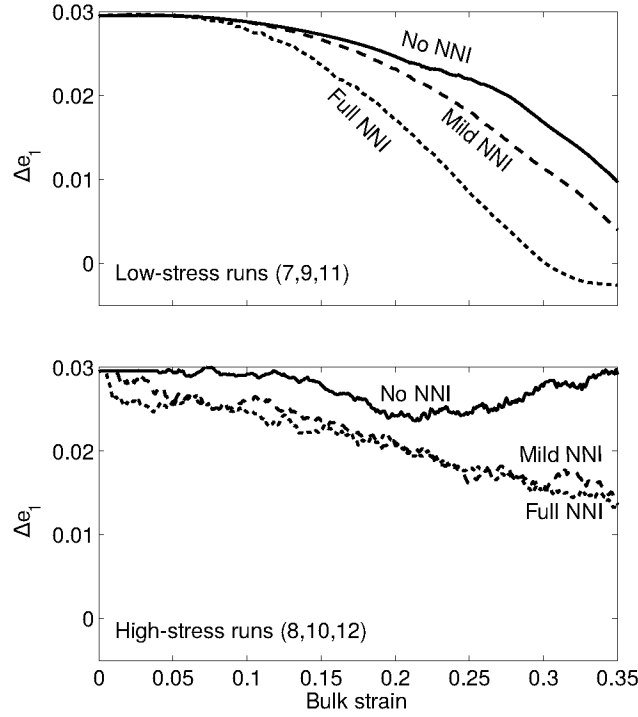


Figure 2.7: Separation of the largest eigenvalue, e_1 , between the top layer and middle layer for the pure-shear runs, 7-12. The top plot shows the low stress runs 7, 9 and 11. The bottom plot shows the high stress runs 8, 10 and 12. The solid curves indicate runs 7 and 8 with no nearest-neighbor interaction ($[\zeta, \xi] = [1, 0]$; Eqn (2.10)), the dashed curves indicate runs 9 and 10 with mild nearest-neighbor interaction ($[\zeta, \xi] = [6, 1]$) and the dotted curves indicate runs 11 and 12 with full nearest-neighbor interaction ($[\zeta, \xi] = [1, 1]$).

profiles. The time-step was 100a and the modeled depth range corresponds to 210ka of evolution. For all three layers, we use an initial uniform crystal size, D_0 , of 1.5mm, which is consistent with the average crystal size observed at 100m depth in Taylor Dome, and agrees with our the crystal-growth factor, K , (Eqn (2.1)) using an initial crystal size of 1mm (Benson, 1962). For the middle layer, we generated the initial fabric, based on a concentration parameter for the Watson distribution of $k = -2.4$ ($e_1 = 0.567$). The concentration parameter was estimated at a 100m depth from a linear interpretation of the thin sections eigenvalues ($e_1 = 0.571$, $e_2 = 0.240$, and $e_3 = 0.189$; Eqn (2.28)). Since the Watson distribution is circularly symmetric, e_2 and e_3 are set equal to a symmetric distribution with the same vertical concentration; $e_2 = e_3 = (1 - e_1)/2$. For the top and bottom layer, we generated fabrics that are slightly less concentrated; $k = -2.0$ ($e_1 = 0.538$, and $e_2 = e_3 = 0.231$). The initial fabrics are shown in Figure 2.3 (these are the same fabrics used in the constant stress experiments). This fabric is evolved for one time-step, and then used as the input

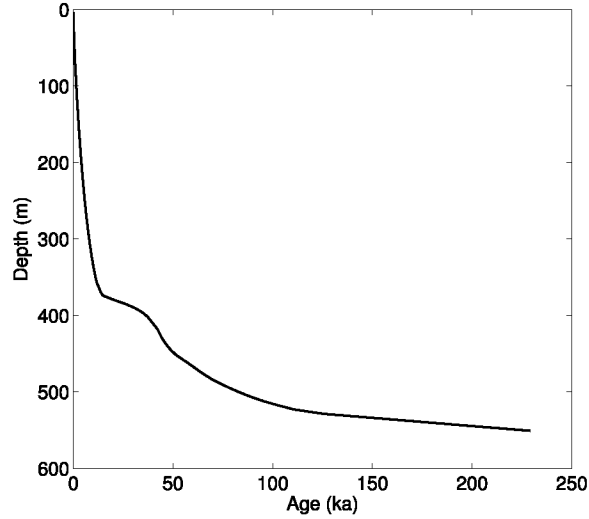


Figure 2.8: Depth-age profile for Taylor Dome, East Antarctica. (Steig and others (1998, 2000))

for the next time-step. The NNI parameters from Eqn (2.10) were varied ($[\zeta, \xi] = [1, 0], [6, 1], [1, 0]$) for different model runs (Table 2.3).

2.7.2 Results

Figure 2.11 compares the modeled evolution for the middle fabric section of the 100m fabrics for a dome-like stress profile with the measured fabric in Taylor Dome. Likewise, Figure 2.12 shows the modeled and measured fabric for a ridge-like symmetry. The modeled fabric evolves more slowly than the measured fabric in Taylor Dome because of our model assumptions: the idealized steady-state stress profile we are using and the lack of the fabric-deformation feedback. Nearest-neighbor interactions further slows down the evolution of the fabric, because they modify the crystal strain rates (Eqn (2.10)). This can be seen in the Schmidt plots of the evolved fabrics for each of these cases, which are shown in Figure 2.13. After the same total strain, the fabric with no NNI has more crystals concentrated towards vertical than the fabric with full NNI (Figure 2.14).

Figure 2.15 shows the separation between the largest eigenvalues, e_1 , of the middle and top/bottom layers in the dome-like and ridge-like stress tests (runs 13–15 and 16–18, respectively; Table 2.3) and the number of polygonization events. As in the constant-stress experiments, we see the separation of the eigenvalues decreases over time in all cases, but they remain measurable for 210ka. In both the dome-like and ridge-like cases, NNI causes the separation to decrease and

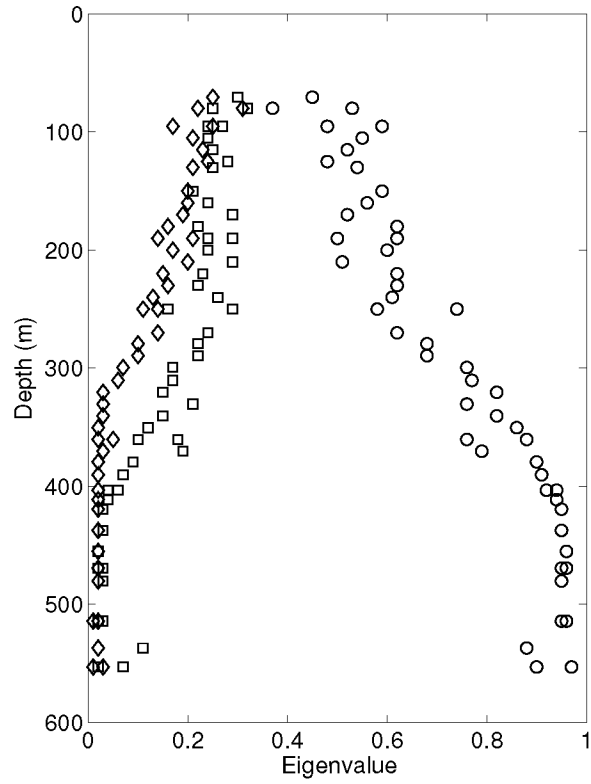


Figure 2.9: Fabric profile with depth for Taylor Dome. The fabrics were analyzed on an automatic ice fabric analyzer from thin sections of the Taylor Dome ice core. Circles correspond to eigenvalues e_1 , squares correspond to eigenvalues e_2 and diamonds correspond to eigenvalues e_3 . Measurement errors are less than ± 0.001 for the eigenvalues; the error bars are smaller than the data markers in the figure.

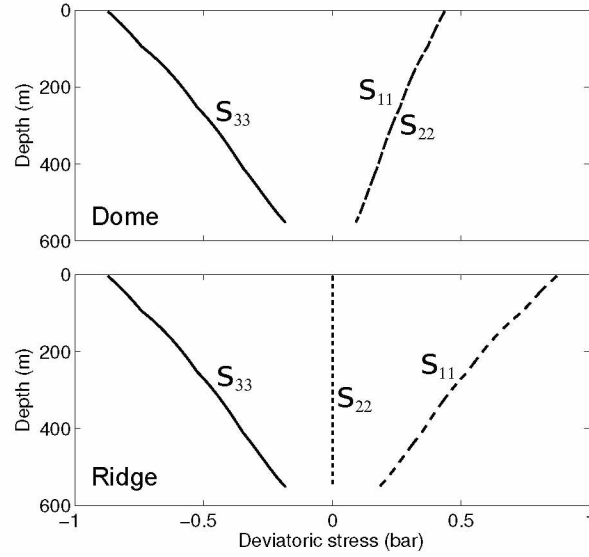


Figure 2.10: Depth-stress profile for Taylor Dome. The top plot shows a dome-like stress profile and the bottom plot shows a ridge-like profile. The solid curves correspond to σ_{33} , the dotted curves correspond to σ_{22} and the dashed curves correspond to σ_{11} .

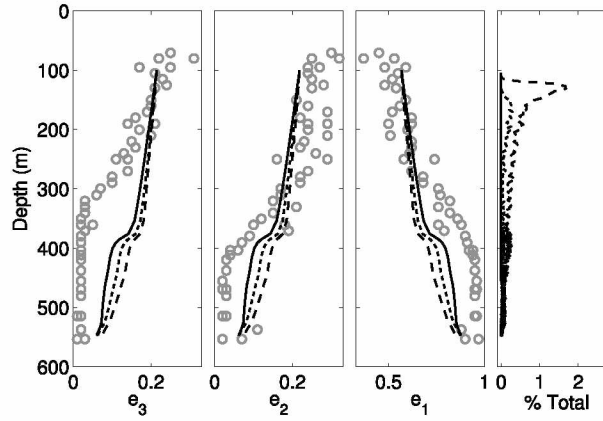


Figure 2.11: Evolution of fabric within an ice sheet based on Taylor Dome for the dome-like Taylor Runs, 13-15 (Table 2.3). The three left plots show the evolution of the three eigenvalues for the middle fabric layer in Taylor Dome and the rightmost plot shows the number of polygonization events within a time-step as a percentage of the total number of crystals. In the plots, the gray open circles are thin section measurements in Taylor Dome, the solid curve corresponds to no nearest-neighbor interaction ($[\zeta, \xi] = [1, 0]$; Eqn (2.10)), the dotted curve indicates mild nearest-neighbor interaction ($[\zeta, \xi] = [6, 1]$) and the dashed curve indicates full nearest-neighbor interaction ($[\zeta, \xi] = [1, 1]$).

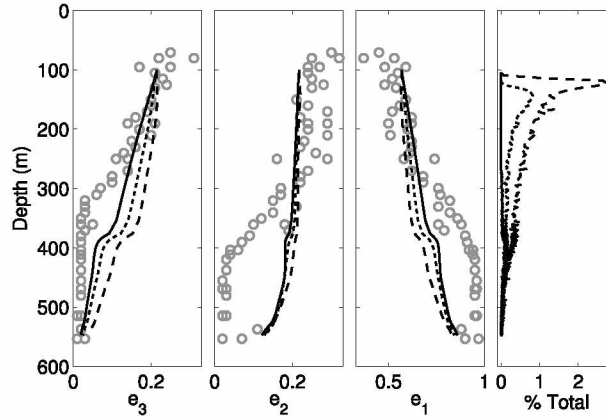


Figure 2.12: Same as Figure 2.11, but within a glacier based on Taylor Dome for the ridge-like Taylor runs, 16-18 (Table 2.3).

polygonization starts at lower bulk strains than in the no NNI runs. In the ridge-like runs (16–18) the fabric is adjusting from the circularly symmetric distribution to an elliptical distribution expected from pure shear (Paterson, 1994). This causes some crystals to have a very high strain rate, causing polygonization to be much more dominate than in the dome-like runs (13–15).

2.8 Discussion

In all of our experiments, a variation in fabric, such as that created by a fluctuation in climate, is preserved until the fabric equilibrates to the stress state. For uniaxial compression and pure shear, there is a ‘window of opportunity,’ in which the separation of eigenvalues is sufficient to preserve the climate signal because the weaker fabric takes more time to equilibrate. The minimum separation required to measure a fabric anomaly depends on the measurements technique.

For a constant applied stress, the length of time this window is open depends on the magnitude of the initial fabric variation, the initial strength of the weaker fabric, the magnitude of the applied stress (which controls the strain rate and, therefore, the rate of polygonization) and the strength of the nearest-neighbor interactions. If the fabric variation is small to begin with, it may become

Table 2.3: Summary of the run setup of the Taylor Dome experiments.

Run	Dome	Run	Ridge
	NNI [ζ, ξ]		NNI [ζ, ξ]
13	None [1, 0]	16	None [1, 0]
14	Mild [6, 1]	17	Mild [6, 1]
15	Full [1, 1]	18	Full [1, 1]

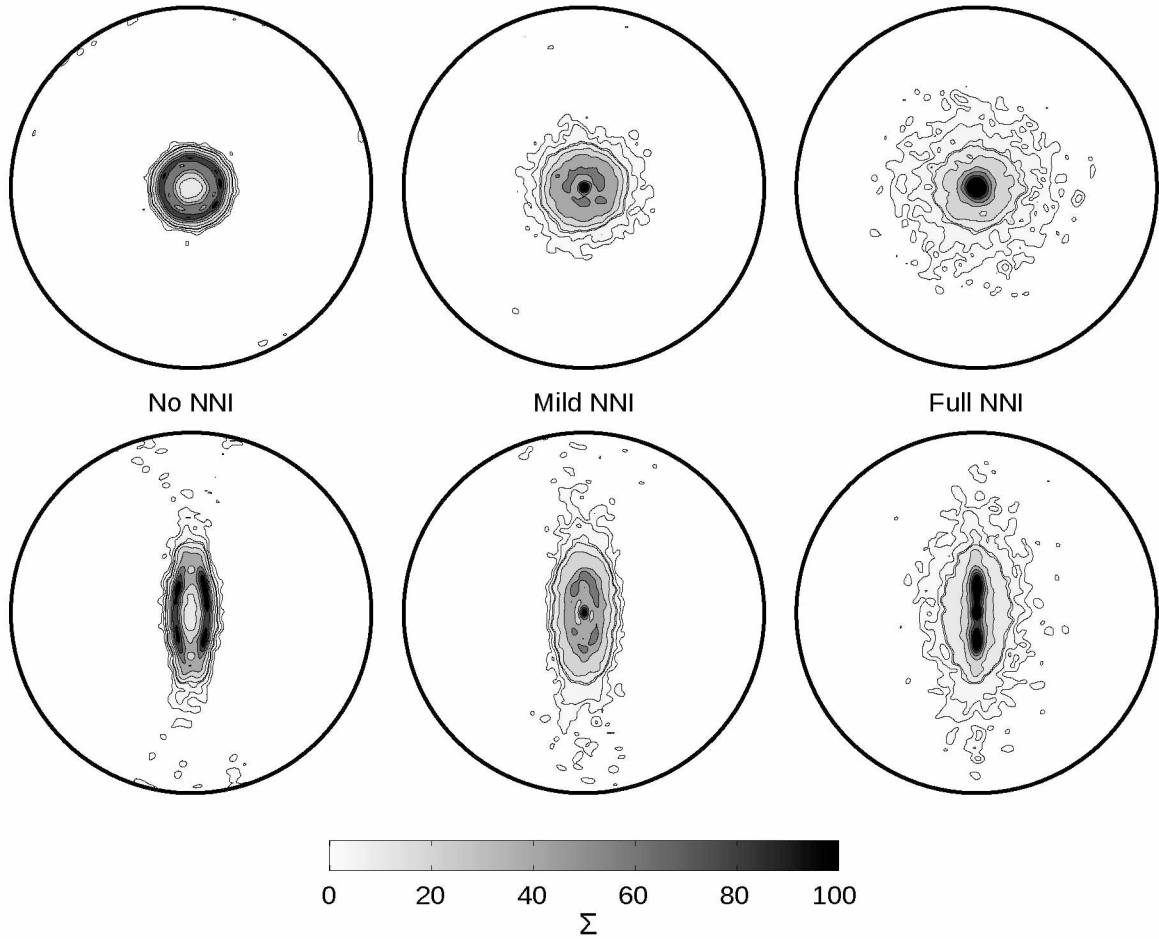


Figure 2.13: Contoured Schmidt plots of the evolved middle layer fabric after 210 000 years for dome-like (top row) and ridge-like (bottom row) symmetry. The left column shows no nearest-neighbor interaction ($[\zeta, \xi] = [1, 0]$; Eqn (2.10)), the middle column shows mild nearest-neighbor interaction ($[\zeta, \xi] = [6, 1]$), and the right column shows full nearest-neighbor interaction ($[\zeta, \xi] = [1, 1]$). The plots are contoured in the same way as in Figure 2.3, but the fabrics are now contoured at levels of $0, 20\Sigma, \dots, 100\Sigma$.

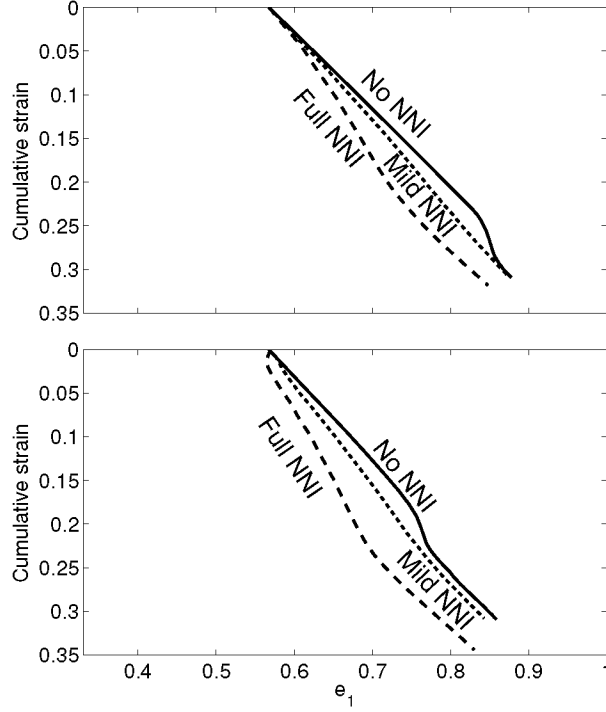


Figure 2.14: Cumulative strain in the Taylor Dome runs. The top plot shows the cumulative strain undergone by the modeled fabrics as a function of the largest eigenvalue, e_1 , for the dome-like Taylor runs, 13-15 (Table 2.3). Likewise, the bottom plots show the ridge-like Taylor runs, 16-18. In the plots, the solid curves corresponds to no nearest-neighbor interaction ($[\zeta, \xi] = [1, 0]$; Eqn (2.10)), the dotted lines indicates mild nearest-neighbor interaction ($[\zeta, \xi] = [6, 1]$) and the dashed lines indicates full nearest-neighbor interaction ($[\zeta, \xi] = [1, 1]$).

immeasurable before either fabric reaches equilibrium. If the fabric variation is sufficiently large, the weaker initial fabric controls the time the window is open because the window closes as this weaker fabric reaches equilibrium with the local stress state (the stronger fabric reaches equilibrium before the weaker fabric). Higher stress leads to higher strain rates and faster rotation of the crystals. Therefore, the fabric will equilibrate and the window will close more quickly in time.

Polygonization plays a major role in the evolution of fabric. Each additional polygonization event rotates a crystal away from the principal stress direction, therefore acting to slow down the strengthening of the fabric. Polygonization events, however, do not occur uniformly in time because each event requires a threshold dislocation density. At high strain rates (resulting from high stress in our experiments), polygonization events occur often throughout the deformation process. But at the low strain rates we studied, our model predicts a negligible number of polygoniza-

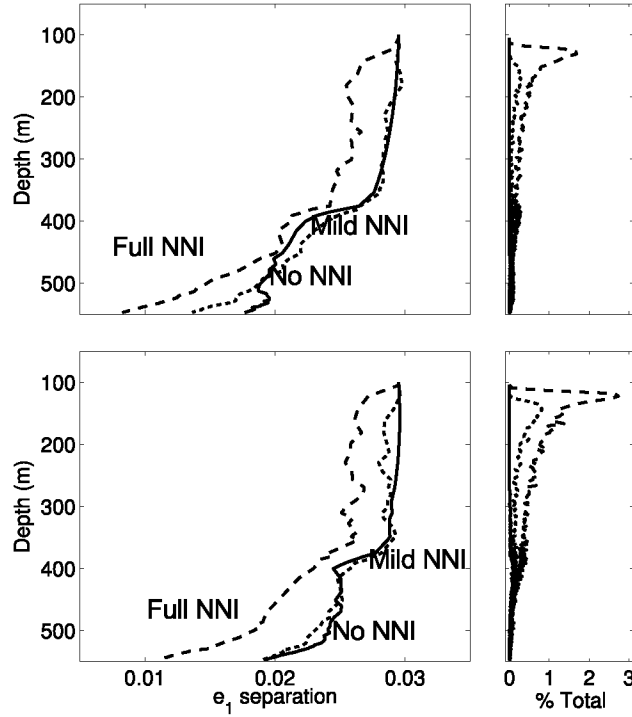


Figure 2.15: Largest eigenvalue separation for Taylor Dome. The top plots show the separation of the largest eigenvalue, e_1 , between the top and middle fabric layers for the dome-like Taylor runs, 13-15 (Table 2.3), as well as the total number of polygonization events within a time-step, as a percentage of the total number of crystals. Likewise, the bottom plots show the ridge-like Taylor runs, 16-18. In the plots, the solid curves correspond to no nearest-neighbor interaction ($[\zeta, \xi] = [1, 0]$; Eqn (2.10)), the dotted curves indicates mild nearest-neighbor interaction ($[\zeta, \xi] = [6, 1]$) and the dashed curves indicates full nearest-neighbor interaction ($[\zeta, \xi] = [1, 1]$).

tion events until 0.20 or 0.30 strain. When neighboring crystals interact, however, polygonization events occur earlier in the deformation process.

Nearest-neighbor interactions minimize the differences in strain rates among neighboring crystals. With NNI, a poorly oriented or hard crystal surrounded by soft crystals will deform faster than without NNI, advancing when the crystal will polygonize. Likewise, a soft crystal surrounded by hard crystals will deform more slowly, delaying when the crystal polygonizes. However, because this crystal is deforming less, it will stay in a softer orientation longer, while the neighboring hard crystals will also move to a softer orientation through polygonizations (their deformation is being increased by the softer crystal). The net effect of this is to increase the overall strain rate of the ice, advance the timing of polygonizations and increasing the overall number of polygonization events. Since NNI causes the crystals to bunch up (the hardest crystals get softer

and the softest crystals get harder), the window will close more quickly; the separation between the fabrics will be reduced.

By finding the time (and therefore strain) at which the eigenvalues separation is less than 0.01, we can determine how long the window stays open. Our model results suggest that at low stresses, similar to those found at thick cold ice divides, the window stays open for ≈ 2000 ka. At higher stresses, similar to those found at smaller ice sheets and ice caps, the window stays open for ≈ 10 ka.

When we apply this model to Taylor Dome, we see that the low stresses and cold temperatures result in maintaining the separation of eigenvalues throughout the depth of the ice sheet. This suggests that a fabric anomaly created by a fluctuation in climate may be measurable deep in the ice: *the window stays open*. The window stays open even with full NNI implemented. It is important to note that our fabric only evolves to ≈ 0.3 strain throughout our Taylor Dome profile since the idealized stress profile was generated with an isotropic ice assumption and our fabric experiences stress hardening as it evolves. Realistically, the fabric would evolve to ≈ 1.0 strain if the fabric–deformation feedback was included. This may cause the fabric signal to be lost higher up in ice sheet, however, the fabric–deformation feedback may also cause an initial enhancement of the climate signal by causing the stronger fabric to evolve much faster than the weaker fabric. Integrating this model into a flow model would allow this feedback to be studied.

2.9 Conclusions

Our model for fabric evolution in ice suggests that for compressive-stress regimes, total strains of at least 0.30 are necessary to rid fabric of its ‘memory’ of past fabric and stress states. Near an ice divide, most ice does not reach 0.30 total strain until deep in the ice (deeper for cold or low stress divides, and shallower for warm or high stress divides). Therefore, we can preserve a fabric anomaly, such as may be induced in the firn by a fluctuation in climate, throughout most of the depth of the ice sheet.

The rate of fabric evolution depends on strain rate, and our model assumes the strain rate is related to stress, based on the analytic flow law developed by Thorsteinsson (2001, 2002), which is an extension of Glen’s flow law and uses the typical softness parameters as reviewed by (Paterson, 1994, p. 97). As discussed in Paterson, many ways have been suggested to alter the isotropic softness parameter. If we increase the value of the softness parameter in our model, then the same stress will result in higher strain rates. While higher strain rates will rotate the crystals more quickly and increase the rate of fabric evolution, higher strain rates also induce polygonization

events, which slows bulk fabric evolution and preserves the fabric anomaly for longer. The net effect of softer ice depends on the balance of these two processes.

If different layers have different isotropic rheologies (e.g. due to differences in impurities), then the complex feedbacks between stress and strain-rates may cause the softer ice to have a higher strain rate. This high strain rate will lead to faster fabric evolution unless it triggers polygonization events, which slows down fabric evolution. The fabric evolution will be determined by the balance of these two processes. Furthermore, impurities tend to impede crystal growth, which increases the likelihood of a polygonization event (as Eqn (2.3) shows, the rate of polygonization is inversely proportional to crystal size).

Differences in rheologies between layers may also be generated by the fabric itself, because, in compression, crystals tend to rotate to a ‘hard’ orientation. The stronger the fabric, the harder the ice in compression. In our model results, this is what causes the decrease in strain rate as the fabric strengthens, slowing the rate of fabric evolution.

Finally, our model assumes cold ice (-30°C) where migration recrystallization is likely negligible. At higher temperatures, when migration recrystallization is known to be active, new, strain-free crystals grow quickly, polygonization events decrease and fabric weakens because the new crystals grow in a ‘soft’ orientation. The effects of migration recrystallization on fabric evolution or the ability to preserve a fabric anomaly is not fully understood. Data from the EPICA Dome C borehole suggests that fabric variability maintains its correlation with climate variability despite active migration recrystallization (Gusmeroli and others, 2012). Kipfstuhl and others (2009) have shown that migration recrystallization may be active at much lower temperatures and strain rates.

Because a real ice divide is rarely in steady state, often migrating its position laterally, ice rarely only experiences a pure compressive stress state (uniaxial or pure shear). Along its particle path, an ice particle will experience a combination of compressive and simple-shear regimes that varies throughout the depth. Our results suggest what is possible for pure compressive regimes. When simple shear is included, the results may be significantly different. Our goal in this paper was to isolate the compressive regimes and further work is required to detail the effect of simple shear on a fabric variation.

We can, however, speculate on the response to simple shear of a fabric variation, similar to the one we studied here, because many of the same principles apply. The primary difference between compressive and simple-shear states of stress is that fabric in simple shear tends to rotate into a ‘soft’ orientation, with respect to the applied stress, rather than into a ‘hard’ orientation, as happens with compressive regimes. This difference results in ice with strong fabrics having higher

strain rates than ice with weaker fabrics under the same applied stress. Because fabric evolution depends on strain rate, the stronger fabric will evolve fabric more quickly than the weaker fabric. Rather than simply slowing the decrease in separation (slowly closing the window), there will be a *positive feedback* that opens the window wider. This effect is observable in the deepest ice in ice sheets, where shear stress is typically highest; this deep ice exhibits the strongest variations in fabric (Gusmeroli and others, 2012).

It is likely that fabric can be developed as a climate proxy, because a climate-induced variation in fabric can be preserved throughout the depth of an ice sheet. Through the use of geophysical inverse methods, it may be possible to use a fabric-evolution model to invert continuous fabric data (e.g. a sonic velocity profile) for past temperatures. However, there is still much research needed in order for the fabric proxy to be realized. A fabric-evolution model that includes dynamic recrystallization will need to be coupled to an ice-flow model, and the response of fabric variations across a wide variety of stress states will have to be quantified. Furthermore, the parameterizations used to model the dynamic recrystallization processes need to be robust, and new parameterizations may need to be developed, especially in the case of migration recrystallization (Kipfstuhl and others, 2009).

2.10 Acknowledgements

We thank Larry Wilen for allowing us to use the Taylor Dome data. We thank Ed Waddington, Regina Carns, Alessio Gusmeroli, Maurine Montagnat, Cathrine Ritz and Paul Duval for enlightening discussions on fabric evolution. We thank Paul Jacobson for the many modeling tips he provided, and Ed Bueler for his insightful discussions on statistics. Finally, we thank Scientific Editor Jo Jacka and the two anonymous reviewers for their comments which considerably improved the manuscript. The work presented in this paper was supported by the US National Science Foundation (NSF) grants OPP#0948247, OPP#0940650, OPP#0636795 and an NSF GK-12 Fellowship to Joseph H. Kennedy.

2.11 References

- Alley, R.B., 1992. Flow-law hypotheses for ice-sheet modeling, *J. Glaciol.*, **38**(129), 245–256.
- Alley, R.B., J.H. Perepezko and C.R. Bentley, 1986. Grain growth in polar ice: I. theory, *J. Glaciol.*, **32**(112), 415–424.

- Arnaud, L., J. Weiss, M. Gay and P. Duval, 2000. Shallow-ice microstructure at Dome Concordia, Antarctica, *Ann. Glaciol.*, **30**, 8–12.
- Azuma, N., 1994. A flow law for anisotropic ice and its application to ice sheets, *Earth and Planetary Science Letters*, **128**(3-4), 601–614.
- Azuma, N. and A. Higashi, 1985. Formation processes of ice fabric pattern in ice sheets, *Ann. Glaciol.*, **6**, 130–134.
- Benson, C.S., 1962. Stratigraphic studies in the snow and firn of the Greenland ice sheet, *Tech. rep.*, Snow, Ice and Permafrost Research Establishment, US Army Corps of Engineers.
- Budd, W.F. and T.H. Jacka, 1989. A review of ice rheology for ice sheet modelling, *Cold Reg. Sci. Technol.*, **16**(2), 104–144.
- Carns, R., E.D. Waddington, E.C. Pettit and S.G. Warren, 2010. A model of grain growth and crystal fabric in polar snow and firn, *AGU Fall Meeting Abstracts*, D572.
- Castelnau, O. and P. Duval, 1994. Simulations of anisotropy and fabric development in polar ices, *Ann. Glaciol.*, **20**, 277–282.
- Castelnau, O., P. Duval, R.A. Lebensohn and G.R. Canova, 1996. Viscoplastic modeling of texture development in polycrystalline ice with a self-consistent approach: comparison with bound estimates, *J. Geophys. Res.*, **101**(B6), 13851–13868.
- Colbeck, S.C., 1983. Theory of metamorphism of dry snow, *J. Geophys. Res.*, **88**(C9), 5475–5482.
- Cook, P.A., D.C. Alexander and G.J.M. Parker, 2004. Modelling noise-induced fibre-orientation error in diffusion-tensor MRI, IEEE International Symposium on Biomedical Imaging: Nano to Macro, IEEE, 332–335.
- De La Chapelle, S., O. Castelnau, V. Lipenkov and P. Duval, 1998. Dynamic recrystallization and texture development in ice as revealed by the study of deep ice cores in Antarctica and Greenland, *J. Geophys. Res.*, **103**(B3), 5091–5105.
- Di Prinzio, C.L., L.A. Wilen, R.B. Alley, J.J. Fitzpatrick, M.K. Spencer and A.J. Gow, 2005. Fabric and texture at Siple Dome, Antarctica, *J. Glaciol.*, **51**(173), 281–290.
- Durand, G., F. Gillet-Chaulet, A. Svensson, O. Gagliardini, S. Kipfstuhl, J. Meyssonier, F. Parrenin, P. Duval and D. Dahl-Jensen, 2007. Change in ice rheology during climate variations –

- implications for ice flow modelling and dating of the EPICA Dome C core, *Climate of the Past*, **3**(1), 155–167.
- Duval, P., M.F. Ashby and I. Anderman, 1983. Rate-controlling processes in the creep of polycrystalline ice, *Journal of Physical Chemistry*, **87**(21), 4066–4074.
- Duval, P. and O. Castelnau, 1995. Dynamic recrystallization of ice in polar ice sheets, *Journal de Physique IV*, 197–205.
- Faria, S.H., J. Freitag and S. Kipfstuhl, 2010. Polar ice structure and the integrity of ice-core paleoclimate records, *Quaternary Science Reviews*, **29**(1-2), 338–351.
- Faria, S.H., S. Kipfstuhl, N. Azuma, J. Freitag, I. Weikusat, M.M. Murshed and W.F. Kuhs, 2009. The multiscale structure of Antarctica part I: inland ice, *Low Temperature Science*, **68**(Sup.), 39–59.
- Fisher, N.I., T. Lewis and B.J.J. Embleton, 1987. Statistical analysis of spherical data, Cambridge University Press.
- Fisher, R., 1953. Dispersion on a Sphere, *Proceedings of the Royal Society. Series A, Mathematical and Physical Sciences*, **217**(1130), 295–305.
- Fujita, S., H. Enomoto, K. Fukui, Y. Iizuka, H. Motoyama, F. Nakazawa, S. Sugiyama and S. Surdyk, 2012. Formation and metamorphism of stratified firn at sites located under spatial variations of accumulation rate and wind speed on the East Antarctic ice divide near Dome Fuji, *The Cryosphere Discussions*, **6**(2), 1205–1267.
- Fujita, S., J. Okuyama, A. Hori and T. Hondoh, 2009. Metamorphism of stratified firn at Dome Fuji, Antarctica: a mechanism for local insolation modulation of gas transport conditions during bubble close off, *J. Geophys. Res.*, **114**(F03023), 1–21.
- Gagliardini, O., G. Durand and Y. Wang, 2004. Grain area as a statistical weight for polycrystal constituents, *J. Glaciol.*, **50**(168), 87–95.
- Gagliardini, O., F. Gillet-Chaulet and M. Montagnat, 2009. A review of anisotropic polar ice models: from crystal to ice-sheet flow models, *Low Temperature Science*, **68**(Supplemental), 149–166.
- Gillet-Chaulet, F., O. Gagliardini, J. Meyssonier, M. Montagnat and O. Castelnau, 2005. A user-friendly anisotropic flow law for ice-sheet modelling, *J. Glaciol.*, **51**(172), 3–14.

- Gillet-Chaulet, F., O. Gagliardini, J. Meyssonier, T. Zwinger and J. Ruokolainen, 2006. Flow-induced anisotropy in polar ice and related ice-sheet flow modelling, *J. Non Newtonian Fluid Mech.*, **134**, 33–43.
- Glen, J.W., 1955. The creep of polycrystalline ice, *Proceedings of the Royal Society of London. Series A, Mathematical and Physical Sciences*, **228**(1175), 519–538.
- Gördert, G., 2003. A mesoscopic approach for modelling texture evolution of polar ice including recrystallization phenomena, *Ann. Glaciol.*, **37**(1), 23–28.
- Gow, A.J. and D. Meese, 2007. Physical properties, crystalline textures and c-axis fabrics of the Siple Dome (Antarctica) ice core, *J. Glaciol.*, **53**(183), 573–584.
- Grootes, P.M., E.J. Steig and M.Stuiver, 1994. Taylor Ice Dome Study 1993-1994: an ice core to bedrock, *Antarctic Journal of the United States*, **29**, 79–81.
- Gusmeroli, A., E.C. Pettit, J.H. Kennedy and C. Ritz, 2012. The crystalline fabric of glacial ice from full-waveform borehole sonic logging, *J. Geophys. Res.*, **117**(F03021), 1–13.
- Hansen, D.P. and L.A. Wilen, 2002. Performance and applications of an automated c-axis ice-fabric analyzer, *J. Glaciol.*, **48**(160), 159–170.
- Hooke, R.L., 2005. Principles of glacier mechanics, Cambridge University Press.
- Kamb, W.B., 1959. Ice petrofabric observation from Blue Glacier, Washington, in relation to theory and experiment, *J. Geophys. Res.*, **64**(11), 1891–1909.
- Ketcham, W.M. and P.V. Hobbs, 1969. An experimental determination of the surface energies of ice, *Philosophical Magazine*, **19**(162), 1161–1173.
- Kipfstuhl, S., S.H. Faria, N. Azuma, J.Freitag, I. Hamann, P. Kaufmann, H. Miller, K. Weiler and F. Wilhelms, 2009. Evidence of dynamic recrystallization in polar firn, *J. Geophys. Res.*, **114**(B5), 1–10.
- Kobayashi, T., 1967. On the variation of ice crystal habit with temperature, *Physics of Snow and Ice*, 95–104.
- Lebensohn, R.A., Y. Liu and P. Ponte Casta neda, 2004. On the accuracy of the self-consistent approximation for polycrystals: comparison with full-field numerical simulations, *Acta Materialia*, **52**(18), 5347–5361.

- Li, K. and C.K. Wong, 1993. Random sampling from the watson distribution, *Communications in Statistics – Simulation and Computation*, **22**(4), 997–1009.
- Lliboutry, L., 1993. Anisotropic, transversely isotropic nonlinear viscosity of rock ice and rheological parameters inferred from homogenization, *International Journal of Plasticity*, **9**, 619–632.
- Mardia, K.V. and P.E. Jupp, 2000. Directional Statistics, Wiley.
- Meyssonnier, J. and A. Philip, 2000. Comparison of finite-element and homogenization methods for modelling the viscoplastic behaviour of a S2-columnar-ice polycrystal, *Ann. Glaciol.*, **30**(1), 115–120.
- Miguel, M.-C., A. Vespignani, S. Zapperi, J. Weiss and J.-R. Grasso, 2001. Intermittent dislocation flow in viscoplastic deformation, *Nature*, **410**(6829), 667–671.
- Mohamed, G. and B. Bacroix, 2000. Role of stored energy in static recrystallization of cold rolled copper single and multicrystals, *Acta Materialia*, **48**(13), 3295–3302.
- Montagnat, M. and P. Duval, 2000. Rate controlling processes in the creep of polar ice, influence of grain boundary migration associated with recrystallization, *Earth and Planetary Science Letters*, **183**, 179–186.
- Morland, L.W., 2002. Influence of lattice distortion on fabric evolution in polar ice, *Continuum Mechanics and Thermodynamics*, **14**(1), 9–24.
- Morse, D.L., 1997. Glacier geophysics at Taylor Dome, Antarctica, Ph.d., University of Washington.
- Nelson, J. and C. Knight, 1998. Snow crystal habit changes explained by layer nucleation, *J. Atmos. Sci.*, **55**(8), 1452–1465.
- Palmer, T.J. and A.H. Fagg, 2009. Learning grasp affordances with variable centroid offsets, IEEE/RSJ International Conference on Intelligent robots and systems, IEEE, 1265–1271.
- Paterson, W.S.B., 1991. Why ice-age ice is sometimes ‘soft’, *Cold Regions Science and Technology*, **20**, 75–98.
- Paterson, W.S.B., 1994. The physics of glaciers, Butterworth-Heinemann, third ed.
- Pettit, E.C., T. Thorsteinsson, P.H. Jacobson and E.D. Waddington, 2007. The role of crystal fabric in flow near an ice divide, *J. Glaciol.*, **53**(181), 277–288.

- Pettit, E.C. and E.D. Waddington, 2003. Ice flow at low deviatoric stress, *J. Glaciol.*, **49**(166), 359–369.
- Pettit, E.C., E.D. Waddington, T. Thorsteinsson, A. Gusmeroli, J.H. Kennedy, C. Ritz and R. Carns, 2011. Using borehole sonic logging to infer ice microstructure and climate history, *Geophysical Research Abstracts*, **13**.
- Placidi, L., R. Greve, H. Seddik and S.H. Faria, 2009. Continuum-mechanical, anisotropic flow model for polar ice masses, based on an anisotropic flow enhancement factor, *Continuum Mechanics and Thermodynamics*, **22**(3), 221–237.
- Raymond, C.F., 1983. Deformation in the vicinity of ice divides, *J. Glaciol.*, **29**(103), 357–373.
- Sarma, G.B. and P.R. Dawson, 1996. Effects of interactions among crystals on the inhomogeneous deformations of polycrystals, *Acta Metallurgica*, **44**(5), 1937–1953.
- Shimizu, I., 1998. Stress and temperature dependence of recrystallized grain size: a subgrain misorientation model, *Geophys. Res. Lett.*, **25**(22), 4237–4240.
- Steig, E.J., E.J. Brook, J.W.C. White, C.M. Sucher, M.L. Bender, S.J. Lehman, D.L. Morse, E.D. Waddington and G.D. Clow, 1998. Synchronous climate changes in Antarctica and the North Atlantic, *Science*, **282**, 92–95.
- Steig, E.J., D.L. Morse, E.D. Waddington, M. Stuiver, P.M. Grootes, P.A. Mayewski, M.S. Twickler and S.I. Whitlow, 2000. Wisconsinan and Holocene climate history from an ice core at Taylor Dome, western Ross Embayment, Antarctica, *Geografiska Annaler. Series A, Physical Geography*, **82**(2), 213–235.
- Svensson, A., S.W. Neilsen, S. Kipfstuhl, S.J. Johnsen, J.P. Steffensen, M. Bigler, U. Ruth and R. Röthlisberger, 2005. Visual stratigraphy of the North Greenland Ice Core Project (NorthGRIP) ice core during the last glacial period, *J. Geophys. Res.*, **110**(D2), D02108.
- Thorsteinsson, T., 2001. An analytical approach to deformation of anisotropic ice-crystal aggregates, *J. Glaciol.*, **47**(158), 507–516.
- Thorsteinsson, T., 2002. Fabric development with nearest-neighbor interaction and dynamic recrystallization, *J. Geophys. Res.*, **107**(B1,2014), 1–13.

- Thorsteinsson, T., E.D. Waddington, K.C. Taylor, R.B. Alley and D.D. Blankenship, 1999. Strain rate enhancement at Dye 3, Greenland, *J. Glaciol.*, **45**(150), 338–345.
- Ulrich, G., 1984. Computer generation of distributions on the m-sphere, *Journal of the Royal Statistical Society: Series C (Applied Statistics)*, **33**(2), 158–163.
- Van der Veen, C.J. and I.M. Whillians, 1994. Development of fabric in ice, *Cold Regions Science and Technology*, **22**(2), 171–195.
- Waddington, E.D. and D.L. Morse, 1994. Spatial variations of local climate at Taylor Dome, Antarctica: implications for paleoclimate from ice cores, *Ann. Glaciol.*, **20**(1), 219–225.
- Watson, G.S., 1965. Equatorial distributions on a sphere, *Biometrika*, **52**(1-2), 193–201.
- Watson, G.S., 1982. Distributions on the circle and sphere, *Journal of Applied Probability*, **19**, 265–280.
- Weerman, J., 1973. Creep of ice, *Physics and Chemistry of Ice*, 320–337.
- Wilén, L.A., 2000. A new technique for ice-fabric analysis, *J. Glaciol.*, **46**(152), 129–139.
- Wilén, L.A., C.L. Di Prinzio, R.B. Alley and N. Azuma, 2003. Development, principles, and applications of automated ice fabric analyzers, *Microscopy Research and Technique*, **62**(1), 2–18.
- Wood, A.T.A., 1994. Simulation of the von Mises Fisher distribution, *Communications in Statistics: Simulation and Computation*, **23**(1), 157–164.
- Woodcock, N.H., 1977. Specification of fabric shapes using an eigenvalue method, *Geological Society Of America Bulletin*, **88**, 1231–1236.

Chapter 3

The response of fabric variations to simple shear and migration recrystallization ¹

3.1 Abstract

The observable microstructures in ice are the result of many dynamic and competing processes. These processes are influenced by climate variables in the firn. Layers deposited in different climate regimes may show variations in fabric which can persist deep into the ice sheet; fabric may ‘remember’ these past climate regimes. We model the evolution of fabric variations below the firn-ice transition and show that the addition of shear to compressive-stress regimes preserves the modeled fabric variations longer than compression-only regimes because shear drives a positive feedback between crystal rotation and deformation. Even without shear, the modeled ice retains memory of the fabric variation for ~ 200 ka in typical polar ice-sheet conditions. Our model shows that temperature affects how long the fabric variation is preserved, but only affects the strain-integrated fabric evolution profile when comparing results straddling the thermal-activation-energy threshold ($\sim -10^\circ\text{C}$). Even at high temperatures, migration recrystallization does not eliminate the modeled fabric’s memory under most conditions. High levels of nearest-neighbor interactions will, however, eliminate the modeled fabric’s memory more quickly than low levels of nearest-neighbor interactions. Ultimately, our model predicts that fabrics will retain memory of past climatic variations when subject to a wide variety of conditions found in polar ice sheets.

3.2 Introduction

Observations show that the microstructure of ice records aspects of climate history (e.g., Paterson, 1991; Gow and others, 1997; Durand and others, 2007; Pettit and others, 2011). However, understanding if and how the climate ‘memory’ is preserved and evolved through time is challenging (Kennedy and others, 2013). Paterson (1991) showed that ice-age ice typically consists of smaller grains and stronger fabric (statistically preferred orientation of the ice crystal lattice) than Holocene ice, providing the first hint of a connection between paleoclimate and microstructure in an ice sheet. More recently, both thin-section data and sonic-velocity data from Dome C, East Antarctica, show an abrupt transition in the ice rheology at 1750 m depth, which corresponds to a transition between the warm MIS-5 (marine isotope stage 5) and the cool MIS-6 ~ 150 ka ago (Durand and others, 2007; Gusmeroli and others, 2012). Many microstructural features (e.g. dust

¹Published as Kennedy, J. H. and Pettit, E. C. (2015). The response of fabric variations to simple shear and migration recrystallization. *Journal of Glaciology*, **61**(227), 537-550. doi:10.3189/2015JoG14J156

particles, grain size, fabric) correlate with climate history (e.g., Durand and others, 2006b). This correlation is caused by a number of interdependent microstructural processes (e.g., Alley, 1992; Faria and others, 2014b).

Classically, three main processes account for the observed grain and fabric structure throughout the depth of the ice sheet (e.g., Alley and others, 1986; Alley, 1992; De La Chapelle and others, 1998; Cuffey and Paterson, 2010). Normal grain growth is the temperature-controlled coarsening of grains through grain-boundary migration in order to reduce the total grain-boundary energy stored in the ice. Large grains consume small grains in such a way that the average grain cross-sectional area increases linearly with time (Alley and others, 1986). This process is considered to be active throughout the depth of the ice sheet, but is counter-balanced by polygonization at intermediate depths of the ice sheet, where a steady grain-size profile is observed (Alley, 1992). Strain energy builds in a grain during deformation, and bending or twisting stresses cause dislocations to form a ‘wall’, which eventually divides (polygonizes) the grain and causes a small mis-orientation between the grains’ crystal lattices. At the greatest depths of an ice sheet, where the temperature is $> -10^{\circ}\text{C}$, migration recrystallization becomes active. Here temperatures are great enough for grain boundaries to move easily, driven by differences in stored strain energy (Alley, 1992). With high enough stored strain energy, it becomes energetically favorable to nucleate a new strain-free grain, which rapidly migrates through neighboring grains and has an orientation that is dependent on the applied stress (Duval and Castelnau, 1995). With sufficiently high rates of migration recrystallization, an inverse power-law relationship between grain size and stress forms (Jacka and Jun, 1994) and an entirely new fabric structure results. Because fabric and grain structure are a result of recrystallization processes, conventional wisdom is that fabric will not maintain any past climate information.

Although the classic three-process model, or ‘tripartite paradigm,’ has successfully described the average grain size and fabric in ice cores, observations in the last decade have led to new perspectives on these processes (e.g., Faria and others, 2014a,b, cf. De La Chapelle and others 1998). Techniques that allow observations on the scale of micrometers or smaller (e.g., Kipfstuhl and others, 2006; Obbard and others, 2006; Faria and others, 2011) are now common, whereas classical observations typically were on the scale of millimeters or larger (Faria and others, 2014a). Some observations from these high-resolution techniques cannot be accounted for under the tripartite paradigm if it is considered a description of the actual microstructural physics. For example, in Dronning Maud Land, Antarctica, the firn grain boundary structure appears to have been dominated by migration recrystallization during the firn-ice transition, even though it is much colder

(annual mean temperature -46°C) than where migration recrystallization is considered to be a dominant process ($\gtrsim 10^{\circ}\text{C}$; Kipfstuhl and others, 2009). However, due to its success in describing the microstructure observed in ice (summarized by Faria and others, 2014a,b), the tripartite paradigm provides a robust phenomenological model of the average grain size and especially the fabric evolution (as discussed in the next section), despite its imperfections.

Observations of more recrystallization in the firn and ice of an ice sheet than expected under the tripartite paradigm (e.g., Kipfstuhl and others, 2009) would seem to reinforce the conventional idea that fabric cannot preserve a memory of past climate. Indeed, the memory is unlikely to be stored directly in the grain structure or fabric strength of a particular layer of ice, as they are continually evolving. The relative differences in the fabric between layers, however, can be preserved under certain conditions (Kennedy and others, 2013).

Because the microstructural processes active in the firn are sensitive to climatic variables (Alley and others, 1990), layers of firn experiencing different climate regimes may have observable variations in the fabric which can be preserved. For example, in polar regions, vapor deposition is the primary method of grain growth in the upper firn and it is anisotropic: deposition will favor either the basal or prism faces of the ice-crystalline lattice, depending on the temperature (Nelson and Knight, 1998). This process causes grains with the preferred face parallel to the vapor pressure gradient to grow more than grains in a less favorable orientation. Because these grains grow at the expense of other grains (Colbeck, 1983), the well-oriented grains are more likely to remain (Carns and others, 2010, are developing a model to explore this process). Variations in texture and fabric in the firn may reflect variations in temperature and vapor-pressure gradients (Adams and Miller, 2003). While measuring fabric in firn is difficult, several studies have reported non-isotropic fabric measurements from firn (Di Prinzio and others, 2005; Fujita and others, 2009; Montagnat and others, 2012). Montagnat and others (2012) found that using non-isotropic initial fabrics was required during simulations of the fabric evolution in Talos Dome, East Antarctica, for a good quantitative match to observed fabrics. Therefore, fabric variations may arise from climatic variations and these variations may be present beneath the firn-ice transition. Fabric variations then may preserve memory of past climate, as long as the fabric variation is observable. (A loose analogy can be drawn to the familiar climate proxy, $\delta^{18}\text{O}$; it is the variation in $\delta^{18}\text{O}$, not the particular amount of the oxygen isotope present, that allows us to extract a temperature history.)

Here, we ask how long a subtle fabric variation (of any origin), just below the firn-ice transition, can be preserved within an ice sheet. Kennedy and others (2013) used a model based on the tripartite paradigm to show that a subtle variation in fabric can persist throughout the depth of an

ice sheet when the ice is in a vertical uniaxial-compression or pure-shear regime and experiences polygonization events typical of ice divides. We build on this work to show that it is possible to preserve a subtle variation in fabric in a simple-shear stress regime and subject to migration recrystallization. Ice flows dominantly by simple shear on the flank of an ice sheet, while ice at the divide may experience some simple shear, especially in the case of divide migration. We also show that for any of the modeled stresses or temperatures, migration recrystallization does not ‘erase’ the fabric variation. Together, the combination of uniaxial compression, pure shear, simple shear, polygonization, and migration recrystallization account for the dominant processes within an ice sheet that affect the fabric evolution.

3.3 Fabric

A sample of ice can display a statistically preferred orientation of its crystal lattices called fabric. The statistical measure of this preference is often reported as eigenvalues and eigenvectors of the (volume-weighted) average orientation tensor of the sample. The grain volume can be determined from the measurement of the two-dimensional grain area in a cross section of the sample (Woodcock, 1977; Gagliardini and others, 2004).

The orientation tensor is calculated from a sample of N grains:

$$\mathbf{A} = \sum_{n=1}^N f_n \vec{c}_n \otimes \vec{c}_n, \quad (3.1)$$

where f_n is the estimate of the grain’s volume fraction, \vec{c}_n is a unit vector describing the grain’s c-axis orientation, and \otimes is the vector direct (outer) product. The eigenvalues, e_i , for $i = 1, 2, 3$, of \mathbf{A} then represent the spatial distribution of the orientations, and how tightly the crystals are aligned to the eigenvectors, \vec{v}_i . The eigenvalues are labeled in descending order ($e_1 > e_2 > e_3$) and sum to unity ($e_1 + e_2 + e_3 = 1$). For a single-maximum fabric, the statistically preferred orientation is the first eigenvector, \vec{v}_1 . The first eigenvalue, e_1 , measures the fabric *strength*. Fabrics typically strengthen throughout the depth of an ice sheet in response to stress-induced velocity gradients driving grain rotation in the ice (e.g., Paterson, 1991; Arnaud and others, 2000; Di Prinzio and others, 2005; Durand and others, 2007; Gow and Meese, 2007).

Microstructural processes further influence the volume orientation of ice and can significantly impact the fabric statistics. The three that affect lattice orientation are rotation recrystallization (RRX), where new grain boundaries are formed through the progressive rotation and migration of sub-grain boundaries (of which polygonization is a special case), and strain-induced boundary

migration (SIBM; also called migration recrystallization) from old/existing grains (SIBM-O) and from nucleation of new grains (SIBM-N) (see Faria and others, 2014b, appendix A). Of these three, only SIBM-N is known to affect the fabric strength significantly. RRX produces new grains, of differing size, with small lattice mis-orientations ($< 10^\circ$; Alley and others, 1995), but the volume average of these new grains, and what is left of the old grain, will closely match the average before RRX resulting in a small weakening of the fabric. SIBM-O, in a statistical sense, is erasing the orientation of a bit of ice and replacing it with an orientation drawn from the same parent distribution of grains. Given a large number of grains, this will not affect the overall fabrics statistics as long as there is not a preference to recrystallize grains in a certain orientation and the total population of grains remains large. Due to the large amount of strain heterogeneity in deforming ice, there should not be an orientation preference for SIBM-O (Faria and others, 2014b).

SIBM-N, in contrast, nucleates new grains with a random orientation (Wilson and others, 2014). The fabrics that arise when SIBM-N dominates the fabric evolution are typically aligned for easy glide in the basal planes (the softest orientation) (Montagnat and others, 2009), indicating that the nucleated grains most likely to grow are the ones oriented for easy glide. The influence of SIBM-N on a fabric variation will then depend on the rates of SIBM-N in each layer, as well as the rates of grain rotation. As long as the rates of SIBM-N remain low, or there is a differing rate in the varying layers, SIBM-N will not immediately eliminate the fabric variation (as shown below).

Therefore, due to the way fabric is influenced by the microstructural processes, and the way it is measured, we expect fabric to be particularly amenable to preserving variations.

3.4 The model

We use the topological model developed by Kennedy and others (2013), based on the analytic flow law developed by Thorsteinsson (2001, 2002). This polycrystal model solves for fabric through time, while incorporating nearest-neighbor interactions (NNI) and the tripartite parameterizations of normal grain growth, polygonization and migration recrystallization (SIBM-N). This model does not predict ice flow; therefore, it does not account for possible strain enhancements, such as impurity-enhanced ice flow (Paterson, 1991; Faria and others, 2009). Nor does it include the feedbacks between rheologically distinct layers that can lead to concentrated shearing on layers with crystals oriented to be soft in shear (Budd and Jacka, 1989; Durand and others, 2007; Pettit and others, 2007).

The model averages over a representative distribution of N individual ice crystals to calculate the bulk response of the ice to stress. The crystals are arranged on a regular cuboidal grid

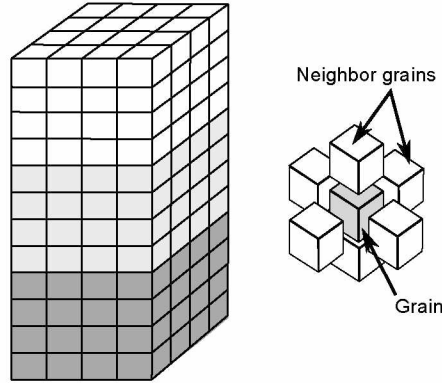


Figure 3.1: The polycrystal structure. Left: An example of a polycrystalline cuboid with three distinct fabric layers, where each color represents a different fabric. Each small cube indicates one grain and each layer has $4 \times 4 \times 4 = 64$ grains. The three-layered cuboid in our model has $20 \times 20 \times 20 = 8000$ grains in each layer. Right: An illustration of the grain packing where each grain (gray) has six neighboring grains (white).

(Figure 3.1), where each crystal has six nearest neighbors. The crystals however, are considered to evolve independently of each other and are embedded in an ice matrix. The matrix accommodates crystal-boundary migration and acts as seeds for migration recrystallization (Thorsteinsson, 2002). In the case of nearest-neighbor interactions, the resolved shear stress of the crystal is modified by a factor depending on the average orientation of the surrounding crystals.

The distribution of N crystals can be divided into sub-distributions with distinct fabrics. The evolution of each sub-distribution can then be calculated and compared with the others or with the entire distribution through time.

Each crystal in the distribution has an associated orientation, \vec{c}_n , given by the co-latitude, θ_n , and azimuth, ϕ_n , as well as an associated spherical size of diameter D_n and dislocation density ρ_n . The model accepts an initial crystal distribution, stress, and temperature, then evolves the distribution through uniform steps in time or strain. Figure 3.2 outlines the model process. First, the initial crystal distribution is created and passed to the model. The model then applies a stress to the distribution and calculates the individual crystal strain rates and velocity gradients using the flow law developed by Thorsteinsson (2001, 2002). Next, it checks the recrystallization conditions (outlined below), calculates the bulk crystal properties, and then rotates the crystals. After each time- or strain-step, the model outputs the new distribution of crystals, the bulk strain, and the number and type of recrystallization events. This new distribution of crystals is then fed back into the model for the next time-step, along with the new stress and temperature. Because stress is an input for this model, stress must be determined outside of the model.

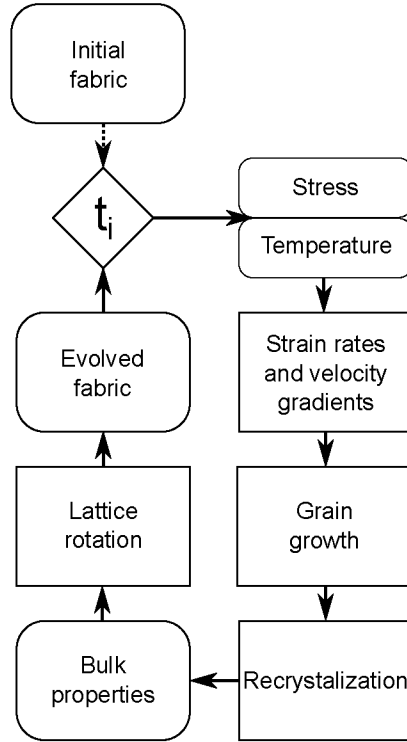


Figure 3.2: Flow chart of the model. The model is initialized with fabric data, deviatoric stress, and temperature. For each time-step, strain rates and velocity gradients are calculated, dynamic recrystallization processes are applied to the fabric and then the grains are rotated to calculate new fabric data. The new fabric data together with new stresses and temperatures are fed back into the model to start the next time-step.

3.4.1 Model physics

Grains rotate due to gradients in velocity, which result from internal stresses experienced by the ice. For polycrystalline ice, these stresses lie somewhere between two end-member assumptions: *uniform stress* and *uniform strain rates*. In the uniform-stress assumption, each grain experiences the same stress as the surrounding grains. Because ice crystals are highly anisotropic, an individual grain's strain rate, therefore, depends on its lattice orientation. In the uniform-strain-rate assumption, each grain has the same strain rate as the surrounding grains. The stress the grain experiences, then, depends on the grains' orientation. Although the true nature of ice is somewhere in between, the uniform-stress assumption is well adapted to describing polycrystalline ice due to strong crystal anisotropy (Castelnau and others, 1996). Therefore, we apply a uniform stress to each grain in the distribution. Furthermore, we restrict the deformation of a grain to be along the slip systems in the basal plane causing the grain to only respond to the components of stress that

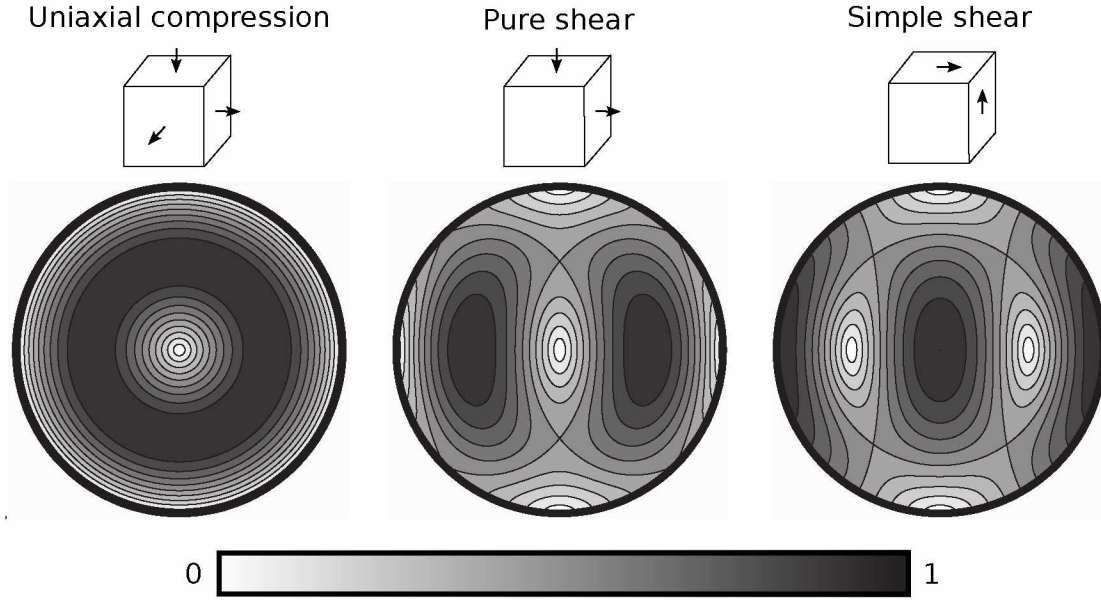


Figure 3.3: Contoured Schmidt plots of the magnitude of the resolved shear stress, \mathcal{T} . \mathcal{T} has been normalized by the maximum resolved shear stress ($\mathcal{T}/\max(\mathcal{T})$; Eqn (3.3)) for grains in the stress states of uniaxial compression, pure shear and simple shear (Eqn (3.18), (3.19), and (3.20), respectively).

are parallel to the basal plane (termed the resolved shear stress, or RSS). The RSS, $\tau^{(s)}$, on a slip system, (s) , is

$$\tau^{(s)} = \mathbf{S}^{(s)} : \boldsymbol{\sigma}', \quad (3.2)$$

where $\mathbf{S}^{(s)}$ is the Schmidt tensor, which describes the orientation of the grain's slip system (s) , $\boldsymbol{\sigma}'$ is the deviatoric stress tensor for the stress applied to the fabric, and $\mathbf{S}^{(s)} : \boldsymbol{\sigma}' = S_{kl}^{(s)} \sigma'_{kl}$ summing over repeated indexes. The magnitude of the RSS, \mathcal{T} , can then be calculated as

$$\mathcal{T} = \left| \sum_{(s)} \tau^{(s)} \hat{b}^{(s)} \right|, \quad (3.3)$$

where $\hat{b}^{(s)}$ is the direction of the Burgers vector for the slip system. Schmidt plots of \mathcal{T} for a variety of stress states are shown in Figure 3.3.

Using the analytic flow law (Thorsteinsson, 2001, 2002) the velocity gradient of a grain in response to a stress, \mathbf{L}^c , is

$$\mathbf{L}^c = \beta \mathcal{A}(T) \sum_{(s)} \mathbf{S}^{(s)} |\mathcal{E}^c \boldsymbol{\tau}^{(s)}|^{n-1} (\mathcal{E}^c \boldsymbol{\tau}^{(s)}) , \quad (3.4)$$

where β is an adjustable constant to control the isotropic ice softness, $\mathcal{A}(T)$ is the temperature-dependent flow parameter from Glen's Flow Law (Cuffey and Paterson, 2010, p. 72), \mathcal{E}^c is the local softness parameter due to nearest-neighbor interactions (NNIs), and n is the exponent in Glen's flow law (Glen, 1955).

The flow parameter $\mathcal{A}(T)$ follows an Arrhenius relation with a switch of activation energy at a transition temperature, $T_\star = -10^\circ \text{C}$. The relationship for T in kelvin is

$$\mathcal{A}(T) = \mathcal{A}_\star \exp \left(-\frac{Q_v^\pm}{R} \left[\frac{1}{T} - \frac{1}{T_\star} \right] \right) \quad (3.5)$$

where \mathcal{A}_\star is a constant, R is the universal gas constant, and Q_v^\pm is the activation energy for volume self-diffusion (Cuffey and Paterson, 2010, p. 72). $Q_v^\pm = Q_v^+ = 115 \text{ kJ mol}^{-1}$ for $T \geq T_\star$ and $Q_v^\pm = Q_v^- = 60 \text{ kJ mol}^{-1}$ for $T < T_\star$ (Table 3.1).

The local softness parameter, \mathcal{E}^c , averages the magnitude of RSS the neighboring grains are experiencing, \mathcal{T}^i , relative to the magnitude of RSS the grain is experiencing, \mathcal{T}^0):

$$\mathcal{E}^c = \frac{1}{\zeta + 6\xi} \left(\zeta + \xi \sum_{i=1}^6 \frac{\mathcal{T}^i}{\mathcal{T}^0} \right) , \quad (3.6)$$

where ζ is the relative contribution of the center grain, and ξ is the relative contribution of each neighbor (Figure 3.1). Because the RSS, \mathcal{T}^0 , can be zero, there is a specified cap for the maximum value of \mathcal{E}^c . Setting $[\zeta, \xi]$ to $[1, 0]$ in Eqn (3.6) is equivalent to the uniform-stress assumption with no NNIs. Changing the values of $[\zeta, \xi]$ modifies the uniform-stress assumption (toward the uniform-strain assumption) by redistributing the stress through explicit NNIs. Mild NNIs occur when $[\zeta, \xi]$ is set to $[6, 1]$ such that the center grain contribution to \mathcal{E}^c is the same as the sum of the neighboring grains. Full NNIs occur when $[\zeta, \xi]$ is set to $[1, 1]$ such that the center grain and individual neighbor grains all contribute equally to \mathcal{E}^c .

Finally, the strain rate of a single grain is

$$\boldsymbol{\epsilon}^c = \frac{1}{2} \left[\mathbf{L}^c + (\mathbf{L}^c)^T \right] , \quad (3.7)$$

where $(\mathbf{L}^c)^T$ refers to the matrix transpose of \mathbf{L}^c .

Table 3.1: Values of the parameters used in the model.

Parameter	Value	Eqn	Reference
Flow law constant, β	630	(3.4)	Thorsteinsson (2001)
Glen's exponent, n	3	(3.4)	Cuffey and Paterson (2010), p. 55-57
Flow law constant, \mathcal{A}_*	$3.5 \times 10^{-25} \text{ Pa}^{-3} \text{ s}^{-1}$	(3.5)	Cuffey and Paterson (2010), p. 74
Activation energy for volume self-diffusion, Q_v^\pm	$Q_v^+ = 115 \text{ kJ mol}^{-1}$ $Q_v^- = 60 \text{ kJ mol}^{-1}$	(3.5)	Cuffey and Paterson (2010), p. 72-74
Initial grain diameter, D_0	1.5 mm	(3.10)	Benson (1962)
Grain growth constant, K_0	$8.2 \times 10^{-9} \text{ m}^2 \text{ s}^{-1}$	(3.11)	Alley and others (1986); Thorsteinsson (2002)
Activation energy for grain-boundary self-diffusion, Q_b^\pm	$Q_b^+ = 81 \text{ kJ mol}^{-1}$ $Q_b^- = 42 \text{ kJ mol}^{-1}$	(3.11)	Cuffey and Paterson (2010), p. 40; Jacka and Jun (1994)
Dislocation absorption constant, α	1	(3.12)	De La Chapelle and others (1998); Montagnat and Duval (2000)
Polygonization ratio, δ	0.065		Thorsteinsson (2002)
Polygonization orientation change, $\Delta\theta$	5°		Thorsteinsson (2002)
Initial dislocation density, ρ_0	10^{10} m^{-2}		De La Chapelle and others (1998)
Minimum dislocation density to form a sub-grain boundary, ρ_p	$5.4 \times 10^{10} \text{ m}^{-2}$		De La Chapelle and others (1998)
Dislocation energy constant, μ	0.01	(3.13)	Mohamed and Bacroix (2000); Thorsteinsson (2002)
Dislocation strain field range, R_e	$\frac{1}{\sqrt{\rho}}$	(3.13)	Mohamed and Bacroix (2000)
Grain boundary energy, γ_g	0.065 J m^{-2}	(3.14)	Ketcham and Hobbs (1969)

The bulk velocity gradient is calculated by averaging the single-crystal velocity gradients, and will be influenced more by larger crystals than smaller crystals. We calculate the volume of a crystal from its diameter, D , and use its volume fraction, f , as a statistical weight for the calculation of the bulk velocity gradient (Gödert and Hutter, 1998; Montagnat and others, 2014). Therefore, the modeled bulk velocity gradient is

$$\mathbf{L}^m = \sum_{n=1}^N f_n \mathbf{L}_n^c, \quad (3.8)$$

where N is the number of crystals in the representative distribution and

$$f_n = \frac{D_n^3}{\sum_{m=1}^N D_m^3} .$$

The modeled bulk strain rate is then

$$\dot{\boldsymbol{\epsilon}}^m = \frac{1}{2} \left[\mathbf{L}^m + (\mathbf{L}^m)^T \right] . \quad (3.9)$$

However, we caution readers that this modeled strain rate will not correspond to strain rates measured *in situ*, because we are solving for fabric evolution, not ice flow. The deformation of ice is not only a function of fabric (as modeled here) but of many co-dependent processes, which accommodate ice deformation (Thorsteinsson and others, 1999). Further, using the uniform-stress assumption results in ice that is too stiff (Montagnat and others, 2014), meaning the fabric evolves too much for the modeled strain rates compared with measured strain rates. Using nearest-neighbor interactions partially alleviates this problem by allowing hard grains to deform.

Nevertheless, the cumulative modeled bulk strain, provides a good measure of the overall fabric evolution (in the context of the model), and is useful when comparing different model runs, as we do below. In order to compare results from our model with measured fabrics, the flow law constant, β (Eqn (3.4)), and parameters controlling the local softness, $[\zeta, \xi]$ (Eqn (3.6)), need to be tuned to reproduce the observed fabric evolution *in time*. How much the strain rate is under-represented in the model can then be determined. The affects of changing these parameters in our model are discussed below.

3.4.2 Recrystallization processes

Once the velocity gradient and strain rates are calculated for each grain, the parameterizations of normal grain growth, polygonization, and migration recrystallization (SIBM-N) are applied to the grain distribution before the grains are rotated into new orientations.

Normal grain growth

Under the tripartite paradigm, normal grain growth occurs when grain boundaries migrate, in order to reduce the overall grain boundary energy. The grain growth is a function of boundary curvature, intrinsic properties (e.g. temperature, thickness, diffusivity of water molecules), and extrinsic material (e.g. impurities, bubbles). This grain growth can be described by a parabolic growth law (Alley and others, 1986), where the grain diameter, D , increases with time:

$$D^2 = Kt + D_0^2, \quad (3.10)$$

where K is the grain-growth factor, t is time, t_0 is the initial time, and D_0 is the grain diameter at time t_0 . The grain-growth factor is a function of the intrinsic properties of the ice and the temperature:

$$K = K_0 \exp \left(-\frac{Q_b^\pm}{\mathcal{R}T} \right), \quad (3.11)$$

where K_0 is a constant that depends on the intrinsic properties of the grain boundaries, Q_b^\pm is the activation energy for grain-boundary self-diffusion, \mathcal{R} is the gas constant, and T is the temperature. Q_b^\pm is $\sim 0.7 \times Q_v^\pm$ (Cuffey and Paterson, 2010, p. 40) and, similarly to the activation energy for volume self-diffusion, $Q_b^\pm = Q_b^+ = 81 \text{ kJ mol}^{-1}$ for $T \geq T_\star$ and $Q_b^\pm = Q_b^- = 42 \text{ kJ mol}^{-1}$ for $T < T_\star$ (Table 3.1). Extrinsic materials, such as dust particles, reduce the rate of boundary migration and can be described by a drag force on the boundary (Alley and others, 1986). This drag effectively reduces the grain-growth factor K . We list the values used for these constants in Table 3.1.

Normal grain growth is then implemented by growing the diameter of the grain, D , according to Eqn (3.10). We reset the growth law after each recrystallization, such that t_0 and D_0 are the time and size immediately after the recrystallization.

Polygonization

Under the tripartite paradigm, a stable grain size is typically reached, even though grains continue growing through time and depth, because polygonization counteracts normal grain growth. Polygonization creates new grain boundaries within large ice grains, effectively dividing the grain in two. Large grains can become highly strained and experience differential stress, which is relieved by the organization of dislocations into sub-grain boundaries (Alley, 1992). De La Chapelle and others (1998) determined that the minimum dislocation density needed to form a sub-grain boundary is, $\rho_p = 5.4 \times 10^{10} \text{ m}^{-2}$.

Because polygonization depends on reaching a minimum dislocation density, the rate of polygonization can be indirectly described through the dislocation density's rate of change. The dislocation density changes due to two dominant processes: it increases due to work hardening and decreases due to the absorption of dislocations by the grain boundary (Miguel and others, 2001). Therefore, the change in a grain's dislocation density can be described as

$$\frac{d\rho}{dt} = \frac{\|\dot{\mathbf{e}}\|}{bD} - \alpha\rho \frac{K}{D^2}, \quad (3.12)$$

where the first term on the right describes work hardening: $\|\dot{\mathbf{e}}\|$ is second invariant of the strain rate tensor, b is the length of the Burgers vectors, and D is the grain diameter (Montagnat and Duval, 2000). The second term describes the absorption of dislocations by the grain boundaries, α is an adjustable constant and K is the grain-growth factor.

We implement polygonization such that once the minimum dislocation density is reached, a grain experiencing a differential stress may polygonize. Because our nearest-neighbor interactions only modify the RSS and cannot directly apply a differential stress, we use a proxy for differential stress on a grain (Thorsteinsson, 2002). Grains that have a small amount of the applied stress resolved onto the basal plane (RSS) will likely be experiencing a differential stress from their neighboring grains which are deforming. Specifically, if the ratio of the magnitude of the RSS, \mathcal{T} , to the second invariant of the applied stress, $\|\boldsymbol{\sigma}'\|$, is less than a given value, $\mathcal{T}/\|\boldsymbol{\sigma}'\| < \delta$, and the dislocation density, ρ , in the grain is sufficient to form a sub-grain wall ($\rho > \rho_p$), then the grain will polygonize. When a grain polygonizes, the orientation is changed by an angle, $\Delta\theta$, in a direction that increases the RSS, the grain size is halved, and the dislocation density is reduced by ρ_p . Values for these parameters are listed in Table 3.1. Polygonization tends to slow the development of fabric because grains that are oriented very close to the preferred orientation (small RSS) of the fabric will polygonize preferentially by the selection criteria. Because polygonization rotates the grains away from the preferred orientation, this process tends to weaken the fabric.

Migration recrystallization (SIBM-N)

According to the tripartite paradigm, through most of the depth of an ice sheet, the rate of fabric evolution is controlled by a balance between the grain growth, polygonization, and grain rotation processes. However, migration recrystallization dominates fabric evolution at high temperatures (typically $> -10^\circ\text{C}$; Duval and Castelnau, 1995). Migration recrystallization occurs when the stored strain energy (due to dislocations) in a grain is greater than the grain-boundary energy of a new strain-free grain. This new strain-free grain rapidly grows at the expense of the old grain (Duval and Castelnau, 1995). The stored energy due to dislocations, E_d , can be estimated as

$$E_d \simeq \mu\rho Gb^2 \ln\left(\frac{R_e}{b}\right), \quad (3.13)$$

where μ is a constant, G is the shear modulus, and R_e is the mean average of the dislocation strain field range (Thorsteinsson, 2002). The energy associated with grain boundaries, E_c , is

$$E_c = \frac{3\gamma_g}{D}, \quad (3.14)$$

where γ_g is the energy per unit area on the boundary (for high-angle boundaries). When $E_d > E_c$ it is energetically favorable to nucleate a new grain, which quickly grows to a diameter that scales with the effective stress, due to a balance between nucleation of grains and grain-boundary migration (e.g., Shimizu, 2008). The nucleated grain that grows most rapidly will be the one in the most energetically favorable position: about halfway between the compressional and tensional axes, which maximizes the resolved shear stress on the basal planes, causing them to deform easily (Alley, 1992). For uniaxial compression or pure shear, for example, this is 45° from the axis of compression, while for simple shear, it is 45° from the principal stress axis (Figure 3.3). The new grain is initially strain free and has a much lower strain energy than the surrounding grains, allowing it to grow. As the new grain grows preferentially at an orientation favorable for the bulk deformation (highest RSS), the fabric can change significantly when there are large numbers of migration recrystallization events.

We implement migration recrystallization by immediately creating a new grain when the dislocation energy, E_d , exceeds the boundary energy, E_c (Eqn (3.13) and (3.14)). An old grain is replaced with a new ‘strain-free’ grain that has a dislocation density ρ_0 and a diameter that scales with the effective stress, $D \sim (\sigma'_{kl}\sigma'_{kl}/2)^{-2/3}$ (Thorsteinsson, 2002; Shimizu, 2008). We assume the grain grows fast enough to reach a diameter of D within a single time-step. The new grain is given the orientation with the highest RSS (or softest orientation; Figure 3.3), taken from a random distribution of 50 orientations in the applied stress state (Thorsteinsson, 2002).

Lattice rotation

If the surrounding ice is fixed, each grain rotates as it deforms, according to the standard continuum mechanics rotation rate tensor:

$$\dot{\mathbf{\Omega}}^p = \frac{1}{2} \left[\mathbf{L}^c - (\mathbf{L}^c)^T \right], \quad (3.15)$$

where $\dot{\mathbf{\Omega}}^p$ is the rotation rate of a single grain and \mathbf{L}^c is the velocity gradient of a grain in response to stress from Eqn (3.4). If the surrounding ice is rotating within the frame of reference, however, the model calculates a relative grain rotation rate:

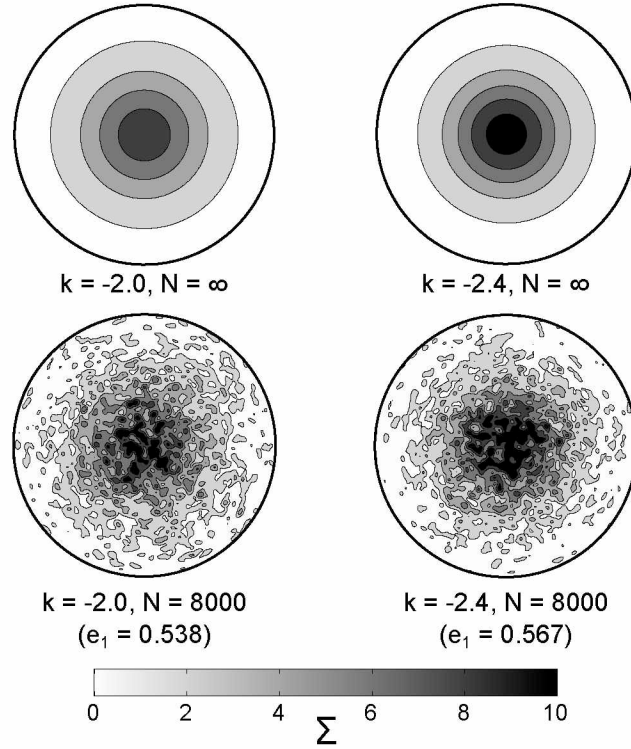


Figure 3.4: Contoured Schmidt plot of the initial fabrics for both the constant-stress and Taylor Dome experiments. The fabrics are contoured at levels of $0, 2\Sigma, \dots, 10\Sigma$. Σ is the standard deviation of the density of grains from the expected density for isotropic ice (Kamb, 1959). The upper two are contour plots of the continuous Watson distribution (an infinite number of grains) with concentration parameters $k = -2.0$ (left) and $k = -2.4$ (right). Two random 8000-grain fabrics generated from the upper Watson distributions are depicted in the lower two plots. The fabric generated from the $k = -2.0$ and $k = -2.4$ distributions have eigenvalues of $e_1 = 0.538$ and $e_1 = 0.567$, respectively.

$$\dot{\Omega}^* = \dot{\Omega}^b - \dot{\Omega}^p, \quad (3.16)$$

where $\dot{\Omega}^b$ is the bulk rotation rate of the modeled ice in response to stress. The new orientation of the grain is then

$$\vec{c}' = (\mathbf{I} + t\dot{\Omega}^*)\vec{c}. \quad (3.17)$$

3.5 Experimental setup

The model domain is a 24000 grain cuboid that is 20 grains wide, 20 grains deep, and 60 grains high (Figure 3.1). The cuboid is split into three vertically layered cubes of 8000 grains each and the

middle layer is initialized with a different fabric to the top and bottom layers. Each layer of the initial fabric is generated using a Watson distribution (Kennedy and others, 2013). The top and bottom layers have a concentration parameter for the Watson distribution of $k_{tb} = -2.0$. This results in a vertical single-maximum fabric, where the largest eigenvalue of the second-order orientation tensor is $e_1^{tb} = 0.538$. The middle layer has a stronger fabric, with a concentration parameter of $k_m = -2.4$ ($e_1^m = 0.567$). These concentration parameters are characteristic of ice fabrics found near the firn-ice transition in polar ice sheets, and correspond to fabrics at $\sim 100\text{m}$ depth in Taylor Dome, East Antarctica (Kennedy and others, 2013), and to $< 500\text{m}$ depth at Dome C, East Antarctica (Wang and others, 2003; Durand and others, 2009). We measure the fabric variation through time by calculating the difference in the fabric e_1 eigenvalues between the middle and top (or bottom) layers: $\Delta e_1 = e_1^m - e_1^t$. e_1 will best represent single-maximum-type grain distributions typically found in ice sheets. Initially, $\Delta e_1 = 0.029$. A contoured Schmidt plot of the initial fabrics is shown in Figure 3.4.

Over time, as the cuboid is stressed, Δe_1 will change and may become smaller than the uncertainty in eigenvalues, due to under-sampling the distribution with a finite number of grains. Durand and others (2006a) found the maximum under-sampling error to be $\delta = 0.004$ for a distribution with 8000 grains. For this study, we consider the minimum separation resolvable above the error in the eigenvalue calculation to be twice the maximum error: $2\delta \approx 0.01$. The fabric variation is then preserved, as long as $\Delta e_1 > 0.01$. *In situ*, the minimum separation required to measure a fabric anomaly will depend on the measurement technique, the number of grains sampled, and the assumed *in situ* distribution of orientations.

To model how our fabrics respond to stress, we apply a constant temperature, T , and constant deviatoric stress, $\boldsymbol{\sigma}'$, at each time-step. The basic stress states within an ice sheet are uniaxial compression, pure shear, and simple shear. The deviatoric-stress tensor for uniaxial compression has the form

$$\boldsymbol{\sigma}'_u = \begin{pmatrix} \frac{1}{2}\sigma'_u & 0 & 0 \\ 0 & \frac{1}{2}\sigma'_u & 0 \\ 0 & 0 & -\sigma'_u \end{pmatrix}, \quad (3.18)$$

the deviatoric-stress tensor for pure shear has the form

$$\boldsymbol{\sigma}'_p = \begin{pmatrix} \sigma'_p & 0 & 0 \\ 0 & 0 & 0 \\ 0 & 0 & -\sigma'_p \end{pmatrix}, \quad (3.19)$$

and the deviatoric-stress tensor for simple shear has the form

$$\boldsymbol{\sigma}'_s = \begin{pmatrix} 0 & 0 & \sigma'_s \\ 0 & 0 & 0 \\ \sigma'_s & 0 & 0 \end{pmatrix}. \quad (3.20)$$

We use $\sigma'_{u,p,s}$ of 0.01 MPa and 0.04 MPa to provide a lower and upper bound on the characteristic deviatoric stresses typically found in ice sheets (Pettit and Waddington, 2003). The model calculates a strain rate at each time-step, $\dot{\boldsymbol{\epsilon}}_i^m$, and then the fabric is evolved for the amount of time required to achieve a strain-step of 0.001, t_i . The total bulk strain undergone by the modeled ice is then $\boldsymbol{\epsilon} = \sum \dot{\boldsymbol{\epsilon}}_i^m t_i$.

Ice in the vicinity of an ice divide will typically experience a regime of compressive stress before experiencing significant shear stress and, for simple ice-sheet geometries, simple-shear stresses are most important in the bottom half of the ice sheet (Cuffey and Paterson, 2010). Therefore we apply a constant compressive stress regime (R1) to the modeled ice up to a total bulk strain of $\boldsymbol{\epsilon}_{R1}$. We then apply a constant-shear-stress regime (R2) to the modeled ice up to a total bulk strain of $\boldsymbol{\epsilon}_{R2}$. The shear-stress regimes consist of simple shear alone, a combination of simple shear and pure shear, or a combination of simple shear and uniaxial compression (Table 3.2).

Kennedy and others (2013) showed that the separation in eigenvalues between the fabric layers drops below 0.01 after 0.30 bulk strain in our model when undergoing uniaxial compression and pure shear. Simple shear, however, causes the fabric to rotate into a ‘soft’ orientation rather than a ‘hard’ orientation. Because the rate of grain rotation depends on the velocity gradient, the stronger fabric (soft in simple shear) will evolve more quickly than the weaker fabric (hard in simple shear). Therefore, the fabric separation between layers can increase in simple shear as the fabric evolves with each time-step. This will cause fabrics to maintain their separation to a higher modeled bulk strain than 0.30. However, after 0.35 strain in our model runs dominated by high magnitudes of uniaxial compression or pure shear, the time-step necessary for a 0.001 strain-step has increased by over three orders of magnitude due to stress hardening. Further evolution becomes computationally impractical, because time-steps that result in realistic amounts of recrystallization become too small. We therefore set $\boldsymbol{\epsilon}_{R2} = 0.35$ in our model to capture the possible enhancement of the eigen-

Table 3.2: Stress regimes, stress magnitude, nearest-neighbor interaction parameters, and temperature values used in the constant-stress experiments. Two hundred and eighty-eight model runs were computed, where each run used a permutation of the listed values. σ'_u indicates uniaxial compression, σ'_p indicates pure shear, and σ'_s indicates simple shear (Eqn (3.18)–(3.20)).

R1 \rightarrow R2	$\sigma'_{u,p}$ MPa	σ'_s MPa	NNI $[\zeta, \xi]$	T $^{\circ}\text{C}$
$\sigma'_p \rightarrow \sigma'_p$	0.01	0.01	None [1, 0]	−30
$\sigma'_u \rightarrow \sigma'_u$	0.04	0.04	Mild [6, 1]	−15
$\sigma'_p \rightarrow \sigma'_s$			Full [1, 1]	−10
$\sigma'_u \rightarrow \sigma'_s$				−5
$\sigma'_p \rightarrow \sigma'_s + \sigma'_p$				
$\sigma'_u \rightarrow \sigma'_s + \sigma'_u$				

value separation between fabric layers due to simple shear, but do not evolve the fabric further to avoid excessively large time-steps. Kennedy and others (2013) found that for dome-like and ridge-like ice sheets, 0.30 modeled bulk strain corresponds to evolution through $\sim 200\text{ka}$ while ~ 0.20 bulk strain was $\sim 100\text{ka}$. We then set $\epsilon_{R1} = 0.20$ so that ϵ_{R1} corresponds to about half of our fabric evolution time.

3.6 Results and discussion

We evolve the layered fabric shown in Figure 3.4 through each of the 288 permutations of the stress style, stress magnitudes, nearest-neighbor interaction parameters, and temperature values shown in Table 3.2. Figure 3.5 shows a contoured ternary plot of the eigenvalues for every time-step of all 288 model runs. The fabrics all evolve towards the expected single-maximum-type fabrics found in ice sheets. The layered fabric initially has an eigenvalue separation of $\Delta e_1 = 0.029$ between the top/bottom layer and the middle layer. The total amount of strain where Δe_1 is greater than the under-sampling error (0.01) depends on the rates and magnitudes of these competing processes: grain rotation; nearest neighbor interactions; the stress regime and the resulting amount of recrystallizations.

We focus on the results that best illustrate the effects of simple shear, temperature, and nearest-neighbor interactions on the eigenvalue separation. Because each of these processes affect the rate and type of recrystallization events, recrystallization is discussed throughout.

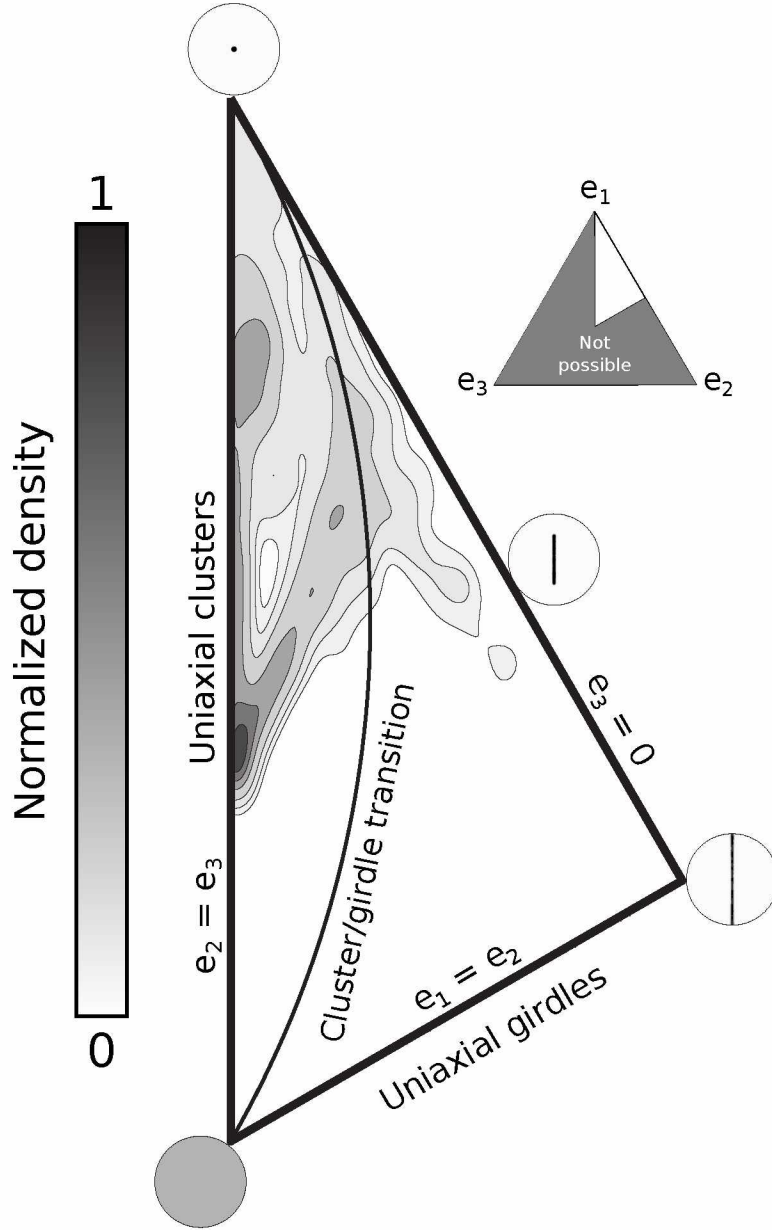


Figure 3.5: Contoured ternary plot of the eigenvalues of the fabrics for every time-step of all 288 model runs. Because by definition $e_1 > e_2 > e_3$, only 1/6 of the equilateral triangle is used. The fabric density, ρ_f has been normalized by the maximum fabric density ($\rho_f / \max(\rho_f)$). Example Schmidt plots show the fabrics with the eigenvalues directly adjacent to them.

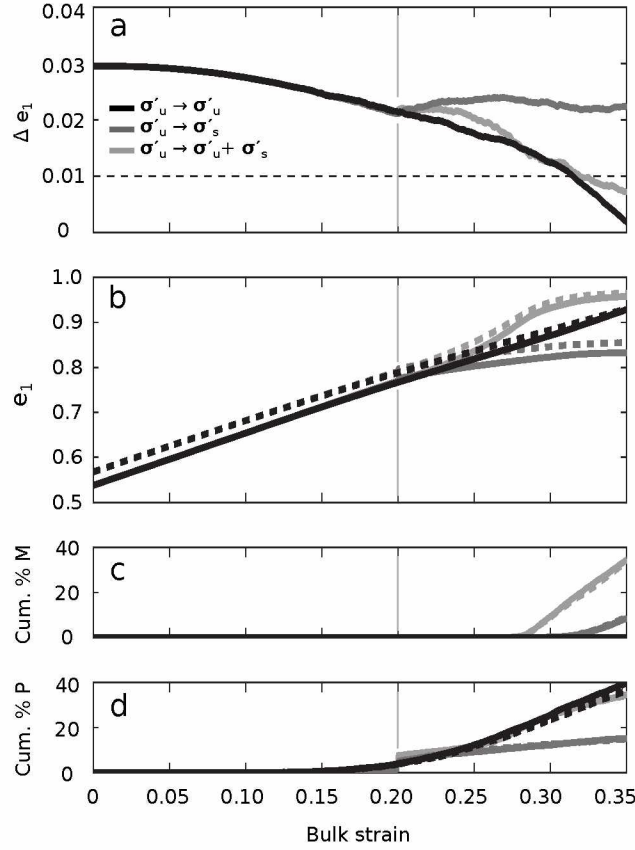


Figure 3.6: The effects of simple shear on the evolution of the layered fabric (Figure 3.4). The fabric was evolved at -30°C with mild NNI ($[\zeta, \xi] = [6, 1]$; Eqn (3.6)) and low stress magnitudes ($\sigma'_{u,s} = 0.01\text{MPa}$) for the stress regimes ($R1 \rightarrow R2$) of: uniaxial compression only ($\sigma'_u \rightarrow \sigma'_u$, black curves), uniaxial compression to simple shear ($\sigma'_u \rightarrow \sigma'_s$, dark gray curves), and uniaxial compression to uniaxial compression plus simple shear ($\sigma'_u \rightarrow \sigma'_u + \sigma'_s$, light gray curves). **a** shows the Δe_1 eigenvalue separation between the top/bottom and middle fabric layers. The horizontal dashed curves indicates the under-sampling error threshold, where Δe_1 may not be resolvable. **b-d** show the fabric evolution, the cumulative percent of grains that have undergone migration recrystallization, and the cumulative percent of grains that have undergone a polygonization event, respectively. Solid curves indicate the top/bottom layer while thick dashed curves indicate the middle layer. In all plots, light gray vertical lines mark the change from R1 to R2.

3.6.1 Simple shear

Figure 3.6 shows the evolution of the fabric for the stress regimes ($R1 \rightarrow R2$) of: uniaxial compression only ($\sigma'_u \rightarrow \sigma'_u$); uniaxial compression to simple shear ($\sigma'_u \rightarrow \sigma'_s$) and uniaxial compression to uniaxial compression plus simple shear ($\sigma'_u \rightarrow \sigma'_u + \sigma'_s$). The fabrics were evolved at -30°C with mild NNI ($[\zeta, \xi] = [6, 1]$; Eqn (3.6)) and low stress magnitudes ($\sigma'_{u,s} = 0.01\text{MPa}$).

In the $\sigma'_u \rightarrow \sigma'_s$ model run, the eigenvalue separation, Δe_1 , remains above the under-sampling error for the entire experiment. When compared with the $\sigma'_u \rightarrow \sigma'_u$ run, the fabric evolution is slowed, polygonization events happen less frequently, and there is some migration recrystallization (SIBM-N) happening at high modeled bulk strains (> 0.30). The fabric evolution is slowed down because at 0.20 modeled bulk strain, the fabrics are already mostly concentrated near vertical and the grains at the periphery of the distribution are now in the hardest orientation in simple shear (Figure 3.3). These peripheral grains rotate towards the vertical slowly, causing e_1 to increase slowly. Likewise, the polygonization frequency is reduced because the grains in a hard orientation in simple shear (and therefore likely to be experiencing a bending moment; $\mathcal{T}/\|\sigma'\| < \delta$, see the *Classical Polygonization* section above) have not yet undergone enough modeled deformation to have a high dislocation density. The grains that have a high dislocation density are very close to vertical and located in a soft orientation (therefore unlikely to be experiencing a bending moment). Further, migration recrystallization events happen at the high modeled bulk strains for this run because the soft grains that already have a high dislocation density increase their dislocation density further, to the point where migration recrystallization is possible even at such low temperatures. This agrees with observations by Kipfstuhl and others (2009), which showed that recrystallization can be active at much lower temperatures than previously suggested. Because grains that undergo migration recrystallization are given a random orientation with a high RSS, they are likely to end up with an orientation either close to vertical or close to the direction of shearing (Figure 3.3). The grains that end up pointing close to vertical will not strongly affect the fabric eigenvalues, as they stay within the vertically-clustered distribution. The fabric in the $\sigma'_u \rightarrow \sigma'_s$ model run remains largely unaffected by the low number of migration recrystallization events.

In the $\sigma'_u \rightarrow \sigma'_u + \sigma'_s$ model run, Δe_1 remains above the under-sampling error to just slightly higher modeled bulk strains than in the $\sigma'_u \rightarrow \sigma'_u$ run. Simple shear does not slow the fabric evolution in this case because the majority of grains will have a large RSS (Figure 3.3), causing a rapid evolution of the fabric to the point where the fabric is too strongly orientated to maintain much separation. Both polygonization and migration recrystallization are active in this model run, due to the high RSS, which causes high modeled strain rates and a rapid buildup of dislocations. In this stress state, migration recrystallization will grow grains in almost any orientation. However, these grains will rapidly rotate to a vertical orientation and the rate of migration recrystallization events seen here does not change the fabric eigenvalues.

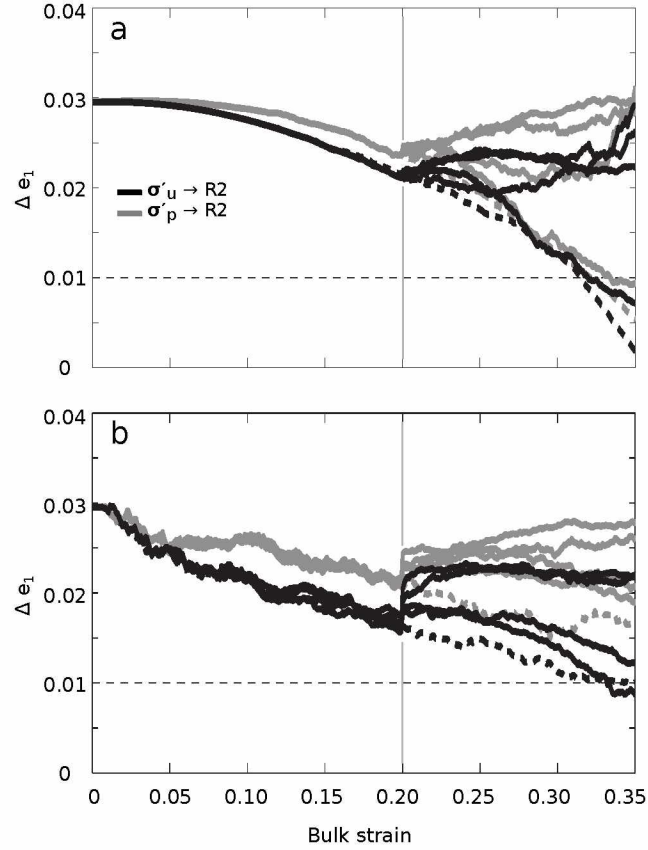


Figure 3.7: The effects of simple shear on the evolution of the layered fabric (Figure 3.4) eigenvalue separation between the top/bottom and middle fabric layer. The fabric was evolved at -30°C with mild NNI ($[\zeta, \xi] = [6, 1]$; Eqn (3.6)) in every permutation of the stress regimes ($R1 \rightarrow R2$) and stress magnitudes ($\sigma'_{u,p,s}$) shown in Table 3.2. Black curves indicate runs that started with uniaxial compression, σ'_u , while gray curves indicate runs that started with pure shear, σ'_p . **a** shows runs with a low stress magnitude initially ($\sigma'_{u,p} = 0.01\text{ MPa}$) while **b** shows a high stress magnitude initially ($\sigma'_{u,p} = 0.04\text{ MPa}$). In both plots, the horizontal dashed line indicates the under-sampling error threshold, where Δe_1 may not be resolvable and light gray vertical lines in both plots mark the change from R1 to R2.

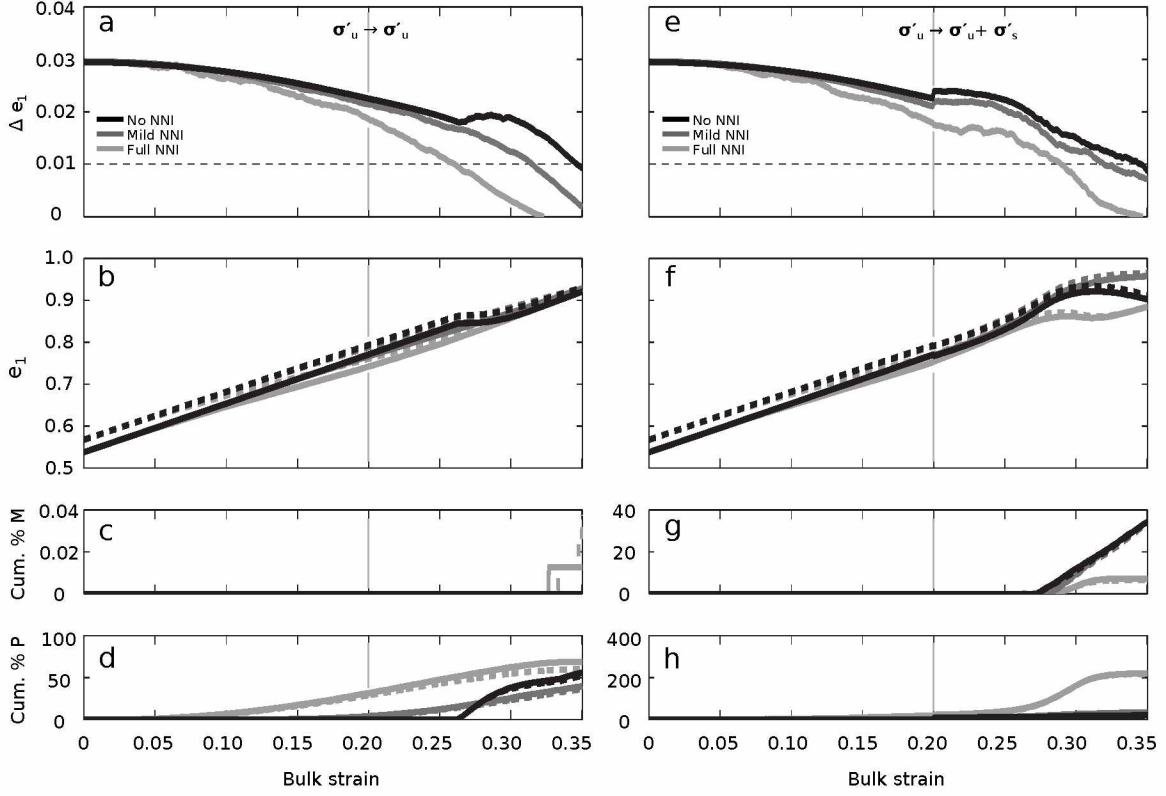


Figure 3.8: The effects of nearest-neighbor interaction (NNI) on the evolution of the layered fabric (Figure 3.4). The fabric was evolved at $T = -30^\circ\text{C}$ with each of the NNIs shown in Table 3.2. **a-d** show the evolution of uniaxial compression only ($\sigma'_u \rightarrow \sigma'_u$) with a low stress magnitude ($\sigma'_u = 0.01\text{ MPa}$) and **e-h** show the evolution of uniaxial compression plus simple shear ($\sigma'_u \rightarrow \sigma'_u + \sigma'_s$) with a low stress magnitude ($\sigma'_{u,s} = 0.01\text{ MPa}$). Black curves indicate no NNI ($[\zeta, \xi] = [1, 0]$; Eqn (3.6)), dark-gray curves indicate mild NNI ($[\zeta, \xi] = [6, 1]$), and light-gray curves indicate full NNI ($[\zeta, \xi] = [1, 1]$). **a** and **e** show the Δe_1 eigenvalue separation between the fabric's top /bottom and middle layers and horizontal dashed lines indicate the under-sampling error threshold where Δe_1 may not be resolvable. **b-d** and **f-h** show the fabric evolution, the cumulative percent of grains that have undergone migration recrystallization, and the cumulative percent of grains that have undergone a polygonization event, respectively. Solid curves indicate the fabrics top/bottom layer and dashed curves indicate the middle layer. In all plots, The light gray vertical lines mark the change from R1 to R2.

Figure 3.7 shows the Δe_1 evolution for all model runs at -30°C with mild NNI (every permutation of stress and stress magnitude shown in Table 3.2). In all cases, simple shear stress causes the modeled bulk strain at which the eigenvalue separation stays above the under-sampling error ($\Delta e_1 > 0.01$) to either remain the same (once) or increase (15 times).

3.6.2 Nearest neighbor interaction

Figure 3.8 shows the repeated evolution of the same layered fabric with no NNI ($[\zeta, \xi] = [1, 0]$; Eqn (3.6)), mild NNI ($[\zeta, \xi] = [6, 1]$), and full NNI ($[\zeta, \xi] = [1, 1]$) in the two stress regimes of uniaxial compression only ($\sigma'_u \rightarrow \sigma'_u$; Figure 3.8a–d) and uniaxial compression to uniaxial compression plus simple shear ($\sigma'_u \rightarrow \sigma'_u + \sigma'_s$; Figure 3.8e–h). The fabric was evolved using $T = -30^\circ\text{C}$ and low stress magnitudes ($\sigma'_{u,s} = 0.01\text{ MPa}$) for both the stress regimes. Higher amounts of NNIs reduce the fabric separation at earlier modeled bulk strains. This happens because nearest-neighbor interactions minimize the modeled strain-rate differences between neighboring grains, such that the grains tend to evolve towards vertical more slowly. This causes the grains to spend more time in a higher strain-rate orientation, which increases the dislocation density. A higher dislocation density allows the recrystallization processes to happen at an earlier modeled bulk strain. Polygonization then slows the fabric evolution by moving grains away from vertical. This affects the stronger fabric preferentially, as it has more hard grains that are prone to polygonization. Therefore, higher levels of NNIs decrease the modeled bulk strain at which Δe_1 remains > 0.01 .

3.6.3 Temperature

Figure 3.9 shows the repeated evolution of the same layered fabric for the temperatures of $T = -30, -15, -10, -5^\circ\text{C}$ in the two stress regimes of uniaxial compression only ($\sigma'_u \rightarrow \sigma'_u$; Figure 3.9a–d) and uniaxial compression to uniaxial compression plus simple shear ($\sigma'_u \rightarrow \sigma'_u + \sigma'_s$; Figure 3.9e–h). The fabric was evolved using mild NNI ($[\zeta, \xi] = [6, 1]$; Eqn (3.6)) and low stress magnitudes ($\sigma'_{u,s} = 0.01\text{ MPa}$) for both the stress regimes. The results from these runs fall into two sets: $T = -30, -15^\circ\text{C}$ and $T = -10, -5^\circ\text{C}$. The evolution of the fabric does not differ significantly within a set, but there is a large change in the fabric evolution between the sets, due to the step change in the activation energy Q_b (Eqn (3.11), Table 3.1). At any given modeled bulk strain, the change in activation energy results in a decrease in the eigenvalue separation, Δe_1 , a slow down of the e_1 evolution, and an increase in the polygonization events. Temperature, therefore, does not change the fabric evolution in the modeled bulk strain, except when crossing the activation energy threshold.

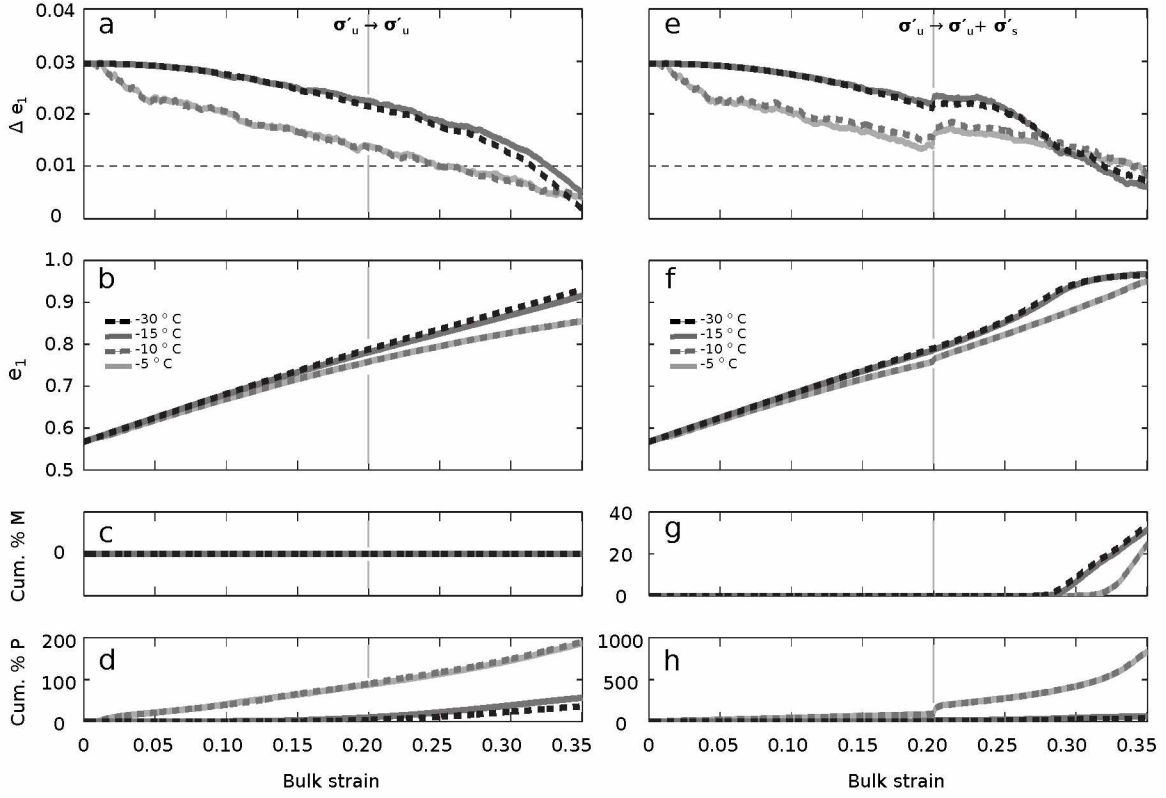


Figure 3.9: The effects of temperature on the evolution of the layered fabric (Figure 3.4). The fabric was evolved with mild NNI ($[\zeta, \xi] = [6, 1]$; Eqn (3.6)) in each of the temperature regimes shown in Table 3.2 ($T = -30, -15, -10$, and -5°C). **a-d** show the evolution of uniaxial compression only ($\sigma'_u \rightarrow \sigma'_u$) with a low stress magnitude ($\sigma'_u = 0.01\text{ MPa}$) and **e-h** show the evolution of uniaxial compression plus simple shear ($\sigma'_u \rightarrow \sigma'_u + \sigma'_s$) with a low stress magnitude ($\sigma'_{u,s} = 0.01\text{ MPa}$). The black dashed curves indicate temperatures of $T = -30^\circ\text{C}$, the solid dark-gray curves indicate $T = -15^\circ\text{C}$, the dashed dark-gray curves indicate $T = -10^\circ\text{C}$, and the light-gray curves indicate $T = -5^\circ\text{C}$. **a** and **e** show the Δe_1 eigenvalue separation between the top/bottom and middle fabric layers, and the horizontal dashed line indicates the under-sampling error threshold where Δe_1 may not be resolvable. **b-d** and **f-h** shows the fabric evolution, the cumulative percent of grains that have undergone migration recrystallization, and the cumulative percent of grains that have undergone a polygonization event, respectively. The light gray vertical lines in all plots mark the change from R1 to R2.

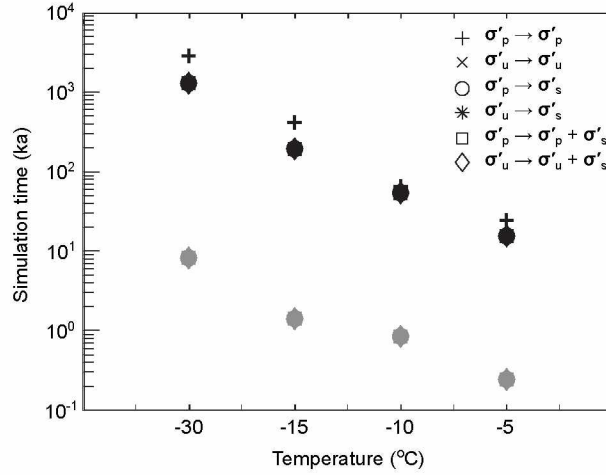


Figure 3.10: The total simulation time to evolve the fabric to 0.35 bulk strain for our different model runs. Time is shown on a logarithmic scale. Black symbols indicate runs with low stress magnitudes ($\sigma'_{u,p,s} = 0.01$ MPa) and gray symbols indicate runs with high stress magnitudes ($\sigma'_{u,p,s} = 0.04$ MPa).

Nevertheless, because ice at a warmer temperature has a larger flow parameter ($\mathcal{A}(T)$, Eqn (3.4)), the ice will deform more quickly at higher temperatures. The actual time required for the modeled ice to reach any given bulk strain will then be shorter at higher temperatures. This also means that, for model runs that drop below an e_1 separation of 0.01 at the same modeled bulk strain, the actual time elapsed will be much shorter for runs at high temperatures (Figure 3.10). Critically, migration recrystallization (SIBM-N) events are reduced for a given modeled bulk strain at the higher temperatures because of the very large number of polygonization events (which both depend on and reduce the dislocation density). Yet, because the actual time required to reach any given modeled bulk strain will be shorter, the earlier onset of migration recrystallization for higher temperatures still holds true.

3.6.4 Further discussion

In all of our experiments, a variation in fabric is either preserved or enhanced under shear stresses. There is a ‘window of opportunity’ in which the separation of eigenvalues is sufficient to observe the variation before the fabric becomes too strongly oriented to maintain much separation. The length of time this window is open depends on the magnitude of the initial fabric variation, the initial strength of the weaker fabric, the magnitude of the applied stress, the strength of the nearest neighbor interactions, and the resultant number of recrystallization events. If the initial fabric variation is sufficiently large, the weaker initial fabric controls the time the window is open –

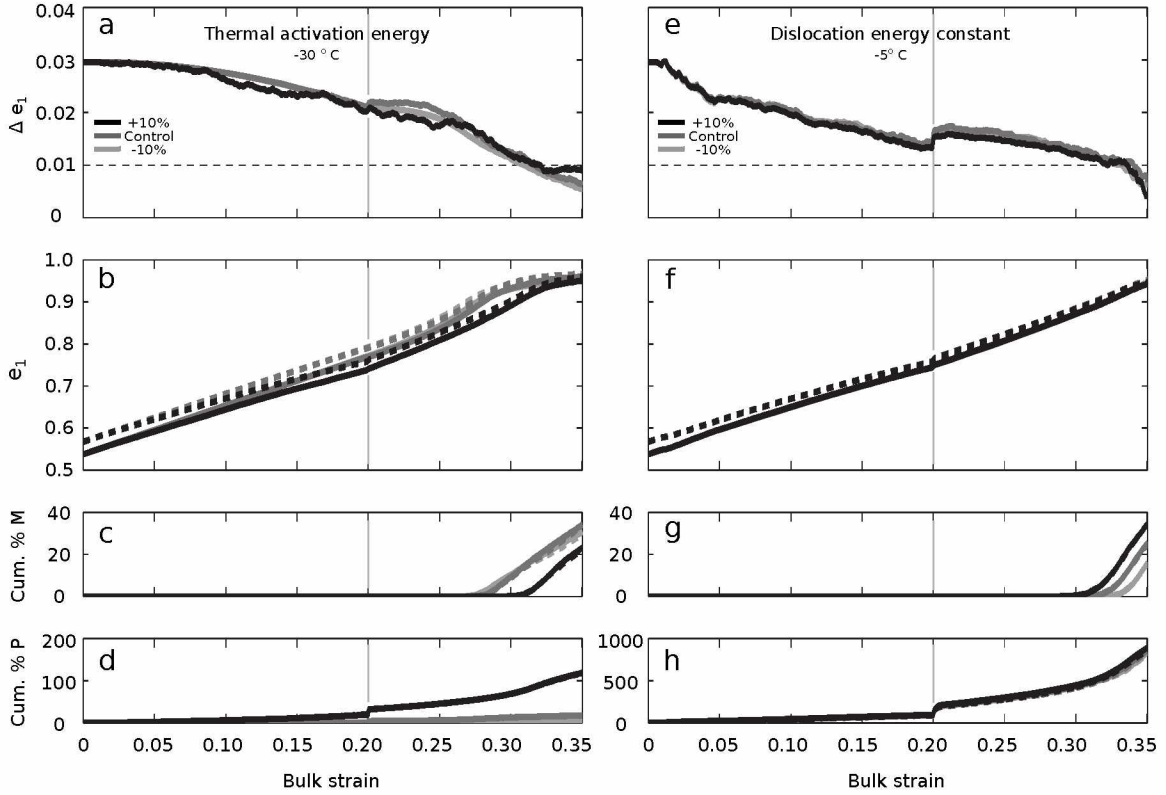


Figure 3.11: Sensitivity to the model parameters (Table 3.1). **a-d** show the result of varying the thermal activation energy, Q , at $T = -30^\circ\text{C}$ and **e-h** the result of varying the dislocation energy constant, μ , at $T = -5^\circ\text{C}$. Dark-gray curves indicate the control run while black curves indicate a 10% increase in the parameter values and the light-gray curves indicate a 10% decrease in the parameter values. **a** and **e** show the Δe_1 eigenvalue separation between the fabrics top/bottom and middle layers and horizontal dashed lines indicate the under-sampling error threshold where Δe_1 may not be resolvable. **b-d** and **f-h** shows the fabric evolution, the cumulative percent of grains that have undergone migration recrystallization, and the cumulative percent of grains that have undergone a polygonization event, respectively. Solid curves indicate the fabrics top/bottom layer and dashed curves indicate the middle layer. In all plots, the light gray vertical lines mark the change from R1 to R2.

the window closes as the weaker fabric reaches the maximum fabric strength (the stronger fabric reaches the maximum fabric strength before the weaker fabric).

By finding the modeled strain (and therefore time) at which the e_1 separation is < 0.01 , we can determine how long the window stays open. Our model results suggest that the window will stay open at least through 0.3 modeled bulk strain in most of the modeled constant-stress regimes, and shear stress will keep the window open well past 0.35 modeled bulk strain. The total simulated time for any particular run is shown in Figure 3.10 and range from a few hundred years in the warmest, highest stress cases to a few hundred thousand years in the coldest, lowest stress cases (typical of an ice divide).

However, the parameter values in Table 3.1 may be different *in situ*, because we are not modeling a specific glacier. In order to test the sensitivity of our model to these parameters, we ran a variety of experiments varying parameters with an increase or decrease of 10%. We tested changes in the isotropic ice softness by varying (1) β (Eqn (3.4)); the grain growth (which influences the change in dislocation density and the rates of polygonization and SIBM-N) by varying (2) the intrinsic grain growth factor, K_0 , and (3) the thermal activation energy, Q (Eqn (3.11) and (3.12)); and the migration recrystallization (SIBM-N) threshold by varying (4) the dislocation energy constant, μ (Eqn (3.13)). These four parameters together allow us to vary all the processes captured in our model. For each parameter, we computed a set of model runs at $T = -30^\circ\text{C}$, low uniaxial compression, low shear stress, and mild nearest-neighbor interactions. We computed another set of model runs at $T = -5^\circ\text{C}$ with the same stresses and nearest-neighbor interaction. Each set consist of a control run, a run with a 10% increase in the parameter, and a run with a 10% decrease in the parameter. In total, we computed runs for four parameters, each in two temperature regimes, with three values for the parameters for 24 more model runs.

Most of the model runs are not presented here as they show only negligible effects on the fabric evolution (the changes are smaller than the width of the plot lines). The only significant changes in results we see occur when varying the thermal activation energy, Q , at $T = -30^\circ\text{C}$ (Figure 3.11a–d) and when varying the dislocation energy constant, μ , at $T = -5^\circ\text{C}$ (Figure 3.11e–h). An increase in the thermal activation energy at $T = -30^\circ\text{C}$ caused more polygonization events, fewer migration recrystallization events and a slower fabric evolution (Figure 3.11b–d). However, because these changes are small, the e_1 separation is negligibly effected (Figure 3.11a). Decreasing the activation energy, on the other hand, had negligible effects.

Increasing the dislocation energy constant (Figure 3.11g), causes a small increase in migration recrystallization events and, likewise, a small decrease in migration recrystallization events when

the dislocation energy constant was decreased. Despite this change in migration recrystallization, the fabric evolution, polygonization, and e_1 separation were negligibly affected (Figure 3.11e, f and h). Therefore, we conclude that our model is insensitive to small changes in parameter values and the conclusions presented above are robust.

It should also be noted that the fabric eigenvalues are not a complete description of the ice and layers with the same eigenvalues may have different distributions of dislocation densities. It is possible for a fabric that has evolved to its maximum e_1 eigenvalue and/or lost the distinction between its layers ($\Delta e_1 < 0.01$) to have its layers separate again due to different levels of recrystallization. We did not observe this re-separation in any of our model runs, but it may be seen with fabrics evolved to higher bulk strains than were modeled.

3.7 Conclusions

Our model predicts that for constant shear-stress regimes, modeled bulk strains > 0.35 (for time, see Figure 3.10) are necessary to rid glacial ice of its past ‘memory’ of fabrics and stress states. In our model, shear stress preserves a subtle variation in fabric longer than in compressive stress regimes and may act to enhance the fabric variation in certain stress regimes by rotating grains into softer orientations and reducing the number of polygonization events.

Our model further predicts that temperature does not affect the modeled bulk strain at which the fabric variation is sufficient to be observed, except when crossing a thermal activation energy threshold. The model shows that the much higher levels of recrystallization observed in warm, fast-flowing ice is balanced by the increased modeled strain rates and grain rotation, such that the fabric variation may be observable past 0.35 modeled bulk strain. For any combination of the modeled stresses or temperatures, migration recrystallization (SIBM-N) does not rid the modeled fabric of its memory. However, using higher amounts of nearest-neighbor interactions within the model reduces the fabric variation for a given modeled bulk strain.

We therefore conclude that a fabric variation below the firn-ice transition, can be preserved in polar ice sheets. Because the microstructural processes active in the firn layer are dependent on climate variables, it is possible that the fabric variations arise from climate variations. In order to quantify the effects of climatic changes on the microstructure evolution in the firn layer, more work is needed. A microstructure model that is able simulate multiple fabrics with a statistically relevant number of grains, that captures the dynamics in the firn and ice region, and is coupled to a flow model, is needed.

3.8 Acknowledgements

We thank the scientific editor Sérgio H. Faria, Paul Duval and an anonymous reviewer for their detailed comments that considerably improved this manuscript. We also thank Martin Truffer, Ed Bueler, and Christina Carr for their help throughout the preparation of this manuscript. The work presented here was supported by the US National Science Foundation (NSF) grants OPP#0948247, OPP#0940650, and OPP#0636795.

3.9 References

- Adams, E.E. and D.A. Miller, 2003. Ice crystals grown from vapor onto an orientated substrate: application to snow depth-hoar development and gas inclusions in lake ice, *J. Glaciol.*, **49**(164), 8–12.
- Alley, R.B., 1992. Flow-law hypotheses for ice-sheet modeling, *J. Glaciol.*, **38**(129), 245–256.
- Alley, R.B., A.J. Gow and D.A. Meese, 1995. Mapping c-axis fabrics to study physical processes in ice, *J. Glaciol.*, **41**(137), 197–203.
- Alley, R.B., J.H. Porepezko and C.R. Bentley, 1986. Grain growth in polar ice: 1. theory, *J. Glaciol.*, **32**(112), 415–424.
- Alley, R.B., E.S. Saltzman, K.M. Cuffey and J.J. Fitzpatrick, 1990. Summertime formation of depth hoar in central Greenland, *Geophysical Research letters*, **17**(13), 2393–2396.
- Arnaud, L., J. Weiss, M. Gay and P. Duval, 2000. Shallow-ice microstructure at Dome Concordia , Antarctica, *Ann. Glaciol.*, **30**, 8–12.
- Benson, C.S., 1962. Stratigraphic studies in the snow and firn of the greenland ice sheet, *Tech. rep.*, Snow, Ice and Permafrost Research Establishment, US Army Corps of Engineers.
- Budd, W.F. and T.H. Jacka, 1989. A review of ice rheology for ice sheet modelling, *Cold Reg. Sci. Technol.*, **16**(2), 104–144.
- Carns, R., E.D. Waddington, E.C. Pettit and S.G. Warren, 2010. A model of grain growth and crystal fabric in polar snow and firn, *AGU Fall Meeting Abstracts*, D572.
- Castelnau, O., P. Duval, R.A. Lebensohn and G.R. Canova, 1996. Viscoplastic modeling of texture development in polycrystalline ice with a self-consistent approach: comparison with bound estimates, *J. Geophys. Res.*, **101**(B6), 13851–13868.

- Colbeck, S.C., 1983. Theory of metamorphism of dry snow, *J. Geophys. Res.*, **88**(C9), 5475–5482.
- Cuffey, K.M. and W.S.B. Paterson, 2010. The physics of glaciers, Butterworth-Heinemann/Elsevier, fourth ed.
- De La Chapelle, S., O. Castelnau, V. Lipenkov and P. Duval, 1998. Dynamic recrystallization and texture development in ice as revealed by the study of deep ice cores in Antarctica and Greenland, *J. Geophys. Res.*, **103**(B3), 5091–5105.
- Di Prinzio, C.L., L.A. Wilen, R.B. Alley, J.J. Fitzpatrick, M.K. Spencer and A.J. Gow, 2005. Fabric and texture at Siple Dome, Antarctica, *J. Glaciol.*, **51**(173), 281–290.
- Durand, G., O. Gagliardini, T. Thorsteinsson, A. Svensson, S. Kipfstuhl and D. Dahl-Jensen, 2006a. Ice microstructure and fabric: An up to date approach to measure textures, *J. Glaciol.*, **52**(179), 619–630.
- Durand, G., F. Gillet-Chaulet, A. Svensson, O. Gagliardini, S. Kipfstuhl, J. Meyssonier, F. Parrenin, P. Duval and D. Dahl-Jensen, 2007. Change in ice rheology during climate variations – implications for ice flow modelling and dating of the EPICA Dome C core, *Climate of the Past*, **3**(1), 155–167.
- Durand, G., A. Svensson, A. Persson, O. Gagliardini, F. Gillet-Chaulet, J. Sjolte, M. Montagnat and D. Dahl-Jensen, 2009. Evolution of the texture along the EPICA Dome C ice core, *Low Temperature Science*, **68**(Sup.), 91–105.
- Durand, G., J. Weiss, V. Lipenkov, J.M. Barnola, G. Krinner, F. Parrenin, B. Delmonte, C. Ritz, P. Duval, R. Röthlisberger and M. Bigler, 2006b. Effect of impurities on grain growth in cold ice sheets, *J. Geophys. Res.*, **111**(F01015).
- Duval, P. and O. Castelnau, 1995. Dynamic recrystallization of ice in polar ice sheets, *Journal de Physique IV*, 197–205.
- Faria, S.H., S. Kipfstuhl, N. Azuma, J. Freitag, I. Weikusat, M.M. Murshed and W.F. Kuhs, 2009. The multiscale structure of antarctica part I: Inland ice, *Low Temperature Science*, **68**(Sup.), 39–59.
- Faria, S.H., S. Kipfstuhl, I. Weikusat, A. Miyamoto, N. Azuma and T. Hondoh, 2011. Subgrain boundaries in Antarctic ice quantified by X-ray Laue diffraction, *J. Glaciol.*, **57**(201), 85–94.

- Faria, S.H., I. Weikusat and N. Azuma, 2014a. The microstructure of polar ice. Part I: Highlights from ice core research, *Journal of Structural Geology*, **61**, 2–20.
- Faria, S.H., I. Weikusat and N. Azuma, 2014b. The microstructure of polar ice. Part II: State of the art, *Journal of Structural Geology*, **61**, 21–49.
- Fujita, S., J. Okuyama, A. Hori and T. Hondoh, 2009. Metamorphism of stratified firn at Dome Fuji, Antarctica: A mechanism for local insolation modulation of gas transport conditions during bubble close off, *J. Geophys. Res.*, **114**(F03023), 1–21.
- Gagliardini, O., G. Durand and Y. Wang, 2004. Grain area as a statistical weight for polycrystal constituents, *J. Glaciol.*, **50**(168), 87–95.
- Glen, J.W., 1955. The creep of polycrystalline ice, *Proceedings of the Royal Society of London. Series A, Mathematical and Physical Sciences*, **228**(1175), 519–538.
- Gödert, G. and K. Hutter, 1998. Induced anisotropy in large ice shields: theory and its homogenization, *Continuum Mechanics and Thermodynamics*, **10**(5), 293–318.
- Gow, A.J. and D. Meese, 2007. Physical properties, crystalline textures and c-axis fabrics of the Siple Dome (Antarctica) ice core, *J. Glaciol.*, **53**(183), 573–584.
- Gow, A.J., D.A. Meese, R.B. Alley, J.J. Fitzpatrick, S. Anandakrishnan, G.A. Woods and B.C. Elder, 1997. Physical and structural properties of the Greenland Ice Sheet Project 2 ice core : A review, *J. Geophys. Res.*, **102**(C12), 26,559–26,575.
- Gusmeroli, A., E.C. Pettit, J.H. Kennedy and C. Ritz, 2012. The crystalline fabric of glacial ice from full-waveform borehole sonic logging, *J. Geophys. Res.*, **117**(F03021), 1–13.
- Jacka, T.H. and Li Jun, 1994. The steady-state crystal size of deforming ice, *Ann. Glaciol.*, **20**, 13–18.
- Kamb, W.B., 1959. Ice petrofabric observation from Blue Glacier, Washington, in relation to theory and experiment, *J. Geophys. Res.*, **64**(11), 1891–1909.
- Kennedy, J.H., E.C. Pettit and C.L. Di Prinzio, 2013. The evolution of crystal fabric in ice sheets and its link to climate history, *J. Glaciol.*, **59**(214), 357–373.
- Ketcham, W.M. and P.V. Hobbs, 1969. An experimental determination of the surface energies of ice, *Philosophical Magazine*, **19**(162), 1161–1173.

- Kipfstuhl, S., S.H. Faria, N. Azuma, J. Freitag, I. Hamann, P. Kaufmann, H. Miller, K. Weiler and F. Wilhelms, 2009. Evidence of dynamic recrystallization in polar firn, *J. Geophys. Res.*, **114**(B5), 1–10.
- Kipfstuhl, S., I. Hamann, A. Lambrecht, J. Freitag, S.H. Faria, D. Grigoriev and N. Azuma, 2006. Microstructure mapping: A new method for imaging deformation-induced microstructural features of ice on the grain scale, *J. Glaciol.*, **52**(178), 398–406.
- Miguel, M.-C., A. Vespignani, S. Zapperi, J. Weiss and J.-R. Grasso, 2001. Intermittent dislocation flow in viscoplastic deformation, *Nature*, **410**(6829), 667–671.
- Mohamed, G. and B. Bacroix, 2000. Role of stored energy in static recrystallization of cold rolled copper single and multicrystals, *Acta Materialia*, **48**(13), 3295–3302.
- Montagnat, M., D. Buiron, L. Arnaud, A. Broquet, P. Schlitz, R. Jacob and S. Kipfstuhl, 2012. Measurements and numerical simulation of fabric evolution along the Talos Dome ice core, Antarctica, *Earth and Planetary Science Letters*, **357–358**, 168–178.
- Montagnat, M., O. Castelnau, P.B. Bons, S.H. Faria, O. Gagliardini, F. Gillet-Chaulet, F. Grennerat, A. Griera, R.A. Lebensohn, H. Moulinec, J. Roessiger and P. Suquet, 2014. Multiscale modeling of ice deformation behavior, *Journal of Structural Geology*, **68**, 78–108.
- Montagnat, M., G. Durand and P. Duval, 2009. Recrystallization processes in granular ice, *Low Temperature Science*, **68**(Sup.), 81–90.
- Montagnat, M. and P. Duval, 2000. Rate controlling processes in the creep of polar ice, influence of grain boundary migration associated with recrystallization, *Earth and Planetary Science Letters*, **183**, 179–186.
- Nelson, J. and C. Knight, 1998. Snow crystal habit changes explained by layer nucleation, *J. Atmos. Sci.*, **55**(8), 1452–1465.
- Obbard, R., I. Baker and K. Sieg, 2006. Using electron backscatter diffraction patterns to examine recrystallization in polar ice sheets, *J. Glaciol.*, **52**(179), 546–557.
- Paterson, W.S.B., 1991. Why ice-age ice is sometimes “soft”, *Cold Regions Science and Technology*, **20**, 75–98.

- Pettit, E.C., T. Thorsteinsson, P.H. Jacobson and E.D. Waddington, 2007. The role of crystal fabric in flow near an ice divide, *J. Glaciol.*, **53**(181), 277–288.
- Pettit, E.C., T. Thorsteinsson, E.D. Waddington, W.D. Harrison, J.L. Morack, D.H. Elsberg and M.A. Zumberge, 2011. The crossover stress, anisotropy and the flow law at Siple Dome, West Antarctica, *J. Glaciol.*, **57**(201), 39–52.
- Pettit, E.C. and E.D. Waddington, 2003. Ice flow at low deviatoric stress, *J. Glaciol.*, **49**(166), 359–369.
- Shimizu, I., 2008. Theories and applicability of grain size piezometers: The role of dynamic recrystallization mechanisms, *Journal of Structural Geology*, **30**(7), 899–917.
- Thorsteinsson, T., 2001. An analytical approach to deformation of anisotropic ice-crystal aggregates, *J. Glaciol.*, **47**(158), 507–516.
- Thorsteinsson, T., 2002. Fabric development with nearest-neighbor interaction and dynamic recrystallization, *J. Geophys. Res.*, **107**(B1,2014), 1–13.
- Thorsteinsson, T., E.D. Waddington, K.C. Taylor, R.B. Alley and D.D. Blankenship, 1999. Strain rate enhancement at Dye 3, Greenland, *J. Glaciol.*, **45**(150), 338–345.
- Wang, Y., S. Kipfstuhl, N. Azuma, T. Thorsteinsson and H. Miller, 2003. Ice-fabrics study in the upper 1500 m of the Dome C (East Antarctica) deep ice core, *Ann. Glaciol.*, **37**(1), 97–104.
- Wilson, C.J.L., M. Peternell, S. Piazzolo and V. Luzin, 2014. Microstructure and fabric development in ice: Lessons learned from in situ experiments and implications for understanding rock evolution, *Journal of Structural Geology*, **61**, 50–77.
- Woodcock, N.H., 1977. Specification of fabric shapes using an eigenvalue method, *Geological Society Of America Bulletin*, **88**, 1231–1236.

Chapter 4

PISM-FEvoR: a multi-scale ice flow model incorporating fabric evolution with recrystallization¹

4.1 Abstract

The deformation of ice within an ice-sheet is anisotropic when there is a preferred orientation to the ice crystallites (grains) due to the strong anisotropy of the crystalline lattice. This preferred orientation (often termed fabric) is widely observed in ice-sheets. In recent years there has been significant effort to connect polycrystalline fabric evolution models with ice-sheet flow models to better account for the anisotropic response of ice to stress. These resulting ice-sheet models, such as the CAFFE (Placidi and others, 2010) and GOLF (Gillet-Chaulet and others, 2005) models, use external polycrystalline fabric models to tune microstructural parameters which control the fabric development and recrystallization equations. Because these ice-sheet models do not directly include the fabric models, they assume the evolution equations for the microstructure are steady over time.

We develop a combined polycrystalline-flow model (PISM-FEvoR), using the open-source Parallel Ice Sheet Model (PISM) and the open source Fabric Evolution with Recrystallization polycrystalline model (FEvoR). PISM-FEvoR provides the first integrated flow-fabric model that explicitly computes the fabric evolution and includes all three major recrystallization processes – grain growth, rotation recrystallization, and migration recrystallization. Because FEvoR is directly incorporated into PISM, PISM-FEvoR does not require steady material parameters. We use PISM-FEvoR to model the evolution of a slab-on-slope glacier, initialized with a variety of fabric profiles. PISM-FEvoR captures the flow enhancement due to fabric and we show that the entire integrated fabric-flow history determines the final simulated flow. We provide a further, independent validation of using an integrated fabric-flow model over a constant enhancement factor in ice sheet models.

4.2 Introduction

An ice sheet is made up of an unfathomably large number of ice crystallites, or grains, which determine its bulk material properties and overall response to stress. Thus the natural flow of an ice sheet is a many-scale process. The deformation of a single ice crystal in response to stress is governed by meso-scale (\approx nm) dynamics of lattice dislocations and is highly anisotropic. The

¹This chapter is being prepared for submission to the Journal of Glaciology as Kennedy, J. H., Khroulev, C., and Pettit, E.C. (In prep). PISM-FEvoR: a multi-scale ice flow model incorporating fabric evolution with recrystallization.

deformation of polycrystalline ice (macro-scale; $\approx \text{cm} - \text{m}$) is a balance between lattice dislocation dynamics, grain compatibility, and active recrystallization processes (micro-scale; $\approx \mu\text{m}$). Further up the scale, the emergent flow of an ice sheet ($> \text{km}$) is the integrated polycrystalline response to stresses that arise from the overall ice sheet geometry. Understanding and connecting the many-scale processes present in ice sheets is a complex task and an active area of research (see the reviews by Montagnat and others, 2014; Faria and others, 2014a,b).

There are a number of micro-scale processes active within glaciers and ice sheets that affect the fabric (grain orientation distribution) and texture (grain size and shape). In deforming ice ($\gtrsim 20 \text{ m}$ depth; Faria and others, 2014b), fabric develops through lattice rotation by intra-crystalline slip in response to stress (Azuma and Higashi, 1985; Alley, 1992). Dynamic recrystallization further influences the fabric and texture throughout the depth of an ice sheet. Dynamic recrystallization (DRX) includes rotation recrystallization (RRX), where new grain boundaries are formed through the progressive rotation of the crystalline lattice and the migration of sub-grain boundaries (of which polygonization is a special case involving tilt boundaries). DRX also includes migration recrystallization which involves strain-induced boundary migration (SIBM) from old/existing grains (SIBM-O) and from nucleation of new grains (SIBM-N) (see Faria and others, 2014b, appendix A). The growth of grains and the fabric strength are then emergent properties of these interdependent processes.

Polycrystalline models take either a full-field or mean-field approach (e.g., Montagnat and others, 2014). Full-field models simulate the full micro-mechanical fields and explicitly include the recrystallization processes (Montagnat and others, 2014). Full-field approaches are complex and are computationally limited to 2D simulations of a few hundred grains, though in principle could be applied across a full 3D (Becker and others, 2008). Mean-field models, on the other hand, calculate the statistical response to stress of (mostly) independent crystallites to and average their responses to determine the macroscopic response of the polycrystal. Mean field models can contain phenomenological descriptions of dynamic recrystallization processes (e.g., Azuma, 1994; Castelnau and others, 1996; Thorsteinsson, 2002). This approach is significantly less computationally intensive and has been used to model tens of thousands of grains (Kennedy and others, 2013; Kennedy and Pettit, 2015). However, fully incorporating a mean-field model into an ice-sheet scale flow model, in order to resolve the microstructural physics, has remained outside the bounds of computational feasibility (Montagnat and others, 2014).

Table 4.1: Notation. We will represent vectors as \vec{v} with scalar elements v_i , second rank tensors as \mathbf{A} with elements A_{ij} , and fourth rank tensors as $\overline{\overline{\mathbf{B}}}$ with elements B_{ijkl} . Tensor operations follow the notation below, summing over repeated indices.

Tensor operations		
$\mathbf{A} : \mathbf{B} = c$	\Leftrightarrow	$A_{ij}B_{ij} = c$
$\mathbf{A} \otimes \mathbf{B} = \overline{\overline{\mathbf{C}}}$	\Leftrightarrow	$A_{ij}B_{kl} = C_{ijkl}$
$\overline{\overline{\mathbf{A}}} : \mathbf{B} = \mathbf{C}$	\Leftrightarrow	$A_{ijkl}B_{kl} = C_{ij}$

In ice-sheet flow models, glacier ice was historically assumed to behave isotropically in response to stress. Early field observations were well-described by what came to be known as the Glen-Nye flow law (Glen, 1955; Nye, 1957):

$$\dot{\boldsymbol{\epsilon}} = \mathcal{A}(T)\sigma_e^{n-1}\boldsymbol{\sigma}, \quad (4.1)$$

where $\dot{\boldsymbol{\epsilon}}$ is the strain rate, $\mathcal{A}(T)$ is scalar softness parameter with an Arrhenius dependence on the temperature T , $\boldsymbol{\sigma}$ is the applied deviatoric stress, $\sigma_e^2 = (\boldsymbol{\sigma} : \boldsymbol{\sigma})/2$ is the effective stress, and n is the stress exponent. Modern field measurements have shown some discrepancies with flow predicted from the Glen-Nye flow law; much of which can be attributed to the fabric in the ice sheet (e.g., Thorsteinsson and others, 1999). Because the development of fabric in ice sheets is typically favorable for deformation (Hooke, 2005), it has become common to modify Eqn (4.1) with a constant scalar enhancement factor E ,

$$\dot{\boldsymbol{\epsilon}} = E\mathcal{A}(T)\sigma_e^{n-1}\boldsymbol{\sigma}, \quad (4.2)$$

where E typically takes on a value $E \geq 2$ for ice undergoing shear, and can be as large as $E = 12$ in polar ice (Cuffey and Paterson, 2010, p. 77). The use of different enhancement factors for different boundary stress regimes, however, suggests that a scalar enhancement factor does not fully explain the effects of fabric on flow (Ma and others, 2010).

In recent years there has been significant effort put forth to connect polycrystal scale models with ice-sheet scale flow models (see the review by Montagnat and others (2014)). Two models have come out of this effort, the Continuum-mechanical Anisotropic Flow model based on an anisotropic Flow Enhancement factor (CAFFE; Placidi and others, 2010) and the General Orthotropic Linear Flow law (GOLF; Gillet-Chaulet and others, 2005).

CAFFE is based on the theory of continuous diversity and uses an orientation dependent density function (D) to update a scalar enhancement factor field $E^*(D)$ in the Glen-Nye flow law (Eqn (4.2)). Because of the simple change to the flow law, The CAFFE model is easy to implement in existing ice flow models and incorporates grain rotation, strain-induced lattice rotation, rotation recrystallization as a diffusive process, and migration recrystallization as a dissipative process in the evolution of the fabric. However, the material parameters controlling rotation recrystallization and migration recrystallization are not easy to measure experimentally and must be determined from in situ observations or a polycrystalline model (Placidi and others, 2010). Further, the evolution equations for the microstructure are steady over time, and therefore are unable to account for any changes to the material parameters over time.

Alternatively, GOLF modifies the Glen-Nye flow law (Eqn (4.2)) to use six dimensionless viscosities to calculate an orthotropic material response to stress. The viscosities are a function of the second-order orientation tensor $\mathbf{a}^{(2)}$ and are tabulated initially using a polycrystalline model. $\mathbf{a}^{(2)}$ is assumed to evolve solely by deformation and does not include recrystallization processes, though could in principle include rotation recrystallization as a diffusive process and migration recrystallization as a dissipative process similar to the CAFFE model. These recrystallization parameters would also need to be determined from the polycrystalline model used to tabulate the six viscosities. Like CAFFE, these material parameters are steady in time.

In both the CAFFE and GOLF models, the fabric is described as a Eulerian fabric field, and the fabric field is evolved both due to convection and the local stress balance. These kind of approaches are computationally efficient, but including time varying material parameters would require the development of conservation equations for each parameter. The form these equations may take is not obvious, and many possible solutions may exist that would need to be validated against polycrystalline models and observations (Placidi and others, 2010; Montagnat and others, 2014; Faria and others, 2014b). Alternatively, the fabric-field can be described by Lagrangian particles, each of which contains its own polycrystalline model. This allows already validated polycrystalline models to be used, and the ability to change the material parameters from particle to particle. For example, particles could be seeded at the surface of an ice sheet over time and given the material parameters existing at the time of their seeding. These parameters may be derived from paleoclimate records (such as impurity concentration or grain size), and time-variant material parameters can then be studied. This, however, will come at a large computational cost as each particle must run its own polycrystalline model.

Though no polycrystalline model has been incorporated into a full ice-sheet model, some smaller scale attempts at integrating them (without recrystallization) have been made. For example, Rudolph and Manga (2012) implemented a mean-field model (simplified from Thorsteinsson, 2001, 2002) into a finite-difference model of Galilean ice-shells. Using a 2D 41×41 Eulerian grid, and a parallel solver, the inclusion of the mean-field model resulted in a $100\times$ increase in runtime. A fully integrated model, incorporating recrystallization, and capable of simulating fully 3D ice sheets is our development goal.

Here, we present the beginnings of the integrated polycrystalline-flow model PISM-FEVOR which combines the open source flow model PISM (Parallel Ice Sheet Model) with the open source mean-field polycrystalline model FEVOR (Fabric Evolution with Recrystallization). Similar to CAFFE, we calculate a scalar enhancement factor field ($E^*(\sigma)$) which is dependent on the applied stress. Instead of using an evolution equation with tuned parameters from a polycrystalline model, we run a number of FEVOR models directly within PISM to calculate $E^*(\sigma)$. Each FEVOR model is contained within a trace particle which freely flows within the PISM model. $E_l^*(\sigma)$ is calculated from each particle P_l , and $E^*(\sigma)$ is determined for the PISM ice domain. We are therefore able to adjust material parameters from particle to particle.

We use PISM-FEVOR to investigate the evolution of fabric in a slab-on-slope glacier. By using different initial fabric profiles within the slab, we show that we are able to model effects of fabric on the overall flow field comparably to other fabric-flow models' results. We also show that the full fabric-evolution history affects the total flow achieved at the end of the simulation, and therefore a constant scalar enhancement factor is inadequate to model the evolution of an ice sheet. This further validates similar findings from both the CAFFE and GOLF models.

Importantly, we are focused here on model development. PISM-FEVOR is among the first steps into the realm of directly integrating a polycrystal scale model within an ice-sheet scale flow model, and we have necessarily used a simplified model domain. It will provide an open example to the scientific community on how to tackle such an integration, and provide an avenue to fully integrate a mean-field model into an ice-sheet model which can be used for complicated domains such as Greenland and Antarctica.

4.3 FEVOR

To model the fabric evolution, we use the open-source Fabric Evolution with Recrystallization (FEVOR) library developed at the University of Alaska Fairbanks (FEvOR, 2015). FEVOR is actively under development and based on the model described in Kennedy and others (2013) and

Kennedy and Pettit (2015). FEVOR is a mean-field fabric evolution model in that it calculates the average polycrystalline response from a distribution of (mostly) independent crystallites, or grains. FEVOR modifies the Reuss model (uniform stress) through explicit nearest-neighbor interactions between grains. Additional (slight) differences between the FEVOR library presented here and the model in Kennedy and others (2013) and Kennedy and Pettit (2015) are detailed below.

Due to the strong anisotropic response of a grain to stress, deformation is restricted to the basal planes, whose slip systems are described by the three Burgers vectors $\vec{b}^{(s)}$. The orientation of a grain's slip systems are then described by the three Schmidt tensors

$$\mathbf{S}^{(s)} = \vec{b}^{(s)} \otimes \vec{c} . \quad (4.3)$$

where \vec{c} is the optical or c-axis the crystal and \otimes is the vector direct (dyadic) product (Table 4.1). The velocity gradient (\mathbf{L}^c) of a grain in response to a stress can then be described by:

$$\mathbf{L}^c = \beta \mathcal{A}(T) (\mathcal{E}^c)^n \sum_{(s)} |\mathbf{S}^{(s)} : \boldsymbol{\sigma}|^{n-1} \mathbf{S}^{(s)} (\mathbf{S}^{(s)} : \boldsymbol{\sigma}) , \quad (4.4)$$

where the super script c indicates a grain (crystallite) property, β is an adjustable constant to control the isotropic ice softness, $\mathcal{A}(T)$ is the temperature dependent flow parameter from the Glen-Nye flow law (Eqn (4.2); Cuffey and Paterson, 2010, p. 72), $\mathbf{S}^{(s)}$ is the Schmidt tensor which describes the orientation of the grain's slip system (s), \mathcal{E}^c is the local softness parameter due to nearest-neighbor interactions (NNIs), $\boldsymbol{\sigma}$ is the deviatoric stress tensor for the stress applied to the fabric, and n is the exponent in the Glen-Nye flow law (Eqn (4.2)). If we notice that $\mathbf{S}^{(s)} (\mathbf{S}^{(s)} : \boldsymbol{\sigma}) = (\mathbf{S}^{(s)} \otimes \mathbf{S}^{(s)}) : \boldsymbol{\sigma}$ (see Table 4.1 for notation), we can rewrite Eqn (4.4) as:

$$\begin{aligned} \mathbf{L}^c &= \beta \mathcal{A}(T) (\mathcal{E}^c)^n \sum_{(s)} |\mathbf{S}^{(s)} : \boldsymbol{\sigma}|^{n-1} (\mathbf{S}^{(s)} \otimes \mathbf{S}^{(s)}) : \boldsymbol{\sigma} \\ &= \overline{\overline{\mathbf{M}^c}}(\boldsymbol{\sigma}) : \boldsymbol{\sigma} , \end{aligned} \quad (4.5)$$

where $\overline{\overline{\mathbf{M}^c}}(\mathbf{S}^{(s)}, \boldsymbol{\sigma})$ is a fourth rank tensor, conceptually identical to the elasticity tensor, but in this case is a nonlinear function of the stress tensor (Rudolph and Manga, 2012; Montagnat and others, 2014). Eqn (4.5) is used here, while Eqn (4.4) was used in Kennedy and Pettit (2015).

The bulk velocity gradient, \mathbf{L} , of a distribution of grains in response to stress is calculated by applying a volume-weighted average (Gagliardini and others, 2004) to the individual grain responses:

$$\mathbf{L} = \overline{\overline{\mathbf{M}}}(\boldsymbol{\sigma}) : \boldsymbol{\sigma} \quad (4.6)$$

where

$$\overline{\overline{\mathbf{M}}}(\boldsymbol{\sigma}) = \sum_{n=1}^N f_n \overline{\overline{\mathbf{M}}}_n^c(\boldsymbol{\sigma}) , \quad (4.7)$$

N is the number of grains within a distribution,

$$f_n = \frac{D_n^3}{\sum_{m=1}^N D_m^3} \quad (4.8)$$

is a grain's volume fraction, and D_n is the grain diameter.

The migration recrystallization computation has also been simplified. Previously, when a grain underwent migration recrystallization, 50 random orientations (uniform on surface of \mathbb{S}^2) were generated, and the recrystallized grain was given the orientation with the highest magnitude of the resolved shear stress,

$$\mathcal{T} = \left\| \sum_{(s)} \tau^{(s)} \vec{b}^{(s)} \right\| , \quad (4.9)$$

where $\tau^{(s)}$ are the components of stress resolved onto (s) , and $\vec{b}^{(s)}$ is the Burgers vector for the slip system (s) . Schmidt plots of \mathcal{T} for a variety of stress states are shown in Figure 4.1. Instead, FEVOR now determines which component of the deviatoric stress tensor is dominant ($\max(|\sigma'_{ij}|)$). If shear stresses are dominant, \mathcal{T} is maximized near vertical (Figure 4.1) and the orientation is randomly generated with a uniform probability on the conical section of \mathbb{S}^2 defined by $\theta \in [0, \pi/6]$, and $\phi \in [0, 2\pi)$. If compressive stresses are dominant, \mathcal{T} is maximized near the small circle 45° from vertical (Figure 4.1) and the orientation is randomly generated with a uniform probability on the section of \mathbb{S}^2 defined by $\theta \in [\pi/6, \pi/3]$, and $\phi \in [0, 2\pi)$.

FEVOR can generate distributions of N orientations using the Watson orientation distribution function as described in (Kennedy and others, 2013). The probability density of finding an orientation \vec{c} for a Watson distribution with a principal axis $\vec{\eta}$ is

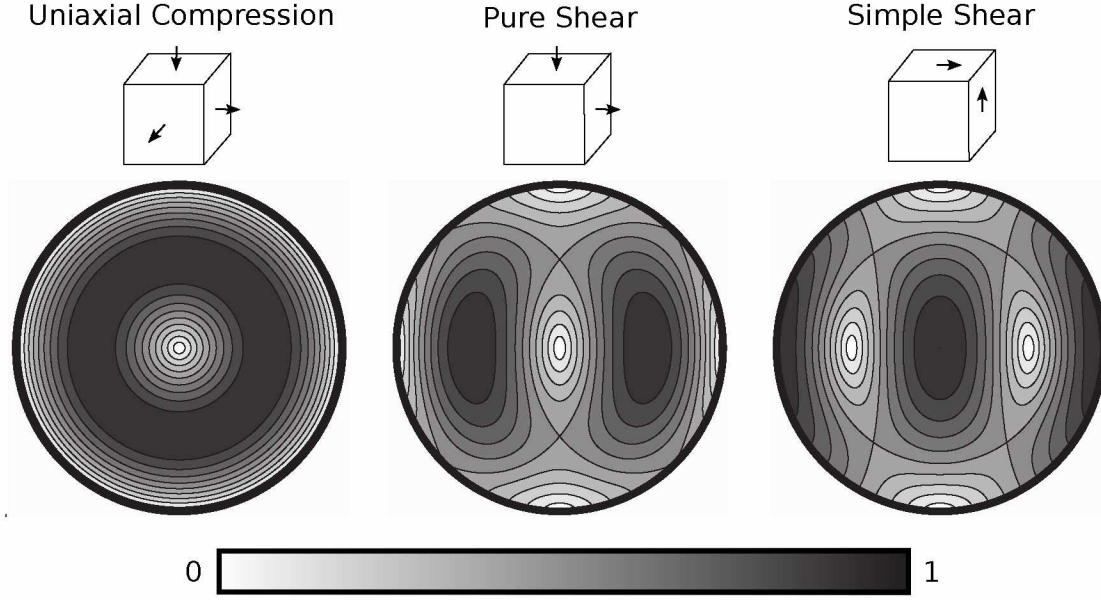


Figure 4.1: Contoured Schmidt plots of the magnitude of the Resolved Shear Stress \mathcal{T} from Eqn (4.9) for grains in the stress states of: uniaxial compression, pure shear, and simple shear. The values have been normalized by the maximum value of \mathcal{T} .

$$d_w(\vec{c}) = a_w^{-1} \exp[-w(\vec{\eta}^T \vec{c})^2], \quad (4.10)$$

where $w \in [-\infty, \infty]$ is the concentration parameter and a_w is the normalizing constant. Watson distributions are axial and defined on the entire unit sphere (\mathbb{S}^2). The Watson distribution describes single maximum fabrics concentrated around $\vec{\eta}$ when $w < 0$, equatorial girdle fabrics around the pole $\vec{\eta}$ when $w > 0$, and reduces to a random distribution when $w = 0$ (uniform on \mathbb{S}^2). FEVOR uses the open-source FADDEEVA package to compute the Dawson's function and error function needed for generating Watson distributions (Johnson, 2012).

4.4 PISM

To model the ice flow, we use the open-source Parallel Ice Sheet Model (PISM, 2015). PISM is well described in the literature (Bueler and Brown, 2009) and has been used in a wide variety of applications; from coupled ice-sheet climate simulations (e.g., Ziemen and others, 2014) to determining basal yield stress in outlet glaciers (e.g., Habermann and others, 2013). In brief, PISM is a fully parallelized, 3D ice-sheet model that uses the shallow ice approximation (SIA), the shallow shelf approximation (SSA), or a hybrid SIA-SSA to solve the stress balance equations (Winkelmann

and others, 2011) and uses an enthalpy formulation (Aschwanden and others, 2012) to model the thermodynamic properties of flowing ice.

4.5 The integrated PISM-FEVoR model

In the PISM-FEVoR integrated model, PISM controls the ice flow, the domain, and the adaptive time-stepping. PISM uses an Eulerian grid to compute the flow field. This grid also contains a number of Lagrangian particles ($P_l = (x_l, y_l, z_l)$), each containing a FEVoR distribution, which is carried by the PISM flow field.

Within PISM's explicit time-step, as outlined in the flow chart shown in Figure 4.2, PISM-FEVoR uses trilinear interpolation (Figure 4.3) to calculate the temperature (T_l), stress (σ_l), and velocity (\vec{v}_l) at each particle position. To trilinearly interpolate values at a particle's position, that particle must be within the convex hull of the ice grid (\mathcal{H}^g ; Figure 4.4). Because the particles are free to flow with the ice, decisions about particles that flow out of \mathcal{H}^g will need to be made, and these decisions will be problem-dependent (see our experiment below).

The particle positions are updated within every PISM time-step using Euler's method. Because the FEVoR model is the most computational intensive part of the PISM-FEVoR model, FEVoR is stepped over a user-specified interval (Δt_f) that typically exceeds the PISM time-step size. When the time at the end of the current PISM time-step is equal to the next FEVoR run time ($t + \Delta t = t_f^+$), a FEVoR time-step is preformed, an enhancement factor (E_l^*) from each particle's distribution is calculated.

FEVoR is integrated into PISM's shallow ice approximation (SIA) version of the stress balance equations. In the SIA, the deviatoric stress tensor ($\sigma'_l(x, y, z)$) only has non-zero components $\sigma'_{13} = \sigma'_{31}$ and $\sigma'_{23} = \sigma'_{32}$ because the driving force of gravity is balanced exclusively by shearing within the ice (Bueler and Brown, 2009). We calculate two enhancement factors

$$E_l^{i3} = \frac{|(\dot{\epsilon}_{i3})_l|}{|(\dot{\epsilon}_{i3})_{iso}|}, i = 1, 2 \quad (4.11)$$

where $(\dot{\epsilon}_{i3})_l$ is the strain rate component for the particle P_l , and $(\dot{\epsilon}_{i3})_{iso}$ is the strain rate component for an isotropic FEVoR distribution experiencing the same temperature and stress as P_l . Then $E_l^* = \max\{E_l^{13}, E_l^{23}\}$, but we set a minimum enhancement factor of 1 because the applied stress may be zero and a maximum enhancement of 10 (Cuffey and Paterson, 2010, p. 77), so $1 \leq E_l^* \leq 10$.

Once the particle enhancement factors are calculated, enhancement factors are determined for the regular PISM grid points (E_{xyz}^*) from the particles using natural neighbor interpolation

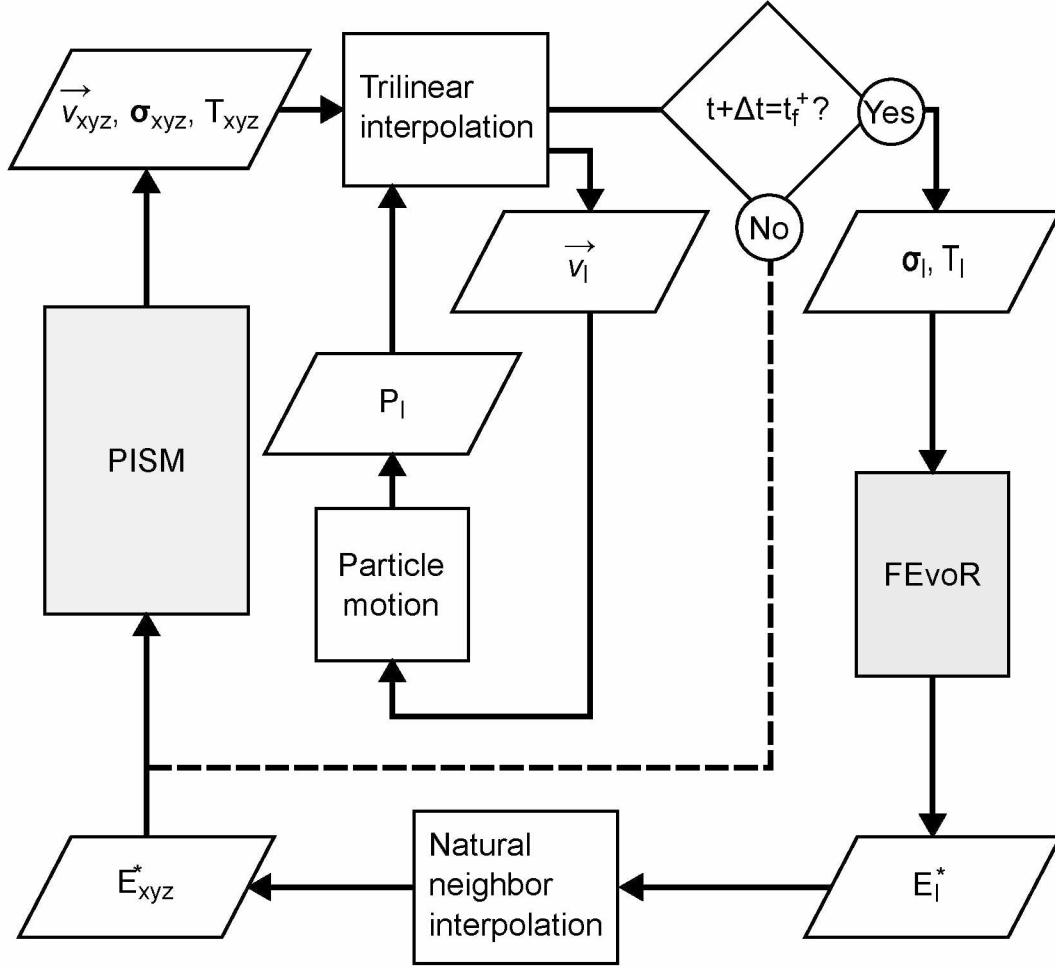


Figure 4.2: Flow chart of the combined PISM-FEVoR model. At each time-step, the 3D velocity \vec{v}_{xyz} , stress σ_{xyz} , and temperature T_{xyz} fields are trilinearly interpolated (Figure 4.3) at particle positions P_l . The particle positions are updated using the Euler method. FEVoR is stepped over a user-specified interval when the time at the end of the current PISM time-step is equal to the next FEVoR run time ($t + \Delta t = t_f^+$). An enhancement factor for each particle (E_l^*) is calculated. Using natural neighbor interpolation (Figure 4.5), enhancement factors are calculated for each grid point (E_{xyz}^*), which are then used to finish the PISM time-step and update the ice geometry.

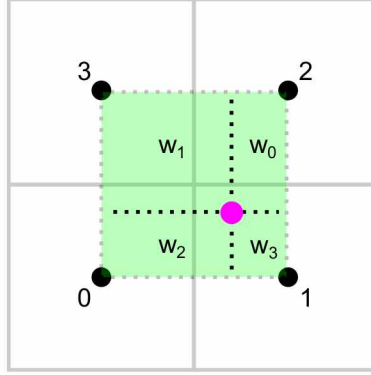


Figure 4.3: Geometric visualization of bilinear interpolation from a regular grid (black) to a particle (pink). The weight (w_i) of a value at grid point i is equal to the fractional area (outlined by dashed lines) of the interpolation rectangle (light green) opposite point i . Trilinear interpolation proceeds similarly with the fractional volumes of an interpolation cuboid.

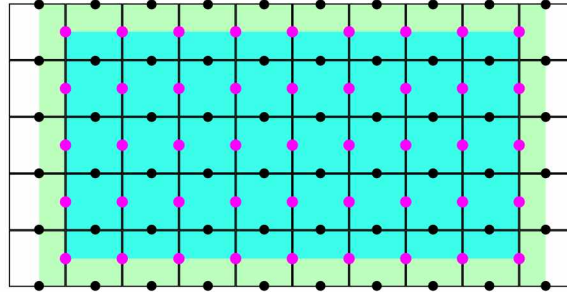


Figure 4.4: A cross-section of the computational domain of PISM-FEVOR. Regular PISM grid points are shown in black and the initial positions of the FEVOR particles are shown in pink. To interpolate values of a FEVOR particle from the PISM grid, particles must lie within the convex hull containing all the grid points (light green). Likewise, to interpolate the values of a grid point from its natural neighbor particles (Figure 4.5), the grid point must be within the convex hull containing all the particles (light blue). For points lying outside of the convex hull, some extrapolation decision must be made.

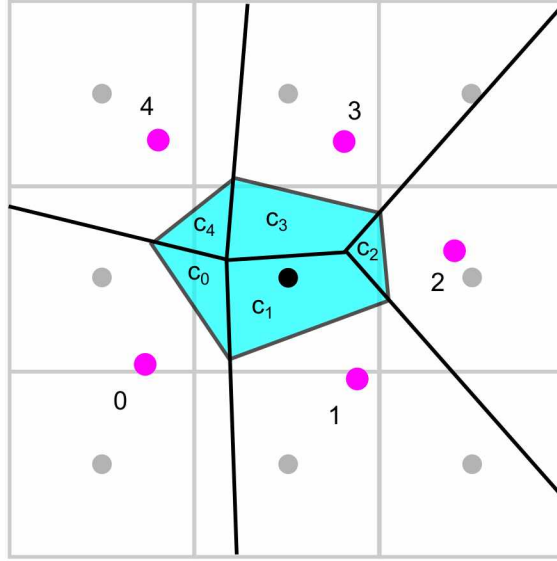


Figure 4.5: Visualization of natural neighbor interpolation of a grid point (black) from a scattered collection of particles (pink). The convex hull (Figure 4.4) containing the particles is divided into Voronoi cells (black lines). By inserting the grid point into the Voronoi tessellation, a new Voronoi cell given to the grid point (light blue) that steals area from the natural neighbors' cell. The stolen area, as a fraction of the new cell area, of a particles cell is then the weight (c_i) for a value at particle i . Natural neighbor interpolation proceeds similarly in three dimensions using the stolen volumes of three-dimensional Voronoi cells.

(Figure 4.5). Natural neighbor computations are preformed using the open-source Computational Geometry Algorithms library (CGAL, 2013; Flötotto, 2013). To interpolate values at a grid point from its natural neighbors, that grid point must be within the convex hull of the particles (\mathcal{H}^p ; Figure 4.4), while some decisions will need to be made about the values at the boundary grid points which are outside \mathcal{H}^p . Typically, surface grid points can simply be given $E^* = 1$, but the basal and side grid points decision will be problem dependent. Further, areas within the ice sheet may become devoid of particles as they flow out of an area leading to large Voronoi cells, especially at the surface, and poor representation of the enhancement field. Models should start with a high enough particle density such that the enhancement field is well represented throughout the simulation.

The enhancement factors are used by PISM to finish the (adaptive) time-step and update the ice geometry. Because the computation of E^* lags behind the PISM stress balance computation by Δt_f , we assume that E^* varies slowly.

Currently, PISM-FEVOR is limited to running in serial (single processor) because the particle motion has not been generalized to the PISM parallel grid structure. Work is currently being

undertaken, independent of this research, by Dr. Florian Ziemen at the Alfred Wegener Institute for Polar and Marine Research to implement Lagrangian tracer particles on the parallel PISM grid (personal communication, June 2015), which we hope to take advantage of in the future.

It should be noted that the PISM-FEVOR interaction described here (Figure 4.2) is agnostic to any particular ice-sheet or fabric model. That is, PISM acts as a black-box which generates the needed dynamical fields (\vec{v}_{xyz} , σ_{xyz} , and T_{xyz}) from the provided E_{xyz}^* field. Likewise, FEVOR acts as a black-box which generates E_{xyz}^* from the provided dynamical fields (\vec{v}_{xyz} , σ_{xyz} , and T_{xyz}).

4.6 Slab-on-slope example

To illustrate the PISM-FEVOR model, we simulate a 510m deep glacier of infinite length, with parallel sides, flowing down an inclined plane in the x -direction, with a slope $\theta = 1^\circ$ (Figure 4.6). The slab is frozen to its bed and has a surface temperature of $T = -30^\circ \text{C}$.

We describe this setup in PISM as a two dimensional (2D) rectangular grid of ice, with periodic boundary conditions on the faces perpendicular to the flow direction. The computational domain is 100km in \hat{x} , divided into 10km cells ($X = 10$), and 600m in \hat{z} , divided into 50m cells ($Z = 12$). The vertical grid extends above the slab, to account for any fluctuations in the ice thickness. Each grid point has an initial enhancement factor $E_{xz} = 1$.

The FEVOR particles (P_l) are initially distributed halfway between each vertical PISM grid point for every horizontal grid point in \hat{x} , except the x grid point furthest down slope (Figure 4.6). There are then $XZ = 120$ FEVOR particles in the domain. Because the vertical grid extends above the ice surface, some particles will be placed above the ice. These particles will move along with the surface of the ice, but experience no stress, and therefore do not evolve. Due to the periodic boundary conditions, particles that are carried out of the convex hull of PISM grid points \mathcal{H}^g on the down-slope face, re-enter \mathcal{H}^g on the up-slope face.

Each particle's FEVOR distribution has $N = 16 \times 16 \times 16 = 4096$ cubically-packed grains that experience mild nearest neighbor interactions, such that the local softness parameter (\mathcal{E}^c in Eqn (4.5)) for each grain is

$$\mathcal{E}^c = \frac{1}{2} \left(1 + \frac{1}{6} \sum_{i=1}^6 \frac{\mathcal{T}^i}{\mathcal{T}^c} \right), \quad (4.12)$$

(Kennedy and Pettit, 2015) where \mathcal{T}^c is the magnitude of the RSS experienced by grain c , and \mathcal{T}^i is the magnitude of the RSS experienced by the neighboring grains (Eqn (4.9)).

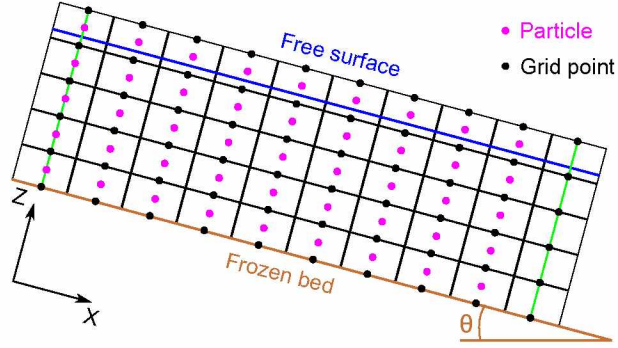


Figure 4.6: Initial PISM-FEVOR setup for the 2D slab-on-slope experiments with slope θ and periodic boundary conditions in x . Regular PISM grid points are shown in black and FEVOR particles are shown in pink. FEVOR particles are carried with the ice flow. Particles that pass the down-slope green line, re-enter upstream.

The distributions are initialized with a Watson concentration parameter (w_l^0) that increases linearly with depth in the ice as is typical of glacial ice. The particles at the surface have an initial concentration typical of ice just below the firn-ice transition ($w_l^0 = -2.0$ for $z \geq 475$ m; Kennedy and Pettit, 2015), and particles at the bottom of the ice have a strong single maximum ($w_l^0 = -15.0$ for $z = 25$ m).

In a slab-on-slope glacier simulation, there is no $\dot{\epsilon}_{23}$ component to the strain rate and Eqn (4.11) reduces to $E_l^* = E_l^{13}$. During each FEVOR time-step, these enhancement factors are interpolated back to the PISM grid points within the convex hull of the FEVOR particles (\mathcal{H}^p) using natural neighbor interpolation (Figure 4.5) and grid points outside \mathcal{H}^p are set from the boundary conditions. For the topmost surface of the grid, the enhancement factor is set to $E_{xz}^* = 1$, and grid points on the bed are given the maximum enhancement factor from within \mathcal{H}^p ($E_{x0}^* = \max(E_{xz}^*)$ for $x \neq 0, X$ and $z \neq 0Z$). For the grid points on the up-stream and down-stream faces, the enhancement factors are set to those directly interior to them in \mathcal{H}^p ($E_{0z}^* = E_{1z}^*$ and $E_{Xz}^* = E_{X-1,z}^*$).

Figure 4.7 shows a contour plot of the initial eigenvalues in the PISM grid which were calculated from FEVOR particles shown in pink. The initial enhancement factors increase from $E^* = 1.63$ at the surface to $E^* = 4.32$ at the base of slab.

In this and the subsequent experiments, we further simplified the PISM-FEVOR interaction. The stress (σ_l) at each particle position, in this setup, is derived from the well known analytical solution to a parallel-sided slab-on-slope glacier. While the stress could be trilinearly interpolated from the PISM grid, using the analytical solution allows us to avoid any possible error feedback from small variations that arise in the enhancement field as the slab evolves. Because of the low

density of FEVOR particles, the fluctuations appear as grid-scale features (Figure 4.8; described below) and may cause fluctuations in the stress field calculated by PISM. These fluctuations in stress will then feed back into the fabric evolution and the calculated enhancement factors. Due to the large computational cost of the FEVOR particles (Figure 4.9; described below), it is currently impractical to increase the particle density. Possible development paths to reduce the excessive costs associated with FEVOR are discussed later.

4.6.1 Evolution

The slab initially starts flowing with a surface velocity of 2.04ma^{-1} , which is the equivalent speed calculated from the analytical solution to this setup using an constant enhancement factor of $E = 3.8$ (Eqn (4.2)). Figure 4.8 shows the fabrics, particle positions, and enhancement factors calculated after 10 ka of evolution. The fabrics at the bottom of the slab have been weakened ($w_l^0 = -6.5$; $a_1^{(2)} = 0.819$), and the speed has been reduced to 1.32ma^{-1} (constant $E = 2.5$). The surface particles have been carried 12.655 km down the slab. Note that the total travel distance appears too small because the average surface velocity is lower than the initial and final surface velocities. The deepest fabrics quickly (≈ 1 ka) reduce to the steady-state profile do to the high stresses experienced at these depths, while the fabric near the surface take longer to achieve the steady-state profile (lower stress). Overall, this works to quickly reduce the surface velocity, which then slowly increases to its final value.

The PISM-FEVOR experiment described above, run in serial (single processor), took 7207.769 s on a desktop using an Intel[®] Xeon 3.0GHz processor with 16 GB of RAM available. Simulations without the FEVOR particles took 4.818 s on the same desktop. Figure 4.9 shows the simulation times for the slab-on-slope experiment when varying the number of grains in each FEVOR particle. The simulation time increases linearly with the number of particles in each distribution.

4.7 Slab-on-slope experiments

We test the fabric-flow enhancement by running three other simulations, only differing in their initial fabric profile (Figure 4.10a). The first simulation uses an isotropic initial fabric profile ($w_l^0 = 0$, $a_1^{(2)} = 0.33$, for all particles). The second simulation uses a step-change fabric profile where the top half of the particles are initialized with $w_l^0 = -2.0$ ($a_1^{(2)} = 0.53$) and the rest of the particles are initialized with $w_l^0 = -15.0$ ($a_1^{(2)} = 0.93$) – large step changes in the fabric profile can be seen in the Siple Dome, West Antarctica ice core (Di Prinzio and others, 2005). Small variations in fabric profiles are also commonly observed (e.g., Gusmeroli and others, 2012; Kennedy and others, 2013).

and are of interest due to their possible connection to paleoclimate (Kennedy and others, 2013; Kennedy and Pettit, 2015). The third simulation uses the same linear fabric profile as before, except the particles at $z = 75, 125$ and 225 m have an $a_1^{(2)}$ that has been increased by 0.05. The initial eigenvalues and calculated enhancement factors for these three profiles are shown in Figure 4.10c-e, respectively.

4.7.1 Evolution

Figure 4.10b shows the evolution of our fabric profiles after 10 ka. The linear fabric and linear fabric with variations have reached the same steady fabric profile. The initially isotropic fabric has not yet reached a steady profile, at any depth. The initial step-change profile is between the two previous final profiles; it has not reached a steady profile above 300 m from the bedrock, but has below that.

For the initially isotropic profile, the slab starts flowing with a surface velocity of 0.53 ma^{-1} (constant $E = 1$; Eqn (4.2)). Figure 4.10c shows the fabrics, particle positions, and enhancement factors calculated after 10 ka of evolution. The fabrics at the bottom of the slab have been strengthened ($w_l^0 = -6.0$; $a_1^{(2)} = 0.807$), and the speed has been increased to 1.21 ma^{-1} (constant $E = 2.3$). The surface particles were carried 10.591 km down the slab.

For the initially linear profile, the slab starts flowing with a surface velocity of 2.05 ma^{-1} (constant $E = 3.9$). Figure 4.10d shows the fabrics, particle positions, and enhancement factors calculated after 10 ka of evolution. The fabrics at the bottom of the slab have been weakened ($w_l^0 = -6.4$; $a_1^{(2)} = 0.821$), and the speed has been reduced to 1.33 ma^{-1} (constant $E = 2.5$). The surface particles were carried 12.765 m down the slab.

For the initially linear with variations profile, the slab starts flowing with a surface velocity of 2.06 ma^{-1} (constant $E = 3.9$), about 1% faster than the initially linear profile. Figure 4.10e shows the fabrics, particle positions, and enhancement factors calculated after 10 ka of evolution. The fabrics at the bottom of the slab have been weakened ($w_l^0 = -6.4$; $a_1^{(2)} = 0.820$), and the speed has been reduced to 1.32 ma^{-1} (constant $E = 2.5$). The surface particles were carried 12.667 m down the slab, about 12 m farther than the initially linear profile.

These results have been summarized in Table 4.2.

4.8 Further discussion

To evaluate PISM-FEVOR's ability to capture the enhanced deformation due to the fabric, we compare our results to those obtained by Ma and others (2010) with the GOLF model using a

Table 4.2: Results summary for the different initial fabric profiles. u_x^0 is the initial down slope surface velocity, and u_x^f is the final down slope surface velocity. E_0 is the initial equivalent constant enhancement factor, and E_f is the final equivalent constant enhancement factor. ΔP_x is the distance the surface particles traveled during the simulation. Note that the total travel distance appears too small because the average surface velocity is lower than the initial and final surface velocities. The deepest fabrics quickly (≈ 1 ka) reduce to the steady-state profile due to the high stresses experienced at these depths, while the fabric near the surface take longer to achieve the steady-state profile due to the lower stresses. Overall, this works to quickly reduce the surface velocity, which then slowly increases to its final value.

Initial Profile	u_x^0 (ma ⁻¹)	Constant E_0	u_x^f (ma ⁻¹)	Constant E_f	ΔP_x (km)
Linear	2.04	3.8	1.32	2.5	12.913
Linear variation	2.06	3.9	1.32	2.5	12.926
Step change	2.05	3.9	1.33	2.5	13.026
Isotropic	0.53	1.0	1.21	2.3	10.807

full-Stokes stress balance. They simulated a two-dimensional ice sheet with the same geometry as found in step 12 of the MISMIP 3a experiment (Marine Ice Sheet Model Intercomparison Project; Durand and others, 2009). For the grounded section of the ice sheet, using an reduced-depth temperature profile modeled on the temperature profile observed at the Greenland Icecore Project (GRIP) site (Gagliardini and Meyssonier, 2002), and a constant fabric profile which increases as a function of reduced depth (Fig. 2; Ma and others, 2010), they found an equivalent constant enhancement factor of $E = 5.6$. These conditions are similar to the initial setup of our slab for the linear fabric profile, except, Ma’s temperature profile is nine degrees warmer at the base, and the fabric profile is non-linear with stronger fabric for most the depth of the ice sheet. Because we only have 10 particle levels within the ice, it is not possible to reproduce Ma’s fabric profile exactly, but simulations with Ma-like fabric profiles and an increased basal heat flux to match Ma’s basal temperature results in E_0 that range from 5.2 to 5.5 (not shown). The resulting E_0 value is very sensitive to the imposed fabric profile.

We find our model is able to accurately represent the enhancement field, and its effect on flow, even in our simplified model. Furthermore, the distances the particles travel down slope differ in all the simulations, even for the simulations with the linear and linear-with-variations profiles, which only differ slightly. This shows that the entire integrated fabric-flow history is required to accurately model the flow, and therefore any properties that are carried with the ice. This provides an additional, independent validation of the need for integrated fabric flow models.

4.8.1 Further development

The computational cost of PISM-FEVOR is currently quite high (Figure 4.9). In order for PISM-FEVOR to be applicable to Greenlandic and Antarctic simulations, the computational cost will have to be reduced drastically. The first developmental step should be to allow the FEVOR particles to be distributed across the parallel PISM grid. This can be implemented by hooking into the ongoing development of Lagrangian tracer particles in PISM. The development that will have the largest benefit, however, is parallelizing FEVOR, as the bulk of the computational time is in running the FEVOR models.

It is likely that any fully parallel implementation of PISM-FEVOR will be targeted to run on a high-performance computer (HPC), or super-computer, due to the sheer number of FEVOR particles that would be needed to model any complex geometry. These HPC systems are typically comprised of a number of compute nodes, each containing one or more central processing units (CPUs) with a number of large feature-rich processing cores, dedicated random access memory (RAM), and sometimes one or more graphical processing units (GPUs) containing many hundreds of small feature-sparse processing cores (e.g., Joubert and others, 2015). A fully parallel PISM-FEVOR scheme maybe be a CPU only scheme, as PISM is currently, or a hybrid CPU-GPU scheme.

We propose that PISM-FEVOR may be particularly suited to a hybrid CPU-GPU scheme. FEVOR performs many thousands of individual crystal computations that are averaged together to determine the bulk polycrystalline response. These crystal computations are not data-intensive and can likely be ported to the small processing cores found on a GPU to be preformed simultaneously. The CPUs can then handle the more complex and data intensive operations, such as, PISM evolution, movement of the FEVOR particles and interpolation of data between the PISM grid and the FEVOR particles. A detailed evaluation of the possible speedups, for both a parallel implementation of FEVOR on CPUs and on GPUs, should be undertaken to determine which scheme is best suited to PISM-FEVOR (Lee and others, 2010).

It is important to note, however, that PISM's use of the shallow ice approximation (SIA) will prevent PISM-FEVOR from accurately modeling fabrics at locations that are not dominated by shear stress, such as an ice divide. Strong fabric develops at depth in these location (e.g., Gusmeroli and others, 2012) due to the membrane stresses which are not represented in the SIA. Modeling fabrics in these locations will necessarily entail using a higher-order approximation to the Navier-Stokes equation in order to resolve the membrane stresses at these locations. Fortunately, a

higher-order approximation is planned for inclusion in PISM, but no timeline for inclusion is currently given (PISM, 2015). Even then, the lack of membrane stresses are not the only issue for the SIA in a divide region (e.g., Gillet-Chaulet and Hindmarsh, 2011) and it may be necessary to use the full-Stokes stress balance equation, which, unfortunately is not planned for inclusion in PISM at this time. Nevertheless, the lessons learned here, and throughout the further development of PISM-FEVOR, can be applied equally well to any similar undertaking if needed.

4.9 Conclusions

Using a slab-on-slope glacier setup, we have shown that PISM-FEVOR captures the flow enhancement due to fabric, and provides a further validation for using integrated fabric-flow model over using constant enhancement factors in ice sheet models. PISM-FEVOR successfully incorporates a mean-field polycrystalline model into a ice-sheet scale ice flow model. Because of this integration, PISM-FEVOR is capable of investigating non-steady material parameters, and its effect on flow, which is a capability currently lacking in other polycrystal to ice-sheet scale models. Although this comes at a high computational cost, there are clear developmental steps that can be taken to reduce the computational requirements of PISM-FEVOR. Implementing Lagrangian tracer particles on the PISM grid, and extending FEVOR to parallel processing on a GPU should be the two primary developmental goals.

4.10 Acknowledgements

We thank Andy Aschwanden, Ed Bueler, and the rest of the PISM development group for their support. We thank Robert McNabb and Matrin Truffer for their help throughout the preparation of this manuscript. The work presented in this paper was supported by the US National Science Foundation (NSF) grants OPP#0948247, OPP#0940650, and OPP#0636795. Development of PISM is supported by NASA grants NNX13AM16G and NNX13AK27G.

4.11 References

- Alley, R.B., 1992. Flow-law hypotheses for ice-sheet modeling, *J. Glaciol.*, **38**(129), 245–256.
- Aschwanden, A., E. Bueler, C. Khroulev and H. Blatter, 2012. An enthalpy formulation for glaciers and ice sheets, *J. Glaciol.*, **58**(209), 441–457.
- Azuma, N., 1994. A flow law for anisotropic ice and its application to ice sheets, *Earth and Planetary Science Letters*, **128**(3-4), 601–614.

- Azuma, N. and A. Higashi, 1985. Formation processes of ice fabric pattern in ice sheets, *Ann. Glaciol.*, **6**, 130–134.
- Becker, J.K., P.D. Bons and M.W. Jessell, 2008. A new front-tracking method to model anisotropic grain and phase boundary motion in rocks, *Computers and Geosciences*, **34**(3), 201–212.
- Bueler, E. and J. Brown, 2009. The shallow shelf approximation as a “sliding law” in a thermomechanically coupled ice sheet model, *J. Geophys. Res.*, **114**(F3), 1–21.
- Castelnau, O., P. Duval, R.A. Lebensohn and G.R. Canova, 1996. Viscoplastic modeling of texture development in polycrystalline ice with a self-consistent approach: comparison with bound estimates, *J. Geophys. Res.*, **101**(B6), 13851–13868.
- CGAL, 2013. Computational Geometry Algorithms Library, <http://www.cgal.org>, 4.2.
- Cuffey, K.M. and W.S.B. Paterson, 2010. The physics of glaciers, Butterworth-Heinemann/Elsevier, fourth ed.
- Di Prinzio, C.L., L.A. Wilen, R.B. Alley, J.J. Fitzpatrick, M.K. Spencer and A.J. Gow, 2005. Fabric and texture at Siple Dome, Antarctica, *J. Glaciol.*, **51**(173), 281–290.
- Durand, G., A. Svensson, A. Persson, O. Gagliardini, F. Gillet-Chaulet, J. Sjolte, M. Montagnat and D. Dahl-Jensen, 2009. Evolution of the texture along the EPICA Dome C ice core, *Low Temperature Science*, **68**(Sup.), 91–105.
- Faria, S.H., I. Weikusat and N. Azuma, 2014a. The microstructure of polar ice. Part I: Highlights from ice core research, *Journal of Structural Geology*, **61**, 2–20.
- Faria, S.H., I. Weikusat and N. Azuma, 2014b. The microstructure of polar ice. Part II: State of the art, *Journal of Structural Geology*, **61**, 21–49.
- FEvoR, 2015. Fabric Evolution with Recrystallization, <https://github.com/FEvoR>, master branch.
- Flötotto, J., 2013. 2D and Surface Function Interpolation, CGAL User and Reference Manual, CGAL Editorial Board, 4.2 ed., <http://doc.cgal.org/4.2/CGAL.CGAL/html/packages.html#PkgInterpolation2Summary>.
- Gagliardini, O., G. Durand and Y. Wang, 2004. Grain area as a statistical weight for polycrystal constituents, *J. Glaciol.*, **50**(168), 87–95.

- Gagliardini, O. and J. Meyssonier, 2002. Lateral boundary conditions for a local anisotropic ice-flow model, *Ann. Glaciol.*, **35**(1), 503–509.
- Gillet-Chaulet, F., O. Gagliardini, J. Meyssonier, M. Montagnat and O. Castelnau, 2005. A user-friendly anisotropic flow law for ice-sheet modelling, *J. Glaciol.*, **51**(172), 3–14.
- Gillet-Chaulet, F. and R.C.A. Hindmarsh, 2011. Flow at ice-divide triple junctions: 1. Three-dimensional full-Stokes modeling, *Journal of Geophysical Research: Earth Surface*, **116**(2), 1–15.
- Glen, J.W., 1955. The creep of polycrystalline ice, *Proceedings of the Royal Society of London. Series A, Mathematical and Physical Sciences*, **228**(1175), 519–538.
- Gusmeroli, A., E.C. Pettit, J.H. Kennedy and C. Ritz, 2012. The crystalline fabric of glacial ice from full-waveform borehole sonic logging, *J. Geophys. Res.*, **117**(F03021), 1–13.
- Habermann, M., M. Truffer and D. Maxwell, 2013. Changing basal conditions during the speed-up of Jakobshavn Isbræ, Greenland, *The Cryosphere*, **7**(6), 1679–1692.
- Hooke, R.L., 2005. Principles of glacier mechanics, Cambridge University Press.
- Johnson, S.G., 2012. Faddeeva Package, http://ab-initio.mit.edu/wiki/index.php/Faddeeva_Package, dec. 2012 rev.
- Joubert, W., R. Archibald, M. Berrill, B. Michael Brown, M. Eisenbach, R. Grout, J. Larkin, J. Levesque, B. Messer, M. Norman, B. Philip, R. Sankaran, A. Tharrington and J. Turner, 2015. Accelerated application development: The ORNL Titan experience, *Computers & Electrical Engineering*.
- Kamb, W.B., 1959. Ice petrofabric observation from Blue Glacier, Washington, in relation to theory and experiment, *J. Geophys. Res.*, **64**(11), 1891–1909.
- Kennedy, J.H. and E.C. Pettit, 2015. The response of fabric variations to simple shear and migration recrystallization, *J. Glaciol.*, **61**(227), 537–550.
- Kennedy, J.H., E.C. Pettit and C.L. Di Prinzio, 2013. The evolution of crystal fabric in ice sheets and its link to climate history, *J. Glaciol.*, **59**(214), 357–373.
- Lee, V.W., C. Kim, J. Chhugani, M. Deisher, D. Kim, A.D. Nguyen, N. Satish, M. Smelyanskiy, S. Chennupaty, P. Hammarlund, R. Singhal and P. Dubey, 2010. Debunking the 100X GPU vs.

- CPU myth: an evaluation of throughput computing on CPU and GPU, *SIGARCH Comput. Archit. News*, **38**(3), 451–460.
- Ma, Y., O. Gagliardini, C. Ritz, F. Gillet-Chaulet, G. Durand and M. Montagnat, 2010. Enhancement factors for grounded ice and ice shelves inferred from an anisotropic ice-flow model, *J. Glaciol.*, **56**(199), 805–812.
- Montagnat, M., O. Castelnau, P.B. Bons, S.H. Faria, O. Gagliardini and F. Gillet-Chaulet, F. Grennerat, A. Griera, R.A. Lebensohn, H. Moulinec, J. Roessiger and P. Suquet, 2014. Multiscale modeling of ice deformation behavior, *Journal of Structural Geology*, **68**, 78–108.
- Nye, J.F., 1957. The distribution of stress and velocity in glaciers and ice-sheets, *Proceedings of the Royal Society of London. Series A. Mathematical and Physical Sciences*, **239**(1216), 113–133.
- PISM, 2015. Parallel Ice Sheet Model, <http://www.pism-docs.org/>, fevor branch.
- Placidi, L., R. Greve, H. Seddik and S.H. Faria, 2010. Continuum-mechanical, Anisotropic Flow model for polar ice masses, based on an anisotropic Flow Enhancement factor, *Continuum Mechanics and Thermodynamics*, **22**(3), 221–237.
- Rudolph, M.L. and M. Manga, 2012. Effects of anisotropic viscosity and texture development on convection in ice mantles, *J. Geophys. Res.*, **117**(E11), E11003.
- Thorsteinsson, T., 2001. An analytical approach to deformation of anisotropic ice-crystal aggregates, *J. Glaciol.*, **47**(158), 507–516.
- Thorsteinsson, T., 2002. Fabric development with nearest-neighbor interaction and dynamic recrystallization, *J. Geophys. Res.*, **107**(B1,2014), 1–13.
- Thorsteinsson, T., E.D. Waddington, K.C. Taylor, R.B. Alley and D.D. Blankenship, 1999. Strain rate enhancement at Dye 3, Greenland, *J. Glaciol.*, **45**(150), 338–345.
- Winkelmann, R., M.A. Martin, M. Haseloff, T. Albrecht, E. Bueler, C. Khroulev and A. Levermann, 2011. The Potsdam Parallel Ice Sheet Model (PISM-PIK) – Part 1: Model description, *The Cryosphere*, **5**(3), 715–726.
- Ziemen, F.A., C.B. Rodehacke and U. Mikolajewicz, 2014. Coupled ice sheet-climate modeling under glacial and pre-industrial boundary conditions, *Climate of the Past*, **10**(5), 1817–1836.

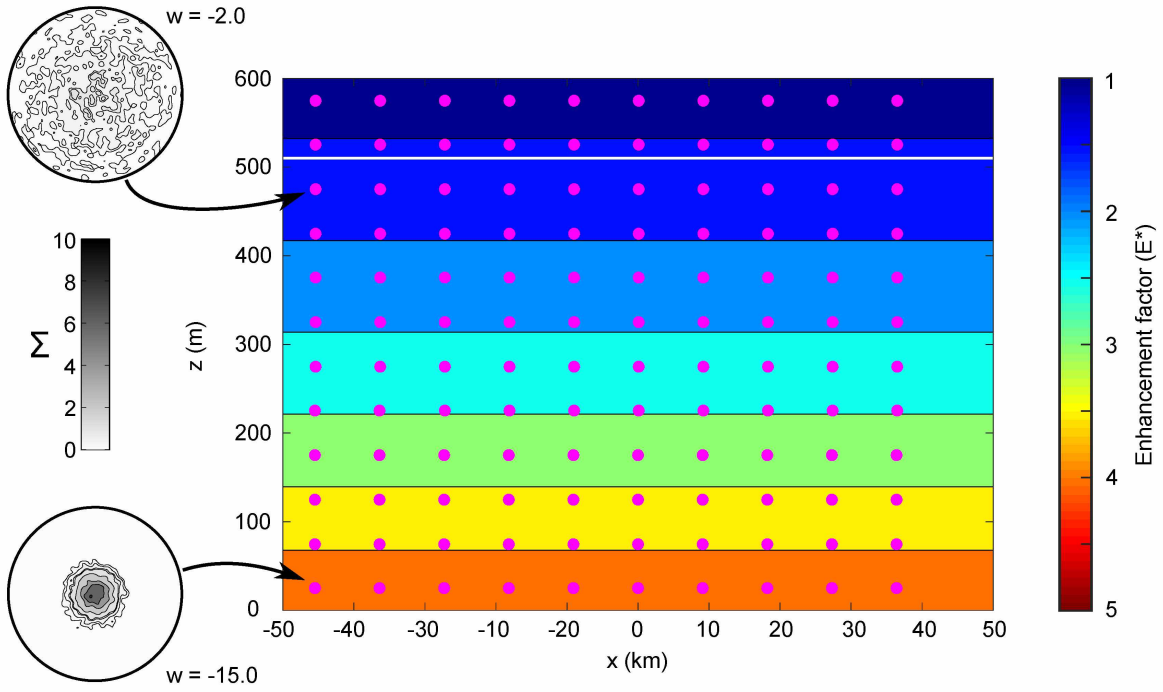


Figure 4.7: Initial eigenvalues and calculated enhancement factors for a slab-on-slope with a linearly increasing fabric profile. The 510 m thick slab will flow to the right, has a slope of $\theta = 1^\circ$ (Figure 4.6), a surface temperature of $T = -30^\circ\text{C}$, a basal heat flux of 42 mW m^{-2} , and 120 FEVOR particles within (positions shown in pink). Schmidt plots for the surface and bed fabrics are shown on the left. The fabrics are contoured at levels of $0, 2\Sigma, \dots, 10\Sigma$ where Σ is the standard deviation of the density of grains from the expected density for isotropic ice (Kamb, 1959). The surface particles' fabric is initialized with a Watson concentration parameter of $w^0 = -2.0$ ($a_1^{(2)} = 0.53$; Eqn (4.10)) and the concentration parameter increases linearly with depth, to a maximum value of $w^0 = -15.0$ ($a_1^{(2)} = 0.93$).

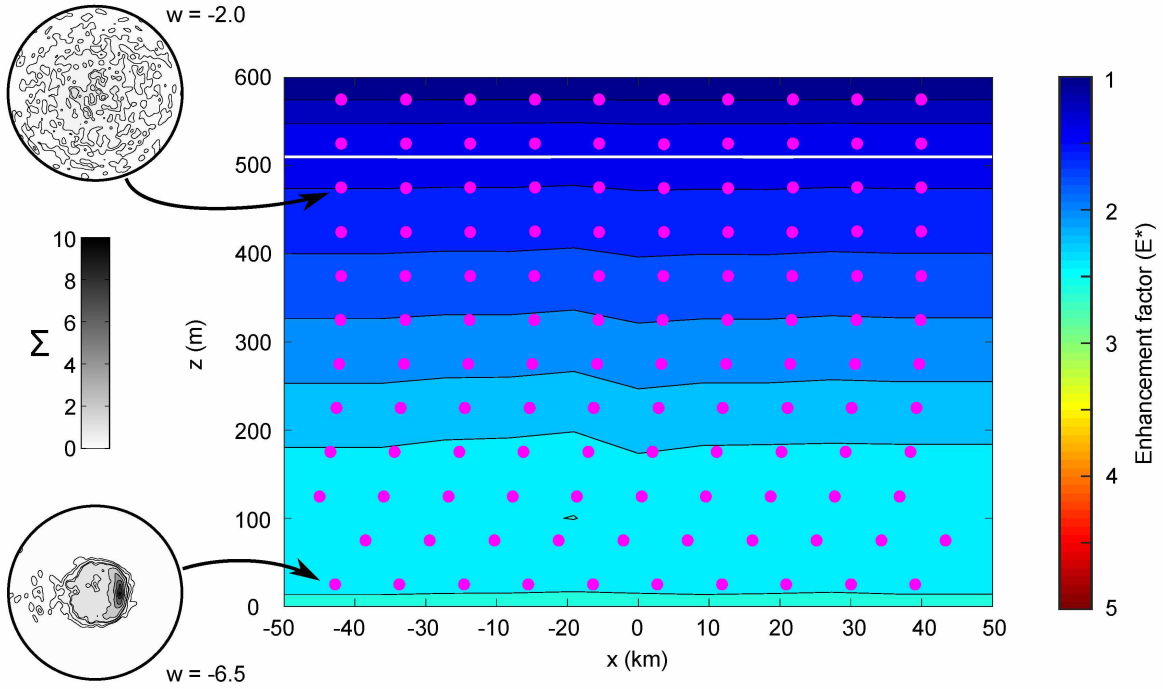


Figure 4.8: The evolution of FEVoR particles for a slab with a linearly increasing initial fabric. The slab has evolved for 10 ka with 50 a time-steps. See Figure 4.7 caption for figure details. The variation in the contour lines is a result of the small differences in the randomly generated fabrics from particle to particle, and the large horizontal spacing of the particles, which cause the fluctuations to appear grid-scale features.

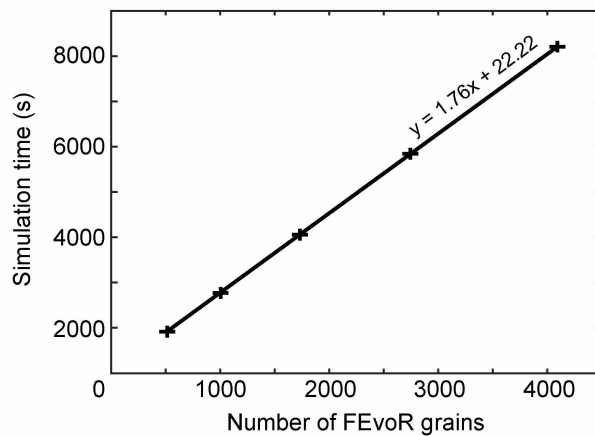


Figure 4.9: Simulation times for the slab-on-slope experiment with differing number of FEVoR distribution grains. The slab was evolved through 242.0 a with 60.0 a time-steps after the 2.0 a evolution shown in Figure 4.7. Simulation time increases linearly with the number of grains in each FEVoR particle's distribution.

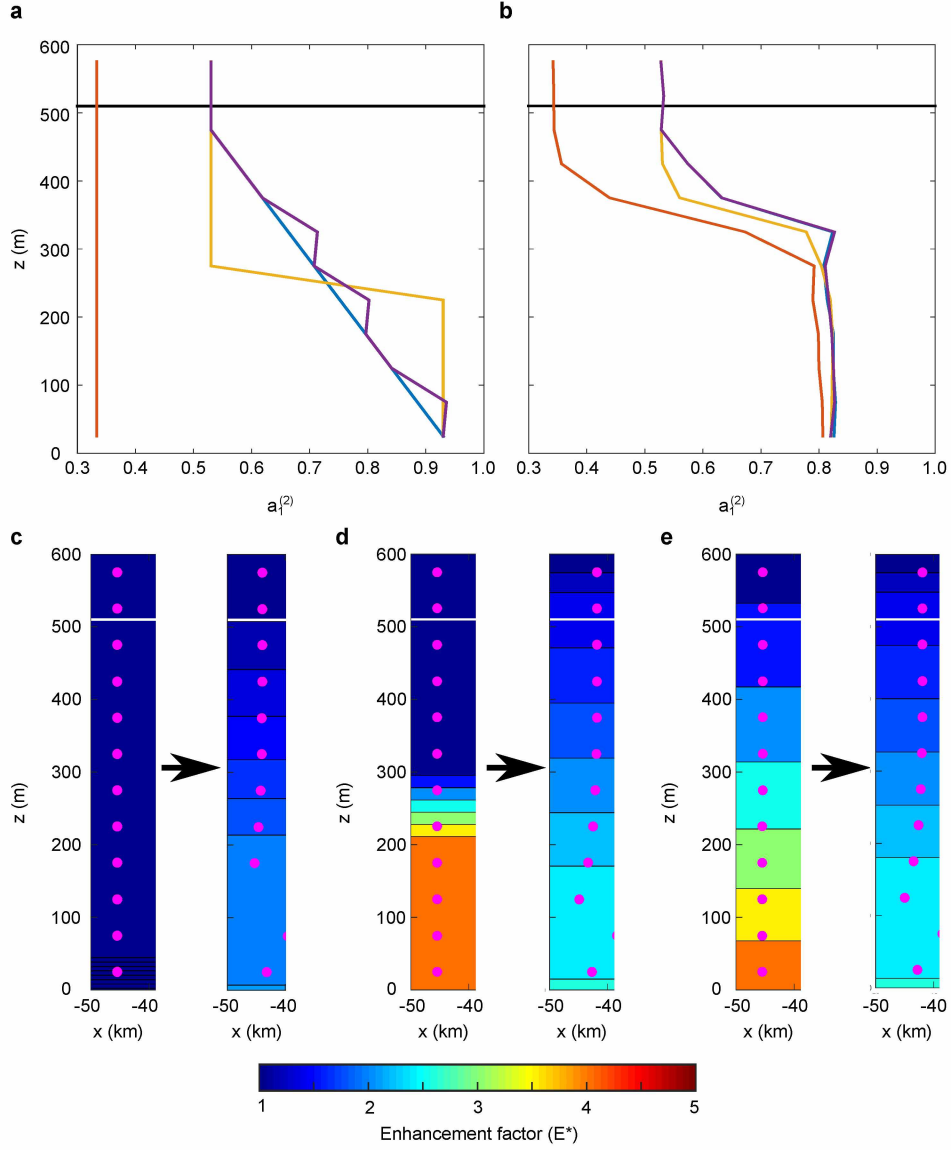


Figure 4.10: The evolution of FEVOR particles in a slab with a variety of initial fabric profiles. **a.** The initial linear, isotropic, and step-change profiles are shown by the blue, orange, and gold curves respectively. The purple curve shows a linear fabric where the fabrics at $z = 75, 125$, and 225 m have been strengthened by 0.05. **b.** The fabric profiles after 10 ka of evolution. **c-e.** The initial enhancement fields and particle positions and the evolved enhancement fields and particle positions for the isotropic, step-change, and linear with variations fabric profiles, respectively. See Figure 4.7 and Figure 4.8 caption for details **c-e**.

Chapter 5

Conclusions

The ultimate goal of the project which this research contributes to, is to develop ice crystalline fabric as a climate proxy. Recall from Chapter 1, that:

In order for climate history to be inverted from fabric data, a forward model of the ice fabric evolution is needed. The forward model must include the ice-climate interaction in the firn, and the subsequent metamorphism of the firn as it turns to ice, as well as the further evolution of ice within the ice sheet. Because this is a many-scale problem, encompassing processes from the mesoscopic to the macroscopic and beyond, a complete forward model will necessarily entail a number of interacting models. These models will need to compute: the climate, the firn microstructure evolution, the firn densification, the ice microstructure evolution, and the ice flow. These models can be split into two regimes, the firn regime and the ice regime.

Throughout the work presented in this dissertation, we have laid the foundation necessary for the development of ice crystalline fabric as a climate proxy by putting the ice regime on a solid theoretical foundation. That is, we have:

1. shown that a variation in fabric just below the firn ice transition may be preserved;
2. determined how long, and under what conditions, the variation is preserved in ice-sheet like conditions;
3. successfully created an initial flow-fabric integrated model which, once fully developed, can be used to investigate in situ fabric evolution.

In Chapter 2 we have modeled the evolution of a subtle fabric variation in conditions typical of a polar ice-divide. Throughout the depth of a polar ice-divide, fabric evolution is driven by uniaxial (an ice dome) or pure shear (an ice ridge) stresses. The evolution of fabric is further influenced by polygonization (sometimes termed rotation recrystallization) at intermediate depth within a polar ice divide. We find that in these conditions, a fabric variation is able to persist for ≈ 200 ka. Using data from Taylor Dome, East Antarctica, to create a simple model for an ice divide, we found that the fabric variation was able to persist throughout the entire depth of the simulated ice divide.

Chapter 3 extends our work to include conditions found throughout a polar ice-sheet where shear stresses and higher temperatures may be experienced, and migration recrystallization may influence the fabric evolution. We find that under all modeled conditions there is a so called ‘window of opportunity,’ where a subtle fabric variation can be preserved. Shear stresses extend how long the fabric variation persists and may act to enhance the fabric variation (under certain conditions) by rotating grains into softer orientations and reducing the number of polygonization events. Higher temperature reduces the overall time in which the fabric variation can be preserved but does not influence the evolution profile, except, when comparing runs across the thermal activation energy threshold at $\approx -10^\circ\text{C}$. Migration recrystallization did not eliminate the fabric variation for any of the modeled stress or temperature conditions, contrary to conventional understanding. Higher levels of nearest neighbor interactions, however, reduce the strength of the fabric variation at any given bulk strain when compared to lower interaction levels. Even with full nearest-neighbor interactions the fabric variation was able to persist to at least 0.35 of the modeled bulk strain – the modeled bulk strain achieved at the base of the simulated Taylor Dome-like ice-divide in Chapter 2.

Chapter 4 discusses the integration of our Fabric Evolution with Recrystallization (FEVOR) model, developed in the previous two chapters, with the Parallel Ice Sheet Model (PISM). Because FEVOR does not compute ice flow, combining it with a flow model such as PISM is necessary to apply it to a particular location. PISM-FEVOR represents the first step into fully incorporating a polycrystal scale model that includes recrystallizations into an ice-sheet scale flow model. Unlike other polycrystal to ice-sheet flow models, which do not directly include a polycrystal model, PISM-FEVOR is capable of investigating non-steady material properties, and its effect on flow. The PISM-FEVOR model was able to reproduce the equivalent constant enhancement factors obtained by Ma and others (2010) with the GOLF model using a full-Stokes stress balance. PISM-FEVOR further provided an independent validation for using an integrated fabric-flow ice sheet model. This capability, however, does come at a high computational cost. Chapter 4 outlines some future development goals that may reduce the computational burden of the PISM-FEVOR model.

5.1 Looking forward

There is still much more work that needs to be done in order to fully develop fabric as a climate proxy. In the ice regime, experiments similar to the ones presented here should be conducted with a variety of polycrystalline models to corroborate our results. The development of PISM-FEVOR should continue; the full parallel capability of PISM needs to be exploited and FEVOR needs

to be parallelized to run on either central processing units (CPUs) or graphical processing units (GPUs). A fully developed PISM-FEVOR (using a higher-order stress balance), when applied to well studied ice-core locations, could be used to determine what types of initial fabric variations, if any, are able to reproduce the fabric variations observed deep within an ice core. For example, it may be possible to determine if initial fabric variations can describe the large jump in fabric (or any part thereof) observed in Siple Dome, West Antarctica (Di Prinzio and others, 2005).

The firn regime, unfortunately, has seen only limited investigation of the fabric development, and how it may relate to climate (Carns and others, 2010; Adams and Miller, 2003; Montagnat and others, 2014). A climate-firn model needs to be developed, and many more observations of firn evolution, both in situ and in the laboratory, need to be undertaken (Kipfstuhl and others, 2009; Faria and others, 2014a,b). Because the firn regime is where the ice is interacting with the climate, this region should be the focus of any ongoing effort to develop fabric as a climate proxy.

5.2 Final words

Although the work left to develop the fabric proxy may seem a daunting undertaking, we have outlined a possible path forward. We hope our work provides you mostly with the sense of excitement; the kind of excitement found in the possibility of creating something new – a climate proxy from the fabric itself.

It seems fitting to conclude by showing Figure 1.3 again — it is the apparent (qualitative) correlation between the fabric and the known climate proxy $\delta^{18}\text{O}$ profiles which sent us down this path. Let it continue to inspire a drive to prove, or disprove if that case may be, a causation for such an intriguing correlation.

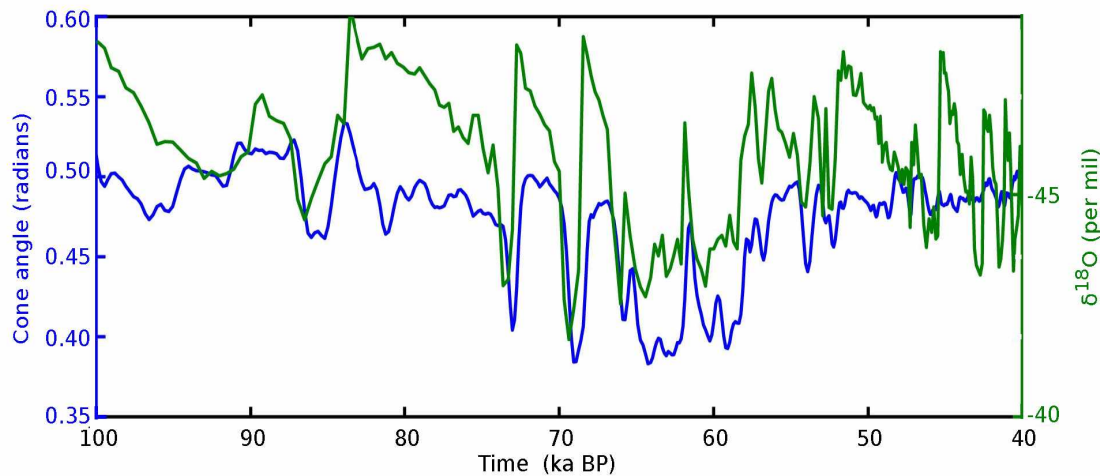


Figure 5.1: Comparison of $\delta^{18}\text{O}$ and fabric in the GISP2 ice core (reprint of Figure 1.3). Changes in the fabric (blue curve; Gow and others, 1997) appears to correlate with the known climate proxy $\delta^{18}\text{O}$ (green curve; Grootes and others, 1993).

5.3 References

- Adams, E.E. and D.A. Miller, 2003. Ice crystals grown from vapor onto an orientated substrate: application to snow depth-hoar development and gas inclusions in lake ice, *J. Glaciol.*, **49**(164), 8–12.
- Carns, R., E.D. Waddington, E.C. Pettit and S.G. Warren, 2010. A model of grain growth and crystal fabric in polar snow and firn, *AGU Fall Meeting Abstracts*, D572.
- Di Prinzio, C.L., L.A. Wilen, R.B. Alley, J.J. Fitzpatrick, M.K. Spencer and A.J. Gow, 2005. Fabric and texture at Siple Dome, Antarctica, *J. Glaciol.*, **51**(173), 281–290.
- Faria, S.H., I. Weikusat and N. Azuma, 2014a. The microstructure of polar ice. Part I: Highlights from ice core research, *Journal of Structural Geology*, **61**, 2–20.
- Faria, S.H., I. Weikusat and N. Azuma, 2014b. The microstructure of polar ice. Part II: State of the art, *Journal of Structural Geology*, **61**, 21–49.
- Gow, A.J., D.A. Meese, R.B. Alley, J.J. Fitzpatrick, S. Anandakrishnan, G.A. Woods and B.C. Elder, 1997. Physical and structural properties of the Greenland Ice Sheet Project 2 ice core : A review, *J. Geophys. Res.*, **102**(C12), 26,559–26,575.
- Grootes, P.M., M. Stuiver, J.W.C. White, S. Johnsen and J. Jouzel, 1993. Comparison of oxygen isotope records from the GISP2 and GRIP Greenland ice cores, *Nature*, **366**(6455), 552–554.

- Kipfstuhl, S., S.H. Faria, N. Azuma, J. Freitag, I. Hamann, P. Kaufmann, H. Miller, K. Weiler and F. Wilhelms, 2009. Evidence of dynamic recrystallization in polar firn, *J. Geophys. Res.*, **114**(B5), 1–10.
- Ma, Y., O. Gagliardini, C. Ritz, F. Gillet-Chaulet, G. Durand and M. Montagnat, 2010. Enhancement factors for grounded ice and ice shelves inferred from an anisotropic ice-flow model, *J. Glaciol.*, **56**(199), 805–812.
- Montagnat, M., O. Castelnau, P.B. Bons, S.H. Faria, O. Gagliardini and F. Gillet-Chaulet, F. Grennerat, A. Grier, R.A. Lebensohn, H. Moulinec, J. Roessiger and P. Suquet, 2014. Multiscale modeling of ice deformation behavior, *Journal of Structural Geology*, **68**, 78–108.